

POLITECNICO DI TORINO

Ph.D. in Materials Science and Technology

Ph.D. Thesis

Metal matrix composites reinforced with SiC long fibers
and carbon nanomaterials produced by electrodeposition



Muhammad Ramzan Abdul Karim
XXV Cycle

Supervisors:

Prof. Matteo Pavese
Prof. Paolo Fino

Coordinator:

Prof. Claudio Badini

Department of Applied Science and Technology (DISAT),
Politecnico di Torino, Italy

December 2014

Metal matrix composites reinforced with SiC long fibers and carbon nanomaterials produced by electrodeposition

By

Muhammad Ramzan Abdul Karim

Thesis submitted as partial fulfilment of the requirements for the award of Ph.D. degree in Science and Technology of Materials at Politecnico di Torino, Italy.

DEDICATION

I dedicate this work to:

My late grandparents “Nabi Bakhsh” and “Ghulam Zainab”;

My parents “Maher Muhammad Nawaz” and “Maharani Ghulam Sakeena”

I believe that without their love, prayers, support and sacrifices; I wouldn't have been at the stage where I am today.

ACKNOWLEDGEMENTS

First of all, I thank to Almighty God for bestowing His countless blessings on me and making me able to complete my doctoral thesis. Then I would like to say thanks to HEC Pakistan for their trust in me and awarding me the financial and moral support for PhD studies abroad.

I would like to extend my sincere gratitude to my tutors and mentors Prof. Matteo Pavese and Prof. Paolo Fino for their special guidance and discussions about the research work and also for the partial financial support during the last year of study. I simply cannot express the gratitude in words for their all-time support and standing with me through thick and thin during my stay at Politecnico di Torino. Also special thanks to my supervisor Prof. Claudio Badini for giving me an opportunity to work in the HTMAT group. I am also thankful to Prof. Daniele Ugues for his help and valuable guidance about the pin-on-disk experiments. Thanks to Elisa Ambrosio for her guidance about the electrodeposition process. Also I would like to thank all of my colleagues in the HTMAT group for their help and providing me friendly environment to work. I really learned a lot from all of you. I am also grateful to my friends Ehsan ul Haq and Azhar Hussain for their moral support, encouragement and motivating words during all this duration.

Special thanks to my family and relatives for their love and prayers. I cannot express gratitude in words to my father, mother, sister and younger brother Zeeshan Ahmad Shani for all of their sacrifices and hardships bearing on my behalf. I would simply say that it is just because of your endless affection and prayers that enabled me to complete my studies. At the end I would like to say special thanks to my wife for her love, prayers and support and for granting me the most precious gift of my life, my cute little nightingale “Andaleeb”.

Table of Contents

| | |
|---|----|
| ACKNOWLEDGEMENTS | I |
| Abstract | VI |
| Chapter 1 Metal Matrix Composites | 1 |
| 1.1 Introduction | 1 |
| 1.2 Fiber reinforced metal matrix composites (FRMMCs)..... | 4 |
| 1.2.1 Metallic matrices | 4 |
| 1.2.2 Fiber reinforcements..... | 5 |
| 1.2.3 Silicon carbide fibers | 6 |
| 1.2.4 Role and characteristics of interface..... | 6 |
| 1.2.5 Mechanical properties of FRMMCs..... | 9 |
| 1.2.6 Applications of FRMMCs | 12 |
| 1.2.7 Fabrication of FRMMCs | 13 |
| 1.2.8 SiC fiber reinforced nickel matrix composites..... | 15 |
| 1.3 Carbon nanomaterials reinforced metal matrix composites | 17 |
| 1.3.1 Carbon nanomaterials..... | 17 |
| 1.3.2 Carbon nanomaterials as reinforcements in composites | 22 |
| 1.4 Electrodeposition of carbon nanomaterials-metal matrix composites | 23 |
| Chapter 2 Technology of Electrodeposition | 25 |
| 2.1 Introduction | 25 |
| 2.2 Formation mechanism of deposited layers..... | 27 |
| 2.2.1 Step-edge ion-transfer mechanism | 28 |
| 2.2.2 Mechanism of terrace ion-transfer | 29 |
| 2.2.3 Mechanisms of growth..... | 30 |
| 2.3 Electrochemical deposition cell and its components | 32 |
| 2.4 Parameters of the process and their effect on electrodeposition..... | 33 |

| | | |
|-----------|--|----|
| 2.4.1 | Deposition time and thickness (Faraday's law) | 34 |
| 2.4.2 | Current density | 36 |
| 2.4.3 | Electrode potential | 37 |
| 2.4.4 | Composition and conductivity of deposition baths | 40 |
| 2.4.5 | Bath additives | 41 |
| 2.4.6 | Temperature of the bath | 42 |
| 2.4.7 | Substrate surface | 43 |
| 2.4.8 | pH of the bath | 43 |
| 2.4.9 | Stirring of the bath | 43 |
| 2.4.10 | Hydrogen evolution and embrittlement | 44 |
| 2.4.11 | Current and metal distribution | 44 |
| 2.5 | Structure and properties of electrodeposits | 46 |
| 2.6 | Electrodeposition of alloys | 48 |
| 2.7 | Electrodeposition of composites | 49 |
| 2.8 | Applications | 51 |
| Chapter 3 | Materials and Methods | 54 |
| 3.1 | Materials | 54 |
| 3.1.1 | Metal matrices | 54 |
| 3.1.2 | Reinforcements | 55 |
| 3.1.3 | Surfactants or dispersing agents | 57 |
| 3.1.4 | Conducting substrates | 58 |
| 3.1.5 | Deposition baths | 59 |
| 3.2 | Methods | 60 |
| 3.2.1 | Electrodeposition of fiber reinforced composites | 60 |
| 3.2.2 | Electrodeposition of carbon nanomaterials reinforced composites | 63 |
| 3.3 | Techniques used for characterizing the electrodeposited composites | 65 |

| | | |
|--------------|---|-----|
| 3.3.1 | Optical microscopy..... | 66 |
| 3.3.2 | Stereo microscopy | 69 |
| 3.3.3 | Scanning electron microscopy..... | 71 |
| 3.3.4 | X-ray diffraction..... | 73 |
| 3.3.5 | Mechanical characterizations..... | 79 |
| 3.3.6 | Techniques for dispersion of carbon nanomaterials | 85 |
| 3.3.7 | Thermal characterization | 88 |
| 3.3.8 | Tribological characterization | 89 |
| Chapter 4 | Results and Discussions..... | 93 |
| 4.1 | Ni-SiC long fibers composites..... | 93 |
| 4.1.1 | Optimization of electrodeposition parameters..... | 93 |
| 4.1.2 | Feasibility of producing composites | 95 |
| 4.1.3 | Study of interfaces..... | 101 |
| 4.1.4 | Production of the composites | 104 |
| 4.1.5 | Mechanical properties | 104 |
| 4.1.6 | Fracture behavior..... | 109 |
| 4.1.7 | EDS analysis | 116 |
| 4.2 | Ni-GNP and Ni-GO composites..... | 119 |
| 4.2.1 | Dispersion stabilities of carbon nanomaterials | 119 |
| 4.2.2 | Production of the composites | 122 |
| 4.2.3 | Hardness and grain size measurements..... | 124 |
| 4.2.4 | Wear and friction behavior | 125 |
| Chapter 5 | Conclusions..... | 131 |
| 5.1 | Fibers reinforced metal matrix composites | 131 |
| 5.2 | Carbon nanomaterials reinforced metal matrix composites | 133 |
| Bibliography | | 135 |

Abstract

The research work of this PhD thesis was done on the study, production and characterization of two types of metal matrix composites: 1) fiber reinforced metal matrix composites and, 2) carbon nanomaterials reinforced metal matrix composites.

In fiber reinforced metal matrix composites, a metal or an alloy is reinforced with continuous or discontinuous fibers in order to improve the specific strength and stiffness at high temperatures. For example superalloys are the typical materials for the hot parts of aeronautic engines. They are very important in the aerospace field as they offer high temperature mechanical strength together with a good resistance to oxidation and corrosion. But due to high temperatures involved in the service conditions, buckling of the material may occur. In order to avoid this high temperature buckling phenomena, a reinforcement of the superalloy could be needed to maintain the mechanical properties. For this reason it was thought to investigate the possibility of realizing continuous fibers reinforced metal matrix composites over the superalloys that can further improve the high temperature properties. Due to its simplicity and viability, electrochemical deposition was chosen as the production technique to produce this kind of composite materials. The selected substrate for electrodepositing the nickel matrix composite was nickel based superalloy Inconel-718, and monofilament continuous silicon carbide fibers were chosen as reinforcement.

First of all chemical compatibility was studied between the nickel matrix, superalloy and silicon carbide fibers, both in the uncoated form, and coated with carbon or carbon/titanium diboride. Both theoretical calculations and experiments were conducted, suggesting the use of a carbon coating over fibers and a buffer layer of nickel to increase the interface quality as well as to avoid unwanted reactions between substrate and silicon carbide fibers. After studying the chemical feasibility of all the related components, electrodeposition of the composites was performed in order to demonstrate the practical feasibility of the process. Then final composites were deposited on the dog-bone shaped specimens of Inconel-718. The produced composites were subjected to mechanical tests in order to evaluate the mechanical properties at room temperature and at high temperatures (400 °C and 600 °C). Evaluation of the results shows improvement in the yield strength of the produced composites with respect to the

superalloy alone at room temperature. There is a decrease in the yield strength at high temperatures due to the failure of the interface between the superalloy and the composite layer but it is demonstrated that if a hot pressing treatment is done, then the interface strength is retained at high temperature and thus yield strength values will also increase.

Fracture analysis and EDS analysis were also performed on the fractured surfaces of the samples with the help of field emission scanning electron microscope in order to study the fracture mechanisms involved and the composition of the interface after their testing at high temperatures. The fracture mechanisms in Ni/SiC composite layer was of debonding and pull out type which is typical characteristic of the fiber reinforced composites. The superalloy fractures with ductile behavior at room temperature. At temperatures of 400 °C and 600 °C, the superalloy fails with more ductile character after extensive amount of plastic deformation before its fracture.

Carbon nanomaterials are widely being used to reinforce the metallic materials in order to improve their electrical, thermal, corrosion, wear and friction resistance for particular applications. In this part of the research work, graphene nanoplatelets (GNPs) and graphene oxide (GO) were chosen as nano reinforcements to produce nickel matrix nanocomposites with the intention to evaluate their wear and friction behavior. Graphene nanoplatelets and graphene oxide consist of few layers of graphene and graphene oxide respectively and their layered structure coupled with the small size of these materials can be helpful reducing the wear rate of the composites. Crystallite size, hardness and roughness of the coatings were also studied in order to understand the effect of nano phases on these properties.

Again the production technique employed consists of electrodeposition of the composites over a conducting steel substrate. A lot of work has been done in producing metal matrix composites reinforced with carbon nano fibers, carbon nanotubes and graphene. But graphene nanoplatelets and graphene oxide are not much evaluated for reinforcing the metallic matrices especially with the electrodeposition technique. To produce these types of composites by electrodeposition, a uniform and stable dispersion of the carbon nanomaterials in the nickel deposition baths is necessary. So particular attention was given to this aspect and uniform and stable dispersions were obtained by using a suitable

dispersant, chosen after a wide screening, namely poly sodium styrene sulphonate (PSS). The dispersing technique employed the ultrasonication of the deposition bath with the help of an ultrasonic probe. The obtained coatings were strong and well adherent to the steel substrate, and presented rather well dispersed graphene oxide or graphite nanoplatelets, even if some agglomerates were still present in samples obtained from highly concentrated suspensions.

The nanocomposites were characterized in terms of microhardness, crystallite size, roughness and wear and friction behaviors. The composites with GO show very little effect on the microhardness whereas Ni/GNP composites show slight increase in the hardness. The effect on the crystallite size is not significant. Low concentration of the nano phase gives the composites a good smooth surface with less roughness whereas, by increasing the concentration of the carbon nanomaterials, the composites produced presents a rougher surface. Pin-on-disk tests were chosen to evaluate the wear behavior of the composites. The obtained results demonstrated a significant decrease in the wear rate, percent mass loss and volume loss of the composites as compared to the pure nickel one. The worn tracks observations suggest that the nanocomposites were worn by adhesive wear mechanism.

Chapter 1 Metal Matrix Composites

1.1 Introduction

The mixture of two or more different type of materials in which all the mixed materials retain their physical and chemical and physical identities is called composite. The phase which forms a continuous network and that surrounds the other phases is called matrix whereas; the discontinuous and dispersed phase is called the reinforcement. The reinforcements can be of various types, shapes and geometries e.g. fibers, whiskers, particles etc. The matrix can be metal, polymer or ceramic whereas the reinforcements are generally ceramic in nature, although in some cases metallic and polymeric reinforcements are also used. Composite materials can be classified on two bases; the type of matrix material, and the size, shape and geometry of the reinforcements. The classification of composites on the basis of matrix material used is shown in Figure 1.1, while the classification based on the shape and geometry of the reinforcements is shown in Figure 1.2.

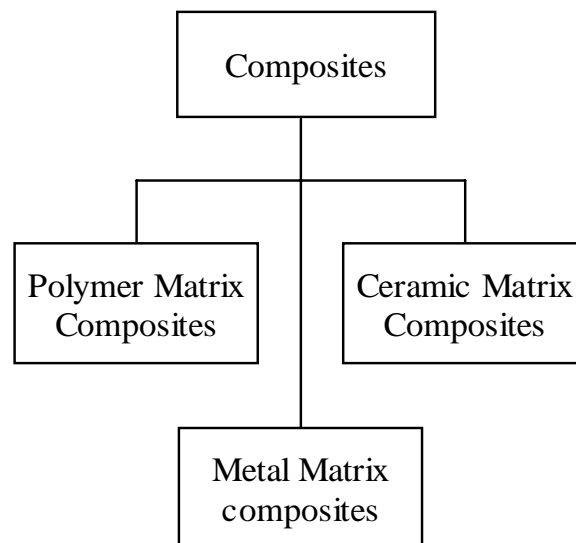


Figure 1.1: Classification of composites on the basis of matrix materials

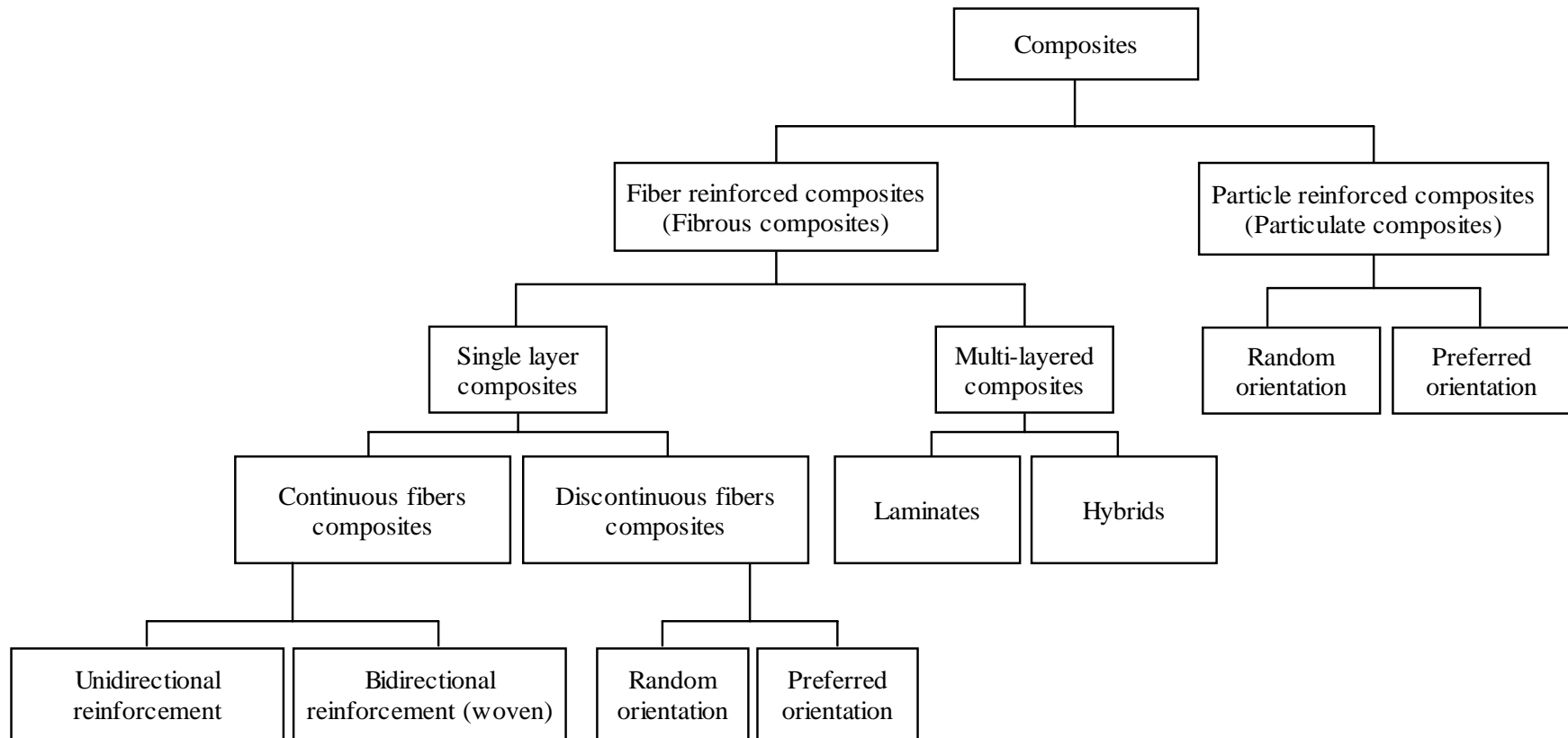


Figure 1.2: Classification of composites on the basis of reinforcement

The composite materials in which matrix phase used is a metal or an alloy, they are called metal matrix composites (MMCs). Metal matrix composites are divided into many types depending upon the size and shape of the reinforcements. There are following four main types of MMCs:

1. Particle-reinforced MMCs
2. Short fiber- or whisker-reinforced MMCs
3. Continuous fiber- or sheet-reinforced MMCs
4. Laminated or layered MMCs

The arrangement of reinforcements in these types is shown in Figure 1.3.

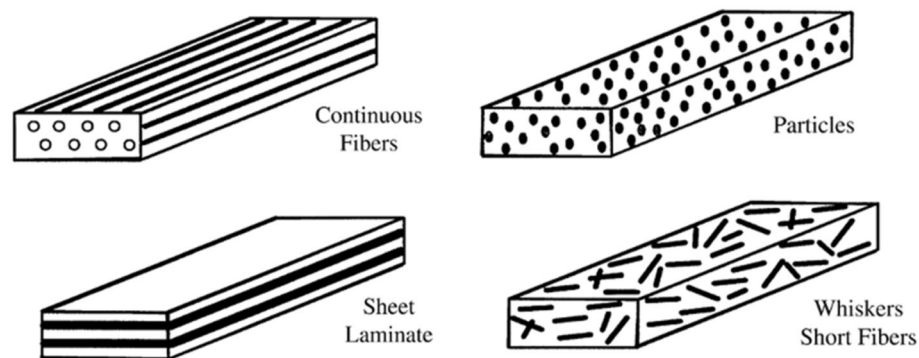


Figure 1.3: Classification of metal Matrix Composites on the basis of reinforcements.

Metal matrix composites have always been attractive for the material scientists and engineers as a substitute for the pure metallic materials and some traditional pure ceramics. The main idea behind the preparation of metal matrix composite is to develop a material that has nearly the same high strength as the ceramics but at the same time it also has high fracture toughness that comes from the tough matrix of the metal. This idea has led to the production and development of a new family of the materials named as metallo-ceramic composites (Breval 1995). Composites with metallic matrices give many advantages over the traditional materials. Metal matrix composites are capable to be designed to give the required type of properties for specific applications. For example they provide good stiffness and strength (Ward-Close & Robertson 1996; Ward et al.

1996), even good at high temperatures (LLORCA 2002; Tjong & Ma 1997). In addition to high strength and stiffness, MMCs also give high electrical and thermal conductivity (Weber et al. 2003; Koráb et al. 2002), improved friction resistance (Ghosh et al. 2013), wear resistance (Berns 2003) and corrosion resistance (Blackwood et al. 2000; Chen & Mansfeld 1997; Shimizu et al. 1995).

1.2 Fiber reinforced metal matrix composites (FRMMCs)

There are a lot of possible combinations of matrices and reinforcements that can be used to produce fiber reinforced metal matrix composites which are discussed in next sections.

1.2.1 Metallic matrices

There are a lot of metals and their alloys which are being used as matrices in metal matrix composites. The examples are aluminum and aluminum alloys, nickel and nickel alloys, copper, zinc, titanium and titanium alloys etc. Properties of some commonly used metals as the reinforcements in metal matrix composites are shown in the Table 1.1.

Table 1.1: Properties of some common used metallic matrices

| Metal | Structure | Density | Melting point | Thermal Expansion | Young's modulus |
|-------|-----------|-------------------------------|--------------------|---|-----------------|
| | | $\text{g}\cdot\text{cm}^{-3}$ | $^{\circ}\text{C}$ | $\mu\text{m}\cdot\text{m}^{-1}\cdot\text{K}^{-1}$ (at 25 $^{\circ}\text{C}$) | (GPa) |
| Ti | CPH | 4.50 | 1668 | 8.6 | 116 |
| Cu | FCC | 8.96 | 1085 | 16.5 | 120 |
| Ni | FCC | 8.90 | 1455 | 13.4 | 200 |
| Fe | BCC | 7.87 | 1538 | 11.8 | 211 |
| Al | FCC | 2.70 | 660 | 23.1 | 70 |
| Zn | CPH | 7.14 | 420 | 30.2 | 108 |

Metals and the metallic alloys have good toughness and strength but they lack in the stiffness especially at higher temperatures. So they are reinforced with the more stiff ceramic materials in order to increase their stiffness. Another advantage apart from the

stiffness improvement is that ceramic reinforcements are low in weight so the specific weight of the metals is decreased by reinforcing them with these reinforcements.

Apart from the pure metals, the composite materials can also be obtained by using their alloys as matrices for specific applications. For example aluminum and titanium alloys which have very low density, good toughness, excellent strength and also good resistance to corrosion. So they are widely used as matrices to prepare composites for aerospace and automotive fields.

1.2.2 Fiber reinforcements

Different types of fiber reinforcements are used for making the metal matrix composites. The fibers used as reinforcements can be continuous long fibers or discontinuous fibers. The discontinuous fibers have further two types namely; short fibers and whiskers. An important factor associated with the fiber composites is the aspect ratio of fibers. Aspect ratio is basically the ratio of length to the diameter of the fibers. So the continuous long fibers have very high aspect ratio but the discontinuous fibers have relatively small aspect ratios. The most of the reinforcements are ceramic in nature. Although ceramic fiber reinforcements are expensive but they are commonly used in making metal matrix composites because they have very high elastic modulus even at higher temperatures. Some common continuous and discontinuous fibers being used in metal matrix composites are shown in the Table 1.2.

Table 1.2: Different materials used as fiber reinforcements

| Fiber Type | Materials | |
|----------------------|---|---|
| Continuous fibers | Al_2O_3 , $\text{Al}_2\text{O}_3+\text{SiO}_2$, C, SiC, B, Si_3N_4 , Nb-Ti, Nb_3Sn | |
| Discontinuous fibers | short fibers | Al_2O_3 , SiC, ($\text{Al}_2\text{O}_3+\text{SiO}_2$), Vapor grown carbon fiber |
| | whiskers | SiC, TiB_2 , Al_2O_3 |

1.2.3 Silicon carbide fibers

Among the long fibers, silicon carbide fiber is the most common ceramic fiber that is used for making metal matrix composites. In the silicon carbide fiber, bonding between Si and C is covalent and due to this strong bonding they are brittle fibers having high modulus. But there is one problem with SiC fibers which is their higher density that causes a decrease in their specific properties as compared to the carbon fibers. Silicon carbide fibers can be produced by the decomposition of a precursor or by chemical vapor deposition (CVD) on a substrate like tungsten. Properties of the silicon carbide fibers are given in the Table 1.3.

Table 1.3: Properties of different types of SiC fibers

| Type of Fibers | Density ρ (Mg/m ³) | Young's Modulus (GPa) E_f | Tensile Strength (MPa) σ_{Tf} | E_f/ρ | σ_{Tf}/ρ |
|---------------------------|---|-----------------------------------|--|------------|--------------------|
| Nicalon | 2.60 | 250 | 2200 | 96.2 | 846 |
| CVD monofilament (W-core) | 3.05 | 406 | 3920 | 133.1 | 1258 |
| CVD monofilament (C-core) | 3.00 | 400 | 3450 | 133.3 | 1150 |
| Tyranno | 2.40 | 280 | 2000 | 116.7 | 833 |
| Whisker | 3.20 | 700 | 10000 | 218.8 | 3125 |

1.2.4 Role and characteristics of interface

The boundary where the matrix and the reinforcements meet is called the interface. It is basically a bi-dimensional boundary between the two meeting entities. In composite materials, the interface is very important because most of the properties e.g. Young's modulus and strength of the composites depend upon the type and characteristics of the interface. In case of load bearing applications, it is the interface who transfers the load from the matrix to the reinforcements. So it should be strong enough to be capable of performing this task.

The bonding between the interface and reinforcement can be of following types:

- Mechanical bonding

- Chemical bonding
- Electrostatic bonding
- Reaction or inter-diffusion bonding

A schematic representation of all four types of interface bonding is shown in Figure 1.4.

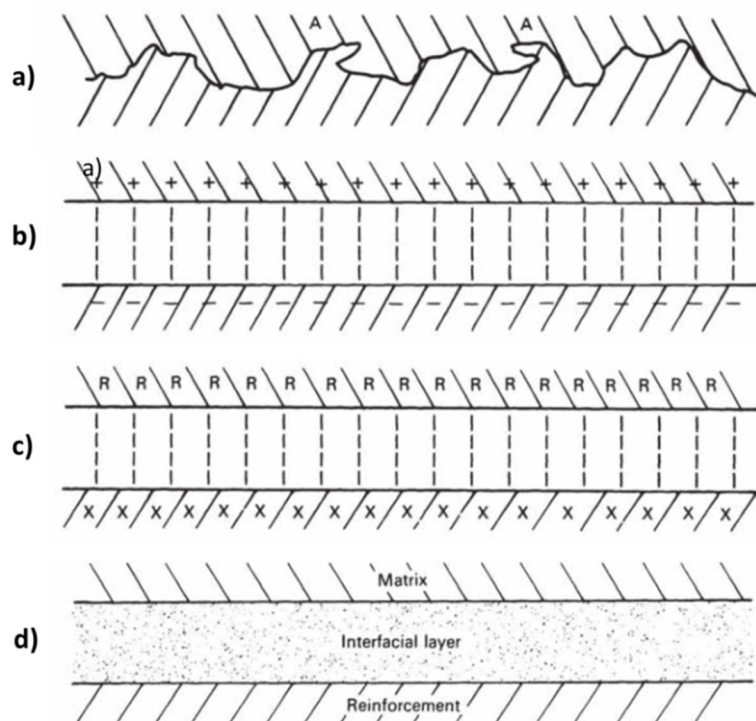


Figure 1.4: Different types of bonding at the metal-reinforcement interface (Mathews & Rawlings 1999)

Mechanical bonding is the interlocking of the two surfaces at the points of contacts (Figure 1.4a). If the meeting surfaces are rough, the mechanical bonding will be strong and hence the stronger is the interface as well. This type of bonding is more strong and useful when the applied forces act parallel to interface because shear strengths are considerable in this case.

Electrostatic bonding occurs between the two oppositely charged surfaces. If among the components of the composite one is charged positively and the other negatively then an electrostatic interaction occurs between them when they come close to each other. This attraction causes an interfacial bonding between the surfaces (Figure 1.4b). Electrostatic bondings are only operative in very small regions as they are of short range type interactions.

Chemical bonding is the type of bonding in which a chemical bond is formed between the surfaces when they are having some chemical groups on them that can react with each other. If a chemical group X is present on the matrix and another chemical groups R is present on the fiber, a chemical bond X-R will develop that will cause a chemical bonding between the matrix and the interface (Figure 1.4c).

Inter-diffusion or reaction type bonding occurs when the molecules or atoms of the matrix and reinforcement diffuse into each other at the interface. Due to this inter-diffusion, an interfacial layer is developed between the combining surfaces. This interfacial layer has a certain thickness and it has different characteristics (e.g. structure, composition and strength) than both of the matrix and reinforcement. The effect of inter-diffusion becomes greater at higher temperatures.

In addition to the bonding mechanisms, another important consideration is the wetting of the fibers by the metallic matrices. To have a good interface and good interface bonding, the wettability has to be good. If we consider the metal in the molten state, the good wettability is said to be achieved when the liquid metal flows over each and every bump and dip of the reinforcement surface. Low viscosity metal matrices will have good wettability which is achieved when free energy of the interface is decreased.

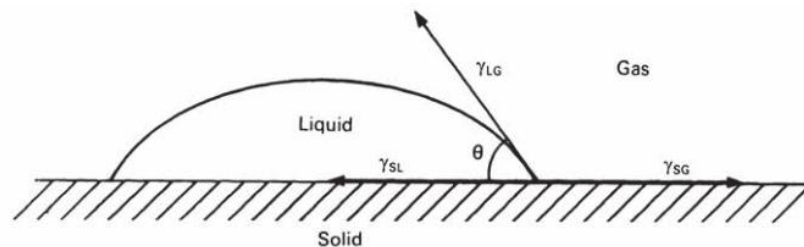


Figure 1.5: A liquid in equilibrium with a solid with contact angle θ

The free energy of the interface (J/m^2) can be taken equal to the surface tension (N/m). At equilibrium,

$$\cos \theta = \frac{(\gamma_{SG} - \gamma_{SL})}{\gamma_{LG}}, \quad \text{Eq. 1.1}$$

Where θ is the contact angle and acts as measure of degree of the wetting of a liquid on a particular surface. When $\theta = 180^\circ$, the liquid drop is completely spherical and there is

no wetting. When contact angle is zero, there is perfect wetting achieved. Between 0° and 180° , the wettability increases as the θ decreases. Generally, it is said that when $\theta > 90^\circ$, the liquids do not wet the solids.

1.2.5 Mechanical properties of FRMMCs

Among the mechanical properties of the fiber reinforced metal matrix composites, strength and elastic modulus are more important which is the main purpose of incorporation of long fibers.

1.2.5.1 Elastic modulus

Elastic modulus or Young's modulus is a very important property to consider in case of fiber reinforced metal matrix composites. The values of elastic modulus for the MMCs depend on the individual properties of the matrix material as well as the reinforcement. The size, shape, distribution and volume fraction of the reinforcement is very important that have profound effects on the mechanical properties. Also the characteristics of interface between metal matrix and the reinforcement also dictate the mechanical properties of metal matrix composites.

Elastic modulus of the composites when the force applied is in longitudinal direction (Figure 1.6a) can be calculated simply by applying the rule of mixtures by the following equation:

$$E_{CL} = V_f E_f + (1 - V_f) E_m \quad \text{Eq. 1.2}$$

Where the subscripts E and V stands for the elastic modulus and volume fractions and subscripts c , f and m stands for the composite, fiber and matrix respectively. The L subscript used means the load is applied in longitudinal direction.

The Equation 1.2 is applicable only in case of longitudinal loading of the composites. And it considers the assumptions that the amount of elastic deformation in both the matrix and the reinforcement is same and also the bonding between them is perfect.

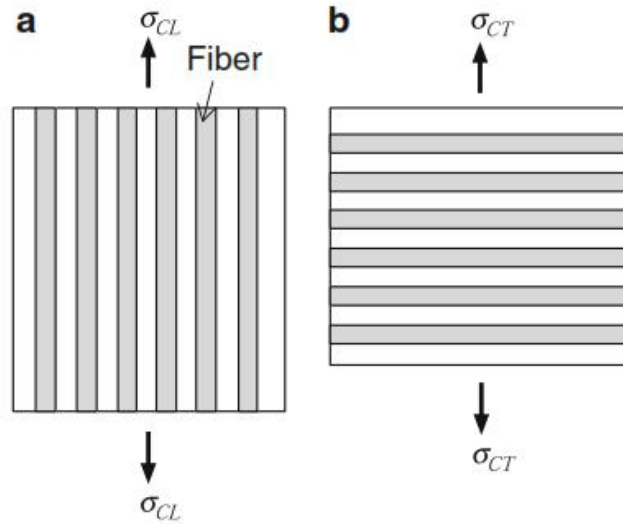


Figure 1.6: Longitudinal (a) and transfer (b) loading of the FRMMC (Nishida 2013)

If the load applied is in a direction perpendicular to the axis of fibers' arrangement, then the elastic modulus of the fiber reinforced composite is calculated by the equation:

$$E_{CT} = \frac{E_f E_m}{E_m V_f + E_f (1 - V_f)}. \quad \text{Eq. 1.3}$$

Here the subscript E_{CT} means the elastic modulus of composite when it is loaded in transverse direction (Figure 1.6b). This equation considers that in case of loading of the composite perpendicular to the axis of fibers, the stress acting on the fibers as well as the matrix is same.

1.2.5.2 Strength

The main goal of producing metal matrix composites is to obtain high strength. The strength of these composites mainly depend upon the strength and arrangement of the fiber reinforcement, reaction or bonding nature at the metal/fiber interface and crack propagation mechanism (Nishida 2013).

If we assume the longitudinal loading and a perfect interface between matrix and reinforcement with same elastic deformations in the fiber and matrix metal, then the strength of the metal matrix can be calculated by the following equation:

$$\sigma_c = \sigma_{ff}V_f + \sigma'_m(1 - V_f) \quad \text{Eq. 1.4}$$

Where σ_c represents the composite strength and σ_{ff} denotes the fiber's fracture strength. Also V_f stands for volume fraction of the fibers and σ'_m is the stress shared by the metal matrix when the fiber reaches its fracture stress. Normally the fibers reach their fracture stress before the metallic matrix because of their brittleness. In the Figure 1.7, σ_μ is the fracture stress of metal matrix and normally $\sigma'_m < \sigma_\mu$

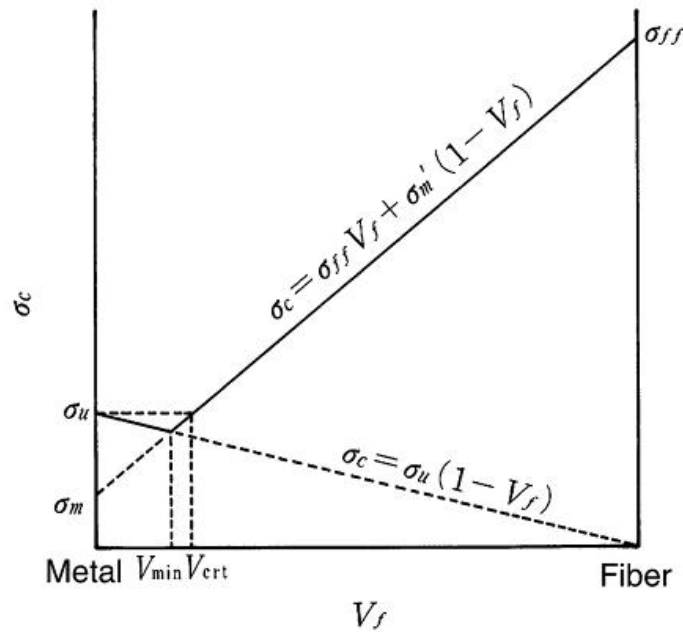


Figure 1.7: Relation between tensile strength (σ_c) and volume fraction (V_f) of the continuous fiber reinforced metal

Also σ_μ and σ'_m coincides which each other when the fracture strains in the matrix metal and the fiber are same i.e $\sigma'_m = \sigma_\mu$. And also if the fibers' volume fraction V_f is smaller than a value V_{min} , in this case there is no fracture in the composite even after the fiber has reached its fracture stress and and has fractured. In this case the composites goes on deforming by the mechanism of work hardening and composites fails at a stress higher than the stress calculated by the Equation 1.4. Now the fracture stress of the composite is given by the equation:

$$\sigma_c = \sigma_u(1 - V_f) \quad \text{Eq. 1.5}$$

So for the strength contribution from the fibers to the composite, V_f should be greater than V_{min} . This V_{min} can be given by the equation:

$$V_{min} = \frac{\sigma_u - \sigma'_m}{\sigma_{ff} + \sigma_u - \sigma'_m}. \quad \text{Eq. 1.6}$$

And if it is required to get the higher strengths of the composites than the matrix material, then volume fraction of the fiber V_f should be higher than a critical value of fiber volume fraction V_{crt} as given by the following equation:

$$V_{crt} = \frac{\sigma_u - \sigma'_m}{\sigma_{ff} - \sigma'_m}. \quad \text{Eq. 1.7}$$

High strength is typically a target of composite materials development. However, there are many factors which influence the strength of composites, and it is very difficult to estimate the strength of a composite precisely. In a fiber reinforced composite, the strength of fibers has a distribution and is not uniform. Many factors including fiber arrangement and distribution, chemical reaction products at the fiber/matrix interface and crack propagation after crack formation influence the strength of a composite.

1.2.6 Applications of FRMMCs

Metal matrix composites reinforced with discontinuous fibers or whiskers and particles are more commonly used in auto motive industry, aerospace and air craft industry (Kainer 2006; Nishida 2013; Tjong & Ma 1997; MIRACLE 2005) and automobile industry (Kainer 2006; Allison & Cole 1993; Davim 2012). But the use of fiber reinforced metal matrix composites is still limited due to high costs and complication of production processes. Although fiber reinforced metal matrix composites may not be so appealing in terms of their high costs and the difficulty of their production but there are some applications where the use of these composites is advantageous due to their enhanced mechanical and thermal properties over conventional materials. And below are few examples of the applications of fiber reinforced metal matrix composites

Space is always a challenge for the engineers and they are trying to get better and better materials with sufficient strength and stiffness but at the same time of as low

weight as possible. For space applications, the first metal matrix composites used successfully was the boron fiber reinforced aluminum matrix composite for the fabrication of tubular struts and rib truss members to be used in the middle part of fuselage section. Also the same B/Al composite was applied to prepare the space shuttle orbiter landing gear drag link. Graphite reinforced aluminum matrix composite (Gr/Al) is used in making antenna of the Hubble space telescope. The good electrical conductivities of MMCs make them usable to serve for transferring the electrical signals between spacecraft and antenna dish (Rawal 2001)

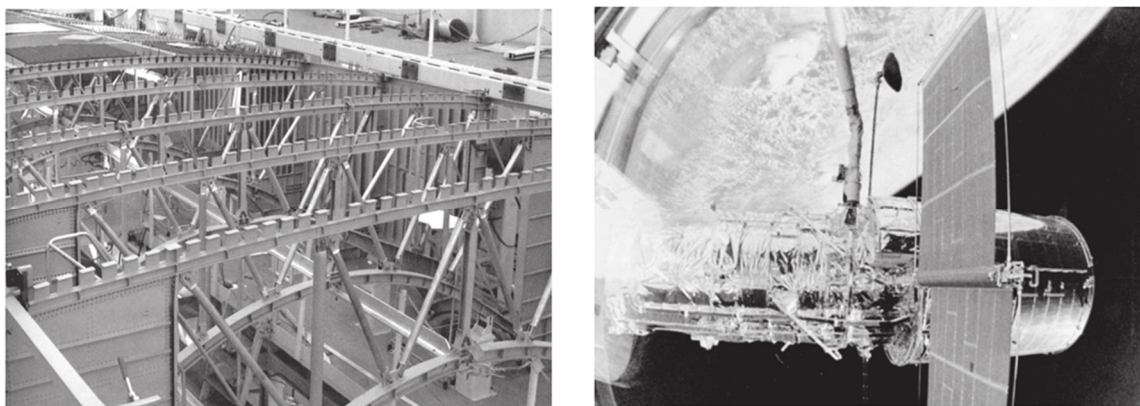


Figure 1.8: Fuselage structure of space shuttle orbiter having B/Al MMC tubes (left) and Hubble telescope antenna made of Gr/Al MMC (right)

Fibers reinforced nickel, aluminum and copper matrix material systems are also being potentially applied for the applications in liquid rocket engines as high-stiffness flanges and ductwork, rotating machinery and turbopump housings (Shelley et al. 2001).

1.2.7 Fabrication of FRMMCs

The fabrication techniques like conventional casting, squeeze casting, powder metallurgy etc. that are commercially applied for the short fibers or whiskers and particle reinforced metal matrix composites (Harrigan 1998) cannot be feasibly applied for the production of continuous fiber metal matrix composites. The reason is obvious i.e. the length of the fibers. For making the long fiber composites there are following possibilities:

- Drawing of fibers from the pool or bath of liquid matrix metal
- Wounding the fibers on a mandral and their binding into sheets of fibers and then hot pressing between the sheets of matrix material

- Electrodeposition of matrix on the fibers arranged on a substrate

A brief detail of these three techniques follows in the following paragraphs.

The first technique is usually used for small diameter fibers ranging from 10 to 15 μm . It has been used by 3M in the USA for making continuous Al_2O_3 fibers reinforced aluminum wires in which the bundles of alumina fibers are drawn from the liquid bath of the aluminum metal. This technique is also being commercially used by Nippon Carbon in Japan for producing silicon carbide fiber reinforced aluminum matrix composite wires.

The second technique is used for large diameter fibers that can range from 100 to 140 μm . In this technique, first of all the fibers are wound on to a large diameter mandral or drum, usually of one meter diameter, and bounded together with the plasma projection of the material that is being used as matrix. Organic binder can also be applied to hold the fibers together but in this case the fiber has to be removed in the later stages. Both of these binding strategies allow the removal of the fibers from the mandral by cutting the fiber sheet along the mandrel axis. As a result a sheet of the fibers positioned close to each other is obtained. This cut sheet of fibers is then placed between the sheets of matrix metal into a mould and hot pressing is done to obtain the final composites. The overall process takes place at high temperature that allows the diffusion bonding between fibers and the matrix material. But off course the temperature is well below the melting point of the matrix metal. An example for the practical use of this method is the production of space shuttle tube frames by boron reinforced aluminum matrix composites (Bunsell & Renard 2005).

Another process that can be used to manufacture the long fiber reinforce metal matrix composites is the process of electrodeposition that is also used in this particular study to prepare this type of composites. The advantages of electrodeposition process for the production of long fiber reinforced composites are that this process is very simple and it does not require higher temperatures of processing and can be carried out at room temperature. It will need just the electrolytic bath of the matrix metal and the fibers arranged onto a substrate. The substrate is then suspended in the deposition bath to deposit the matrix metal.

1.2.8 SiC fiber reinforced nickel matrix composites

In this particular study, the nickel metal was chosen as the matrix material. The reason for choosing this metal was because it was required to increase the properties of Inconel-718 with fiber reinforced metal matrix composite. So the nickel as the matrix could be more suitable as it's the main constituent element of the Inconel nickel super alloy. Superalloys are widely used at medium and high temperature, where high strength and creep resistance are needed. They exist with various compositions; however in high temperature applications nickel superalloys are most often employed. Inconel 718 is the most frequently used nickel-based alloy, accounting for a high share of the annual volume production for both cast and wrought nickel-based alloys (Ezugwu et al. 2003). Due to its superior high temperature mechanical properties, such as high yield and ultimate tensile stress, resistance to corrosion and oxidation, it has been widely used for parts in aerospace industry and nuclear reactors (Liao & Shiue 1996)

In aeronautic engines, superalloys can be used from the rear stages of the High Pressure Compressor (HPC) to the Low Pressure Turbine (LPT). However, since they are metallic materials, they suffer from a significant stiffness reduction at high temperature (Fukuhara & Sanpei 1993; Sieborger et al. 2001), so that the use of composites could be envisaged, in order to increase high temperature stiffness to avoid the buckling phenomenon. Indeed, metal-matrix composites (MMCs) are very attractive engineering materials since their properties can be enhanced or tailored through the addition of selected reinforcement (Chawla & Chawla 2013; Ceschini & Montanari 2011). However, superalloy based composites were rarely considered in the past (Kandeil et al. 1984; Kao & Yang 1990), preferring monocrystalline or directional solidified alloys to improve high temperature behavior (Broomfield et al. 1998; Han et al. 2011; Bürgel et al. 2004). In this work, we propose a novel approach to the increase of stiffness at high temperature, by superposing a stiff composite layer produced by electrodeposition over a superalloy substrate.

Electrodeposition methods have been much studied in the past for the production of coatings containing reinforcing particles (Garcia et al. 2003; Jung et al. 2009; Srivastava et al. 2007; Gyftou et al. 2008; Robin et al. 2009; Zhu et al. 2007; Shrestha et al. 2003). The matrix of these composite coatings is often nickel or copper, while the reinforcement is generally chosen to improve wear or corrosion resistance, even if other

applications are possible, for instance low attrition surfaces by using fluorinated polymers particles. No significant modification of the well-known electrodeposition process is needed for obtaining Ni/SiC composites over the superalloys, since it is sufficient to suspend the superalloy support in the deposition bath.

The preparation of fiber-reinforced composites by electrodeposition technique is instead rarely described in literature (Suchentrunk 2004; Chou et al. 1985; ZHU et al. 1997). In 1970 Divecha and co-workers (Divecha & Church 1970) patented a method for the preparation of such materials, and in the late 70s and early 80s a few works were performed on this subject (Suchentrunk 2004; Chou et al. 1985). Here mostly copper or aluminum matrices were considered, with boron fibers as reinforcement, for the production of pressure vessels for space applications. More recently, copper-carbon or silicon carbide fiber composites were realized by electrodeposition followed by hot pressing (Luo et al. 2007; Wan et al. 2000; Tecchio 1997), with the goal of coupling high mechanical properties with good thermal and/or electrical conductivity. Finally, carbon nanotubes and carbon nanofibers based composites were also realized (Arai & Endo 2005; Wang et al. 2005; An et al. 2008; Arai 2004; Guo et al. 2008), with copper or nickel matrices. In this case however the fibers are not continuous and the system is rather similar to one concerning the deposition of particle-reinforced composite coatings.

The first goal of the present study was to understand the chemical compatibility of Inconel 718 superalloy with nickel/silicon carbide fibers based composite. Even if different metals can be easily deposited by electrodeposition, nickel seems the best choice, both because its deposition is very well known and due to the fact that nickel is also the main constituent of Inconel alloys. Monofilament, high diameter fibers are needed for preparing a regular array, in order to improve the deposition of the matrix around the fiber itself. Due to their exceptional properties at room and high temperature, silicon carbide fibers were chosen. However, since such composite is designed to work at high temperature, it was deemed necessary to perform theoretical considerations and experimental analyses in order to choose the best coating for the silicon carbide fiber, with the goal of avoiding unwanted high temperature reactions between substrate, matrix and reinforcement. Once determined the best coating for the composite, a nickel-matrix composite reinforced with silicon carbide fibers was electrochemically deposited over a superalloy substrate, in order to show the practical feasibility of the process. After

that the final composites were prepared on dog-bone shape specimens in order to test them in mechanical testing machine after the production.

1.3 Carbon nanomaterials reinforced metal matrix composites

Metal matrix composites in which carbon based nanomaterials are used as reinforcements are called carbon nanomaterials reinforced metal matrix composites. They can be considered to fall under the category of particles reinforced metal matrix composites (Figure 1.4).

1.3.1 Carbon nanomaterials

Carbon is very important element in the periodic table that is found in abundance on earth. Its abundance rank in the earth's crust is 15 while it ranks at place 4 in the universe by mass. It is believed to known by man since 2500 BC in the forms of charcoal and soot. Carbon exhibits the property of allotropy and it has many allotropes out of which three very basic are graphite, diamond and amorphous carbon.

Most of the modern day carbon nanomaterials are made of crystalline allotrope of graphite. It consists of many layers of carbon atoms where these atoms are covalently bonded with each other forming hexagon shape structure. The layers are bound together by Van der Waals type of attraction. The crystal structure of graphite is shown in the Figure 1.9.

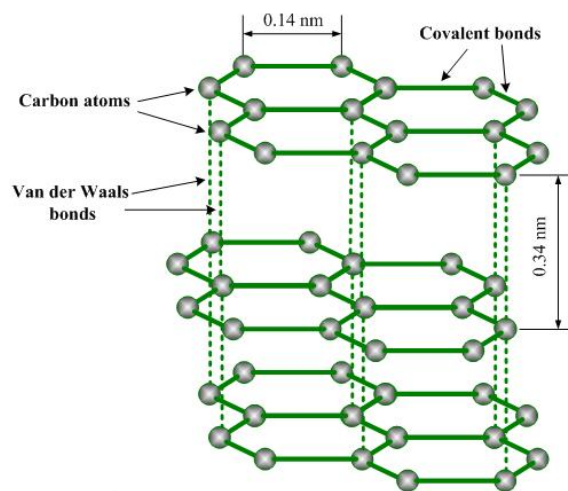


Figure 1.9: Crystal structure of graphite

The prominent carbon nanomaterials derived from crystalline graphite include fullerenes, carbon nanotubes, graphene and graphene oxide.

1.3.1.1 Fullerenes

Fullerenes are interesting allotropes of carbon which consists of a molecule made of 60, 70 or more number of carbon atoms. These were discovered in 1985 by Robert Curl and co-workers (Iijima & Ichihashi 1993) A C₆₀ fullerene forms a cage like structure having 20 hexagonal faces and 12 pentagonal faces. The structure of Fullerene C₆₀ is shown in Figure 1.10.

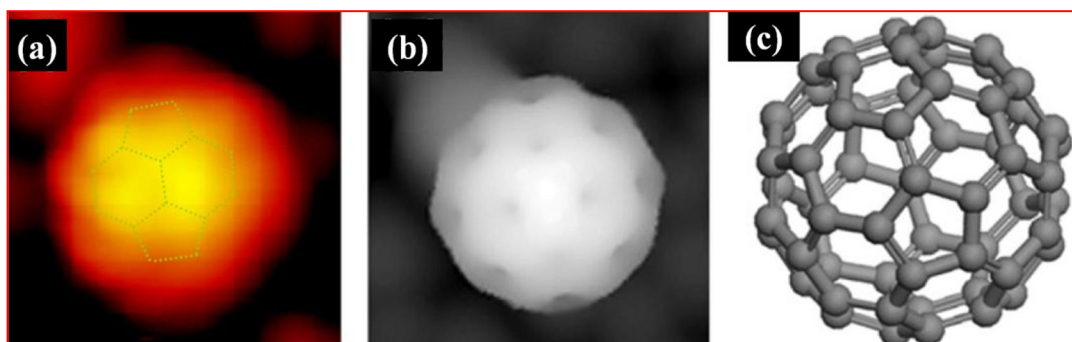


Figure 1.10: Structure of fullerene C₆₀ molecule; a) STM Image, b) simulated image and c) Molecular geometry (Muñoz et al. 2000)

Although fullerene has been discovered in 1985, but its mass production started after 1990 when a mass production method was invented by Krätschmer and Huffman (Thess et al. 1996). Because of their attractive physical and chemical characteristics, fullerenes are being widely used in many modern day applications e.g. in medical and biological, electronic and magnetic applications.

1.3.1.2 Carbon nanotubes

Carbon nanotubes are also member of fullerene family structures but with cylindrical shape instead of buckyball shape. CNTs were discovered by Iijima in 1991 (Bethune 1993). Carbon nanotubes consist of very small diameters of about few nanometers; but their length can vary from nanometers to several millimeters. These days carbon nanotubes are manufactured in many types e.g single or double wall carbon nanotubes, multiwall carbon nanotubes. The structure of carbon nanotubes is shown in Figure 1.11.

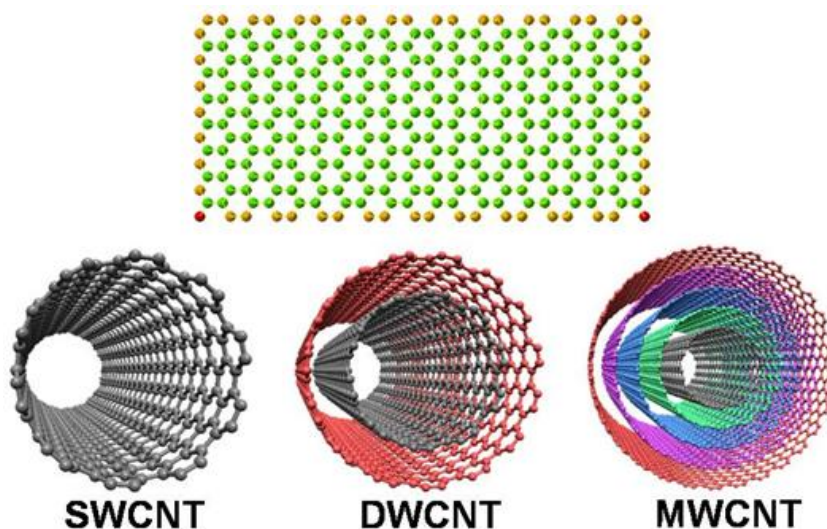


Figure 1.11: Different types of carbon nanotubes

Carbon nanotubes can also be classified on the basis of their chirality as depicted in Figure 1.12.

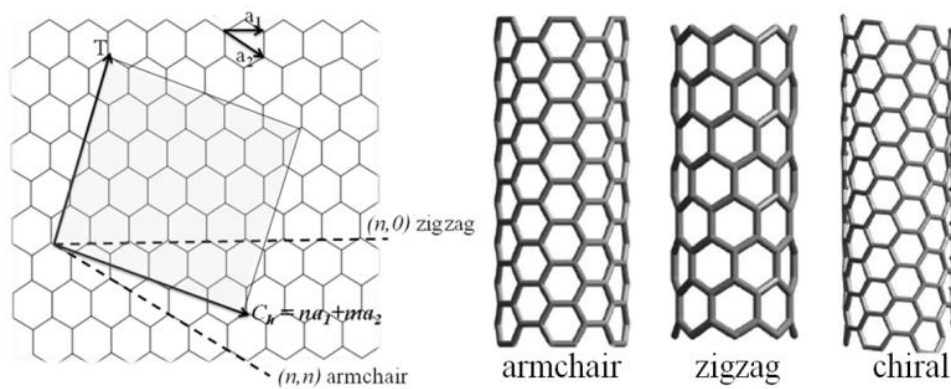


Figure 1.12: Classification of CNTs on the basis of chirality (Gupta 2011)

Carbon nanotubes have excellent mechanical properties like modulus of elasticity for example SWCNTs can reach to a Young's modulus value of terapascal (Cassell et al. 1999). They also have very good physical properties including thermal and electrical conductivity. Due to these fascinating properties they are very attractive to the research community to exploit them for various applications.

1.3.1.3 Graphene

Graphene is also a crystalline form of carbon that is one atomic thick layer of carbon atoms in two dimensions. Carbon atoms in the graphene structure are tightly packed into a honeycomb-like crystalline lattice in a two dimensional arrangement. The graphene serves as the basic building block of other allotropes of carbons and the carbon nanomaterials e.g. carbon nanotubes, fullerenes etc. because it can be molded by different ways to form other forms of carbon allotropes. For example by wrapping single layer of graphene up to zero dimensions, we get the fullerene. In the same way if graphene two dimensional sheet is rolled, one dimensional carbon nanotubes are obtained and if a lot of layers of graphene are stacked over one another we get three dimensional structure of graphite as explained in Figure 1.13 (Novoselov et al. 2004; Novoselov, Jiang, et al. 2005; Zhang et al. 2005).

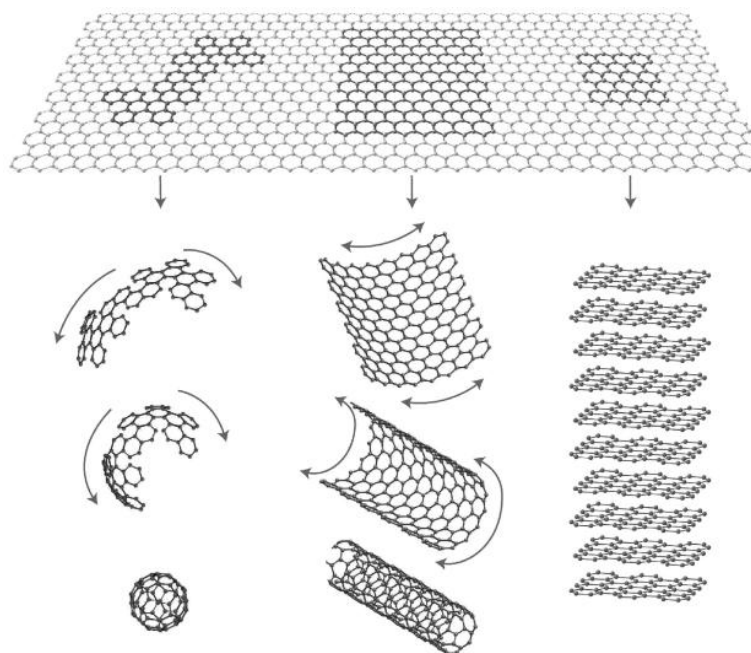


Figure 1.13: Scheme representation of graphene wrapping to form 0D fullerenes (left), 1D carbon CNTs (middle) or stacking to get 3D graphite (right) (Alwarappan & Kumar 2014).

Graphene has got very promising properties explored by various researchers. For example graphene has Young's modulus of 1100 GPa (Lee et al. 2008), fracture strength of 125 GPa (Lee et al. 2008), thermal conductivity of $5000 \text{ Wm}^{-1}\text{K}^{-1}$ (Balandin et al.

2008), charge carrier's mobility of $200000 \text{ cm}^2 \text{ V}^{-1}\text{S}^{-1}$ (Bolotin et al. 2008) and surface area of $2630 \text{ m}^2\text{g}^{-1}$ (Stoller et al. 2008)

Graphene is fabricated by numerous methods including mechanical exfoliation, depositions methods including chemical vapor deposition, plasma enhanced physical vapor deposition and thermal decomposition, by unzipping multiwall carbon nanotubes or can be synthesized by electrochemical methods (Tanaka 2014; Torres et al. 2014; Skákalová & Kaiser 2014; Choi et al. 2010).

1.3.1.4 Graphene nanoplatelets

Small stacks of graphene are said to be graphene nanoplatelets (GNPs). GNPs can be used to replace carbon nanotubes, nano clays, carbon fibers in many applications for example composite applications. GNPs also have excellent thermal, electrical characteristics and they impart these characteristics to the materials in which they are added to form composites. In addition to have good thermal and less permeable properties, they also have been noticed to improve mechanical properties like strength and stiffness of the composites as well.

1.3.1.5 Graphene oxide

As graphene is considered a single layer of graphite, similarly graphene oxide (GO) can also be taken as a single layer of graphite oxide (Figure 1.14). Graphite oxide is being produced since long as its first fabrication is reported to be done about 150 years ago (Novoselov, Geim, et al. 2005; Geim & Novoselov 2007). Graphene oxide is basically a compound made up of different varying ratios of carbon, oxygen, and hydrogen. It can be synthesized by using very strong oxidizers during the process of exfoliation of graphite or just by mechanical exfoliation of graphite oxide. Graphene oxide can also be fabricated having more than one layer as was the case for graphene nanoplatelets. Graphene oxide can be reduced to produce graphene as well.

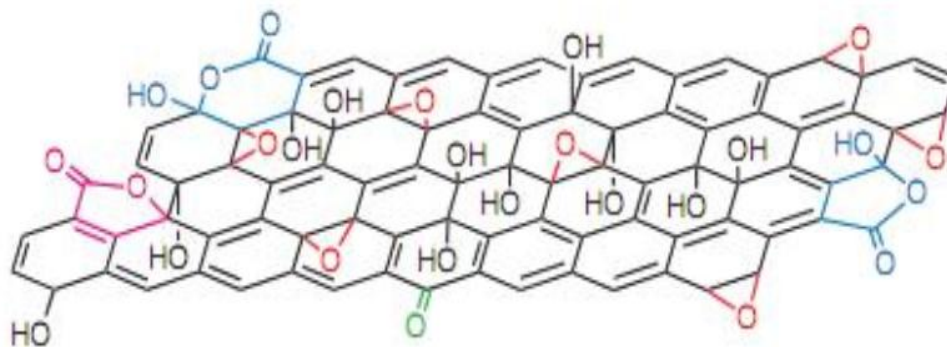


Figure 1.14: Structural model of graphene oxide (Wu et al. 2014)

1.3.2 Carbon nanomaterials as reinforcements in composites

Due to exceptional properties of carbon based nanomaterials like carbon nanotubes, graphene, graphene oxide etc., they have been used to form composite materials in order to utilize their excellent mechanical, thermal and electrical properties. They are being used to reinforce polymers, plastics, metals and ceramics for various applications. For example graphene polymer composites are being prepared to make polymers conductive and strong (Mukhopadhyay & Rakesh 2013; Mittal 2012; Stankovich et al. 2006). But polymer based composites cannot be used at higher temperature applications. So in this case composites of graphene with ceramic or metallic matrices are produced. Graphene composites have been produced along with a lot of ceramics e.g. Al_2O_3 (Fan et al. 2010; K. Wang et al. 2011; He et al. 2009), SnO_2 (Zhang et al. 2010; X. Wang et al. 2011; Wang et al. 2010), MnO_2 (Qian et al. 2011; Yan et al. 2010), SiO_2 . (Watcharotone et al. 2007) and TiO_2 (Williams et al. 2008; Tang et al. 2010). The major applications for which these graphene-ceramic composites were prepared include solar cells (Tang et al. 2010), lithium ion batteries (Zhang et al. 2010; Yang et al. 2010; Qian et al. 2011; Li et al. 2009; Fukui et al. 2010), super capacitors (Yan et al. 2010) and in emitters and electronic devices (Zheng et al. 2009).

The metal composites of graphene has been produced with many metals like platinum (Xu et al. 2008; Li et al. 2009; Si & Samulski 2008), palladium (Xu et al. 2008), cobalt (Yang et al. 2010), silicon (Chou et al. 2010) and gold (Xu et al. 2008; Hu et al. 2010) for their intended use in applications like supercapacitors (Si & Samulski 2008),

biosensors (Zhou et al. 2010; Song et al. 2010), lithium ion batteries (Chou et al. 2010), electrocatalysts (Hu et al. 2010; Li et al. 2009; Fukui et al. 2010) etc.

Graphene reinforced metal matrix composites can be produced by the techniques including reduction of graphene oxide (GO) to graphene after chemical mixing with metals, chemical mixing of graphene with metals or mechanical mixing with metals. Electrodeposition technique can also be utilized to manufacture these types of composites by co-deposition of the nano phase along with the metallic ions. In the present thesis work, the same technique i.e. electrodeposition is used for the production of the nickel matrix graphene nanoplatelets and graphene oxide composites.

1.4 Electrodeposition of carbon nanomaterials-metal matrix composites

Electrodeposition is nowadays a well-known and low cost technique for the preparation of metallic coatings on a conductive substrate (Dini 1993). Many metals can be deposited by this technique, with controlled thickness and properties (Gómez et al. 1995). Recently, composite coatings started to gain interest, due to the possibility to tailor the behavior of the deposited film by controlling the composition, thus becoming an interesting alternative to standard deposition methods, like PVD (Rosso et al. 2008). In particular nickel coatings are industrially modified with silicon carbide or other ceramics (Gyftou et al. 2008; Srivastava et al. 2007; Robin et al. 2009; Garcia et al. 2003; Sun & Li 2007), for improving hardness, or fluoropolymers (Ivanov et al. 2009; TETERINA & KHALDEEV 1998), for reducing attrition and wear, without modifying mechanical properties of core material like it happens when using traditional or novel MMCs (Chawla & Chawla 2013; Manfredi et al. 2009; Manfredi et al. 2010). Since the discovery of carbon nanotubes (Iijima 1991), carbon nanostructures are gaining significant interest in the field of materials science, as they present very interesting properties, both mechanical and thermal (Meyyappan 2004; Shima 2011; Balandin 2011; Shokrieh & Rafiee 2010; Pavese et al. 2010; Castellino et al. 2010). In recent papers, carbon nanotubes or similar carbon nanomaterials have also been used to modify the properties of electrodeposited nickel coatings (Arai 2004; An et al. 2008; Khabazian & Sanjabi 2011; Arai & Endo 2005; Guo et al. 2008; Wang et al. 2005). The composite coating seem to have increased properties with respect to un-modified nickel coatings (Guo et al. 2008; Thess et al. 1996; Jeon et al. 2008), and they present interesting hardness (Khabazian & Sanjabi 2011; Carpenter, Shipway, Zhu, et al. 2011)

and wear properties (Carpenter, Shipway & Zhu 2011). In particular, both Carpenter and co-workers (Carpenter, Shipway, Zhu, et al. 2011) and Khabazian and Sanjabi (Khabazian & Sanjabi 2011) demonstrated an increase in hardness with the increase of nanotubes. In both cases however the increase in hardness was possible only with pre-treated nanotubes, while untreated nanotubes hardness was not so different than the pure nickel coating. Functionalization was in both cases obtained by oxidation, in order to increase polarity of the nanotubes so that they could disperse easily in water. Regarding wear properties, Carpenter and co-workers (Carpenter, Shipway & Zhu 2011) observed a significant reduction of wear rate for carbon-containing composites.

Recently, graphene has also gained much interest as a strong reinforcing carbon nanomaterial (Choi et al. 2010; Young et al. 2012). However, the production of graphene nanoplatelets or graphene oxide electroplated coatings by electrodeposition has not been widely studied yet. Furthermore the previous studies have exploited the thermal and electrical properties of the graphene based metal matrix composites but this study aims to explore the mechanical, wear and friction characteristics of graphene nanoplatelets and graphene oxide reinforced nickel matrix composites.

After preliminary deposition two types of nickel thick composite coatings were produced i.e. Ni/GNP and Ni/GO composites. Nickel thick coatings containing both graphite nanoplatelets (GNPs) and oxidized graphite nanoplatelets or graphene nanoplatelets are very similar to graphene since they consist of a very limited number of graphene sheets, oxidized on the surface to make them partially compatible with water-based deposition solutions. The produced thick coatings were studied in terms of the size of nickel crystallites, hardness, wear and frictional properties.

Chapter 2 Technology of Electrodeposition

2.1 Introduction

The phenomenon, through which a metallic coating forms over base materials by electrochemical reduction of metallic ions in an electrolyte, is called electrodeposition. The technology based on electrodeposition is known as electroplating. This technology is vastly being used today not only for this purpose but also for the extraction of metals from ores or impure materials and in reshaping molds according to the required dimensions where the former is called electrometallurgy and the latter is known as electroforming processes. The phenomenon can also be called electrocrystallization because in most of the cases the metal, which is deposited through this technique, is crystalline in nature. This term was introduced by Russian scientist V. Kistiakovski in twentieth century (D. Gamburg & Zangari 2011).

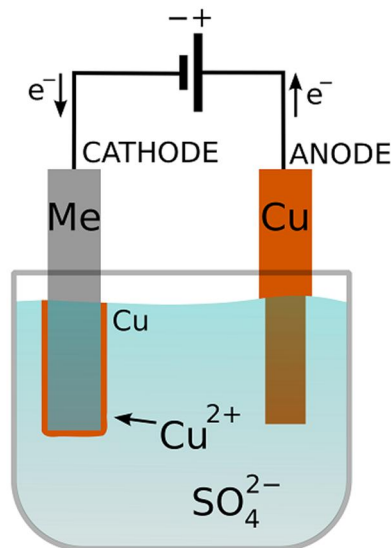
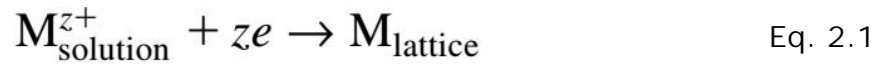


Figure 2.1: Schematic diagram of electrodeposition process being carried out for Cu.

The process involves the reduction or neutralization of ions from different electrolytes by the passage of electricity through their solution in water or in the fused form. Metal ions are reduced from higher oxidation state to lower as given below:



The schematic of electrodeposition process is shown in Figure 2.1. The process can exist in two different forms: in one case the z electrons are provided by the power supply which is usually in the DC form to avoid the polarity disturbances. The other case is the electroless process where no external source of current is required. These two types of processes of electrodeposition are called the electrochemical deposition in overall scenario (PAUNOVIC & MORDECHAY 2006).

The process of electrodeposition is very important in the perspective of production in the sense that it involves a variety of techniques through which one can produce different layers of coatings in a versatile manner which otherwise would be impossible to create and form. But still it should be kept in mind that this is not a simple process to accomplish as there are various variables that control the thickness, purity, and uniformity of the layer. In science and engineering this process is one of the most complex processes to cope with.

Rudzki proposed and an excellent model that explains the metal distribution and the interrelation of the plating variables. A simplified version of this model is shown in Table 2.1. Whereas the Table 2.2 shows the factors influencing the properties of the deposits. Basically electrodeposition is a surface phenomenon in which solid state processes occur in the form of liquid (Dini 1993).

Table 2.1 Metal distribution relationships in electrodeposition (Dini 1993)

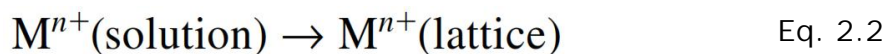
| System Components | Factor influencing metal distribution | Electrodeposit |
|----------------------|--|--------------------|
| Tank | Geometric Electrochemical Incidental | Metal distribution |
| Electrodes | | Composition |
| Solution composition | | Structure |
| Process conditions | | properties |
| Current | | |

Table 2.2 Interdisciplinary nature of electrodeposition (Dini 1993)

| Discipline | Involvement |
|----------------------------------|---|
| Electrochemistry | Electrode processes |
| Electrochemical engineering | Transport phenomena |
| Surface science | Analytical tools |
| Solid state physics | Use of quantum mechanical solid state concepts to study electrode processes |
| Metallurgy and materials science | Properties of deposits |
| Electronics | Modern instrumentation |

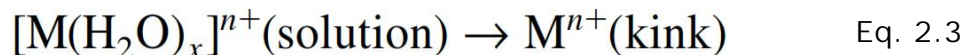
2.2 Formation mechanism of deposited layers

In the process of metal electrodeposition, a metal ion M^{n+} present in the aqueous solution is deposited on the conducting metallic substrate and becomes a part of the ionic metal lattice. A simple representation of the process at atomic scale can be written as:



The above reaction also involves transfer of n number of electrons to the cathodic substrate from an external power source or power supply. These electrons are taken up by the metallic ions present in the solutions as a result of which they get reduced or deposited on the substrate.

As the ions in the electrodepositing solution are present in the form of hydrated ions $[M(\text{H}_2\text{O})_x]^{n+}$, hence the Equation 2.2 can also be written as:



The ions being deposited at the "kink" site are in the form of ad-ion or ad-atom M and the final result of overall process represented by the Equation 2.3 is the absorption of M^{n+} ad-ions/ad-atoms at kink sites. A schematic representation of the initial and final states of ions during deposition process is also shown in the Figure 2.2.

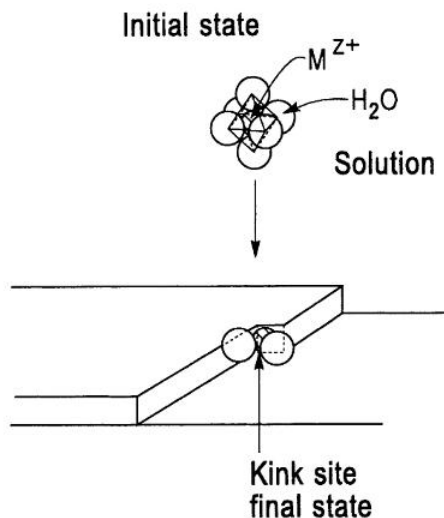


Figure 2.2: States of depositing metallic ions during metal deposition process.

In real world, no surface is perfectly flat and there is always some degree of roughness present on it. In the case of rough surfaces, the electrodeposition processes proceed through two types of mechanisms:

- Ion transfer through step-edge site mechanism and,
- Mechanism of terrace site ion-transfer

2.2.1 Step-edge ion-transfer mechanism

Figure 2.3 illustrates the process of step edge ion transfer which is also known as direct transfer mechanism. In this mechanism, the ions from the solution are deposited over different step edge kink sites. As a result of this transfer the M ad-ion (adsorbed ion) is deposited to the crystal lattice. There are different stages of this process. In the first stage there is the transfer of the M ad-ion to the kink site with one half of energy with respect to the one relative to a bond in the bulk. But it must be remembered that in this position, it still has some water of hydration attached to the ions. Whereas in the other stage there is a direct transfer to the site other than kink. Here the metal ions find a way to diffuse until they reach a kink as shown in Figure 2.3. So it can be assumed that in step-edge site ions-transfer there can be found two ways. First one the direct diffusion of the ions to the kink or site edge path or the diffusion over the surface until to reach the kink or site edge.

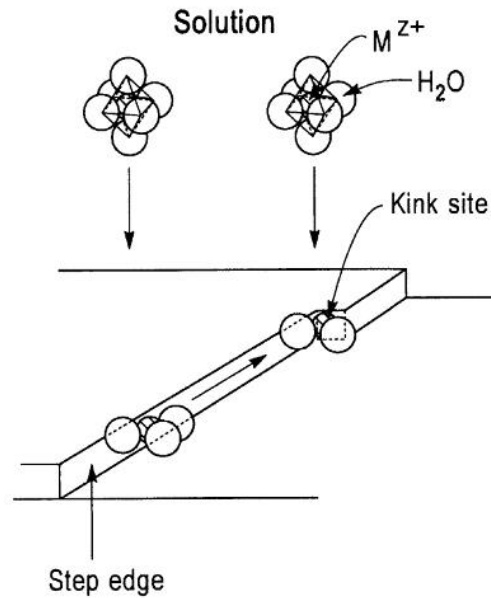


Figure 2.3: Mechanism of step edge ion transfer

2.2.2 Mechanism of terrace ion-transfer

In this process an ion from the solution is transferred to the flat surface or terrace region of the substrate as shown in the Figure 2.4.

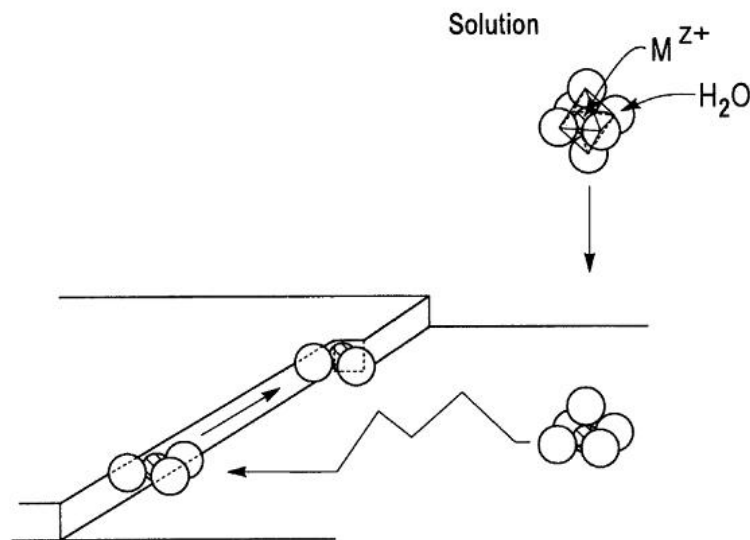


Figure 2.4: Ion transfer mechanism to the terrace and surface sites and deposition at kink site.

The ions in this state are the adsorbed-ion (adion) state having most of the water of hydration. The ions are not strongly bound to the crystal lattice at this stage. They try to seek out the position of lowest energy, hence they are still mobilized due to having relatively higher energy as compared to the atoms of substrate. Again for these ions the final position is a kink site. If we consider the two mechanisms step edge and terrace ion transfer, the current i can be composed of two parts,

$$i = i_{se} + i_{te} \quad \text{Eq. 2.4}$$

In the above Equation 2.4, i_{se} is the step edge and i_{te} is the terrace site current component (Paunovic & Mordechay 2006).

2.2.3 Mechanisms of growth

To make a coherent deposit there could be possibly two basic methods and mechanisms:

- Layer growth mechanism and
- Crystallite growth mechanism

These mechanisms can be well understood by a schematic sketch given in the Figure 2.5.

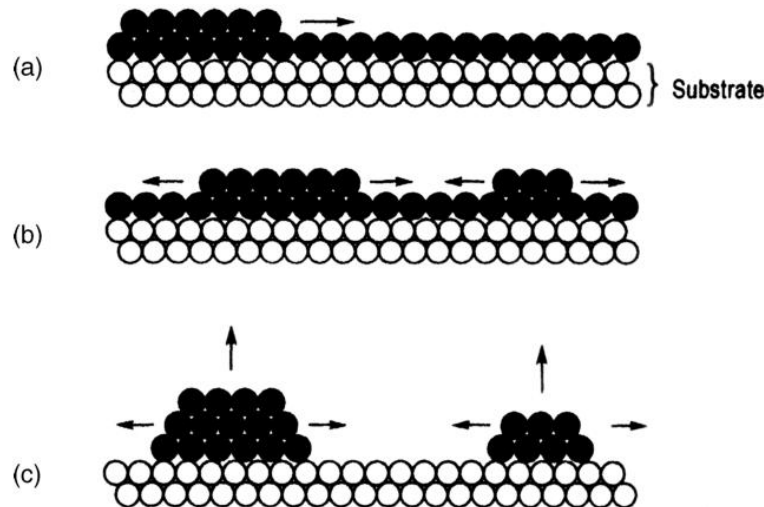


Figure 2.5: Representation of the layer growth mechanism (a, b) and crystallite growth or nucleation coalescence mechanism (c)

In the process of layer growth the crystal is enlarged by the formation of new layers like in onions. This is a step in the growth of a layer which is in coherent with the substrate. These processes are very important and having a big role in electrodeposition of metals

There are different growth steps like monoatomic growth steps, poly atomic growth steps which could be micro and macro in nature (Schlesinger & Paunovic 2010).

In the mechanism of three dimensional crystallites (TDC) formation, the coalescence of crystals occurs. The overall growth takes place in the following steps:

- Nuclei formation and their growth towards TDC
- Joining or merging and coalescence of TDCs
- Linked network formation
- Continuous network formation.

2.2.3.1 Growth as columnar microstructure

As show in Figure 2.6, the columnar structure is always perpendicular to the surface. This structure is composed of fine equiaxed grains near the surface but transform later to columnar grains on the upper surface of the deposit. The columnar grains are much coarser as compared to fine grains near the surface and spans to a greater distance compared to fine grains.

The formation of columnar grain may be considered due to competition between the adjacent grains which ultimately results in the form of long columns. The grains with lower surface energy grow faster always than those with high surface energy i.e. the finer grains. This results in the decrease of higher surface energy grains coalesce and end up in the coarser grains. So the structure becomes like the finer grains are near the substrate surface then coarser grains and then the big columnar grains, as we proceed from substrate towards the coatings (PAUNOVIC & MORDECHAY 2006; Mazor et al. 1988; Sheshadri 1975).

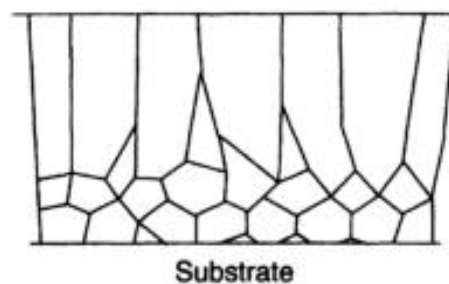


Figure 2.6: A schematic representation of the columnar deposit

2.3 Electrochemical deposition cell and its components

The current is required to flow through for any kind of electrodeposition. A chamber which is used to generate energy from chemical reaction or to initiate a chemical reaction by flow of electricity is known as an electrochemical cell. Commonly used batteries in clocks and toys of 1.5 volts are simple examples of electrochemical cell where some slurries of different materials are used to initiate chemical reactions which generate energy.

The electrochemical cell is an essential component of the electrodeposition process. In principle, an electrodeposition cell is analogous to a galvanic cell but acting in reverse direction. The main components of an electrochemical deposition cell can be listed as:

1. Electrodes
2. External current source
3. Electrodeposition bath (electrolyte)
4. Additives

An electrode is a term in electrochemistry having various meanings and connotations. An electrode is the region where any chemical activity either oxidation or reduction takes places. Depending upon the flow of current either it becomes cathode or anode but sometimes they can serve both reactions or identities being anode and cathode at a time. Secondly the electrode together with solution is called a half cell and can be considered and studied as separately entity performing oxidation or reduction in the cell or electrochemical reaction (D. Gamburg & Zangari 2011).

To flow the stream of electrons from one electrode to another electrode, there is required some medium which should be conductive for the electrons or ions in order to close the circuit and for that reason in electrochemistry electrolytes are being used. These electrolytes could either be solutions in water or fused salts. Power is supplied in the direct form and a potential is created between the electrodes. The ions in the solution are reduced at cathode while oxidation takes places at anode where the anode is dissolved and eroded with time and conditions. These ions which are dissolved into solution create a potential which leads to deposition of same amount ion on cathode in the form of neutralized atoms. So the dissolution rate of anode is always equal to deposition rate of atom over cathode or plating rate on cathode. In some cases the electrodes are not consumable and these atoms for plating are actually only provided by

solution or electrolyte so needs be changed continuously to provide a fresh supply of ion to the system.

Both types of anodes, soluble and non-soluble, are frequently being used in the electrodeposition processes. Usually for electrodeposition of silver, zinc, nickel, copper and many others, the anodes are consumables. Chromium, gold and some other precious metals require non-soluble or insoluble anodes.

For the soluble electrodes there are double duties to play in the process; to provide a path for the flow of current and to provide the necessary ions in the process so need not to replenish the solution continuously. The metallic ions from soluble anodes transfer through solution to the cathode and get again neutralized and create a coating or plating over there. For nickel and copper usually soluble electrodes are used to create plating and also to refine these metals from crudes. The purity of anode is very critical in measuring the rate of dissolution because due to impurities the potential tend to decrease down that reduces the efficiency of anode. But however usually the efficiency remains 100% or close to 100% if the anode is pure. At higher anode potentials sometimes anodic passivation occurs. This results in localized potential decreasing the efficiency of anodic current.

Also on the surface of soluble anodes, oxygen is sometimes evolved. So it is required to check out whether the electrodes are working properly when using soluble electrodes (D. Gamburg & Zangari 2011).

2.4 Parameters of the process and their effect on electrodeposition

As stated in the introduction, electrodeposition is not a simple dip and dunk process. A lot of parameters influence this process that need to be controlled properly for a good quality electrodeposit. Some of the important parameters of electrodeposition process include:

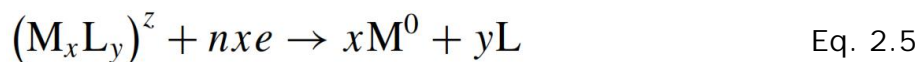
- Deposition time and thickness
- Current density
- Electrode potentials
- Bath composition and conductivity
- Bath additives or surfactants
- Bath temperature

- Substrate surfaces
- Bath pH
- Bath stirring
- Hydrogen and oxygen evolutions on the electrodes
- Current and metal distribution

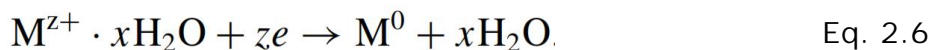
In the next sub-sections, each of these parameters and their effect on the electrodeposition is described briefly.

2.4.1 Deposition time and thickness (Faraday's law)

Generalized reaction of metal deposition is as follow in electrochemical process.



Where L is a molecule, an ion, or radical which is tightly bound to the metal ion M. this makes a *complex* species $(M_xL_y)^z$ and play a role in charge movement process. These intermediate compounds are usually referred as electroactive species. Equation 2.5 indicates the various variables where n is the amount of electrons transferred in depositing atom on the cathode and this quantity is always positive. z can be negative or positive or zero and is the electric charge of electroactive species. The hydrated metal ion discharge becomes a simple ion discharge when n becomes equal to z . This reaction can be written in the following way:



Electrostatic interaction is indicated by dots. But usually $n \neq z$ as n is a different entity and should not be confused with z .

The quantity of deposition of a metal can be calculated if we know the total number of electrons transferred from the external source towards the cathode. From Equation 2.5 we can deduce that ne number of electrons is needed to deposit one atom of a metal. By considering Avogadro's law, we can say that one mole of the metal can be deposited by supplying $N_A ne = nF$ coulombs of electricity. Where N_A is the Avogadro's number ($6.022 \times 10^{23} \text{ mol}^{-1}$) and F is the Faraday's constant ($F = 96485 \text{ C mol}^{-1}$). Now the quantity of a

deposited mass is determined by using the Equation 2.7 which is known as Faraday's Law.

$$m = QA/nF \quad \text{Eq. 2.7}$$

Here m is the mass of deposited metal in grams and Q the charge passed and A is the atomic weight of the metal deposited.

The Equation 2.7 is very important in calculating and measuring the amount of metal deposited in the process of electrolysis. Hence thickness and weight of metal could be easily found. Hence the amount of electricity used in the process of electrodeposition is quite useful to have information about various important aspects including mass and the volume of the deposited metal.

Equation 2.7 gives only the mass of the electrodeposited coating. If one is interested to calculate the thickness of the coating, it can be calculated through the following equation:

$$T = 1000m/\rho S \quad \text{Eq. 2.8}$$

Where: T = thickness in micrometers, ρ = density in grams per cubic centimeter, S = surface area of the plated part in square centimeters. 10000 is a constant for the conversion of centimeters to micrometers.

By combining the equations 2.7 and 2.8, we have the following equation for plated thickness calculation.

$$T = 1000 ItA/nF\rho S \quad \text{Eq. 2.9}$$

The process of electrodeposition occurs at the interface of solution and electrode so this interface greatly influences the structure and properties of electrodeposited coatings.

The mass of the element, expressed in grams, transported from the solution and deposited on the electrode by one coulomb of electricity is called the mass electrochemical equivalent. It is denoted by K_m and expressed in g/C. If the deposited metal is expressed in volume instead of the mass, the electrochemical equivalent is called volume electrochemical equivalent which is denoted by K_v and is expressed in

cm^3/C . Mass and volume electrochemical equivalents (K_m , K_v) of some common metals are given in the Table 2.3 (D. Gamburg & Zangari 2011).

Table 2.3: Volume and mass electrochemical equivalents of some common metals

| Metal | K_v , $\text{cm}^3/\text{A-h}$ | K_m , $\text{g}/\text{A-h}$ |
|----------|----------------------------------|-------------------------------|
| Au (I) | 0.380 | 7.35 |
| Au (III) | 0.127 | 2.45 |
| Ag | 0.3837 | 4.025 |
| Bi | 0.1590 | 1.560 |
| Cd | 0.2424 | 2.097 |
| Co | 0.1234 | 1.099 |
| Cr | 0.0449 | 0.323 |
| Cu(I) | 0.2652 | 2.371 |
| Cu(II) | 0.1326 | 1.186 |
| Fe(II) | 0.1324 | 1.042 |
| Fe(III) | 0.0883 | 0.695 |
| In | 0.1956 | 1.428 |
| Mn | 0.1374 | 1.025 |
| Mo | 0.0670 | 0.597 |
| Ni | 0.1229 | 1.095 |
| Pb | 0.3409 | 3.866 |
| Pt | 0.1696 | 3.640 |
| W | 0.0587 | 1.143 |
| Zn | 0.1711 | 1.220 |

2.4.2 Current density

Current density is very important entity in measuring the rate of electrodeposition of metal. This is measured from the applied current value (obtained from the ammeter reading) divided by the surface area S of the cathode surface immersed in the electrodeposition solution. It can be expressed in A m^{-2} or A dm^{-2} and the deposition rate is expressed in $\text{mol cm}^{-2} \text{s}^{-1}$. The rate of deposition of metal increases with an increase in the current density up to a certain duration of time.

The accurate measurement of the current density is closely related to the precise measurement of surface area S . And the accurate surface area measurement depends on

the roughness of the surfaces. If the surfaces are perfectly smooth then the geometrical surface area S_g is considered equal to the real or true surface area S_t . But if the substrate surfaces are rough, then the true surface area S_t is greater than the geometrical surface area. In this case a roughness coefficient K_r is introduced which is the ratio of true surface area to the geometrical surface area i.e. $K_r = S_t/S_g$. For highly polished surfaces K_r has a value between 2-3. Since $K_r > 1$, then a term real current density i_r is used which is given by $i_r = i_{app}/K_r$. Where, i_{app} is the apparent current density measured by considering the geometrical surface area of the substrates.

Current density is commonly considered as uniform throughout the entire surface of the substrates. But sometimes the heterogeneous surfaces become segregated based on the different energy potentials at different sites and as a result the electrochemical processes occur preferably on high energy sites (also called the active growth sites) first and then on the others. Due to this reason, current density is not uniform during the start of the electrodeposition process but it generally become uniform across the surface as the deposition proceeds (D. Gamburg & Zangari 2011).

2.4.3 Electrode potential

The potential difference between the electrolyte solution and the electrode bulk material is called the electrode potential. It can be represented by the symbol ϕ . Current density and the electrode potential both are the physical variables that are very important in controlling the electrochemical processes occurring on the electrodes. But there is one problem that this potential difference cannot be measured directly because there is no fixed value of potential assigned to the electrolytic solution. To overcome this problem reference electrodes having a constant and stable potential are used. Different types of standard electrodes exist for the measurement of this kind of potential for example SHE (Standard Hydrogen Electrode). The potential of SHE can be denoted by the symbol E and it is normally taken as zero at any temperature. The practical measurement of SHE is also little complicated so usually in the labs other kinds of reference electrodes are used as an alternative for instance calomel or silver/silver chloride electrode. The reference potentials for various types of standard electrodes are given the

Table 2.4 (D. Gamburg & Zangari 2011).

Table 2.4: Types and potentials of different Reference Electrodes

| Electrode | Symbol | Potential at 298 K (mV) | Temperature Coef. (mV/K) |
|-----------------|---|-------------------------|--------------------------|
| 1 M calomel | Pt Hg Hg ₂ Cl ₂ 1 M KCl | +283 | -0.24 |
| Satur. calomel | Pt Hg Hg ₂ Hg ₂ Cl ₂ satur.KCl | +244 | -0.65 |
| Silver chloride | Ag AgCl HCl | +222 | -0.65 |
| Mercury sulfate | Pt Hg Hg ₂ SO ₄ a(SO ₄ ²⁻)=1 | +615 | -0.82 |
| Cadmium oxide | Cd CdO, a(OH)=1 | +13 | |

During the electrodeposition process, current density or the potential values can change a little as the deposition proceeds. These changes occur due to the surface roughness and morphological characteristics of the electrodes, change in composition and pH of the electrolytic solution with the passage of time. There are two conditions possible:

- if the potential is fixed (i.e $E=\text{constant}$) and current density i changes with the time, this condition is called potentiostatic process,
- if the current does not change (i.e $i=\text{constant}$) but the potential E varies with the time, this condition is called galvanostatic process.

2.4.3.1 Equilibrium potential and overpotential

The potential of the electrode at which current density I is zero and the electrode process is in thermodynamic equilibrium, is called the equilibrium potential of the process. It can be denoted by E_{eq} and can be described and calculated from the well known Nernst equation:

$$E_{eq} = E_0 + (RT/nF) \ln (a_{Mz+}) = E_0 + (1/nf) \ln (a_{Mz+}) \quad \text{Eq. 2.10}$$

Where;

$$f = F/RT = 11604/T \text{ (V}^{-1}\text{)};$$

$R = 8.3145 \text{ J/mol K}$ (gas constant) and,

$T =$ the absolute temperature

$E^0 =$ standard potential for this process observed under standard conditions ($T=298 \text{ K}$, and $1 \text{ atmospheric pressure}$).

For depositing a metal with a specific rate, it is necessary to shift the electrode potential from equilibrium to the negative (cathodic) direction. The shift of the potential value towards negative direction causes an increase in the reduction process of the metals to be deposited on the electrode. Whereas if the potential is shifted towards the positive direction, the anodic or oxidation process will be enhanced. This change or shift in the value of the equilibrium potential of the electrode towards positive or negative direction is termed as the overpotential and it is represented by η :

$$\eta = E - E_{eq} \quad \text{Eq. 2.11}$$

The overpotential is an important quantity that can be employed to have information about the rate of the deposition process as well as the structure and properties of the depositing metal. Higher the values of overpotential, finer and denser are the deposits. In electrodeposition processes, the values of overpotential can be in the range of few mV to 2V.

The relationship and dependence of current density i and the potential E is shown in the Figure 2.7. η_a and η_c are the anodic and cathodic potentials respectively. These particular type of curves are called voltammograms or polarization curves (D. Gamburg & Zangari 2011).

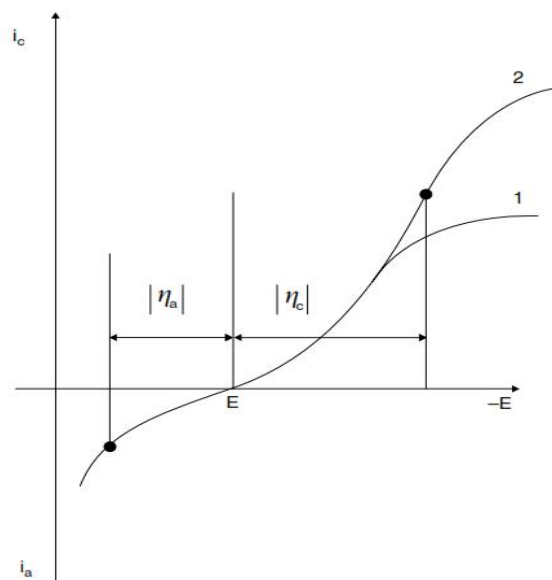


Figure 2.7: A voltammogram for the electrochemical deposition process 1) without electrolyte stirring and, 2) with stirring.

2.4.4 Composition and conductivity of deposition baths

The metals can be deposited from their respective aqueous solutions or the molten salts. Actually, these metallic salts are dissociated into positively charged cations and negatively charged anions in the solution. When an external current is applied, these charged particles move towards the cathodes of the opposite polarity and get deposited on it. For examples the copper sulphate acidic solutions employed for Cu deposition contain salt's constituents dissociated in Cu^{2+} cations and SO_4^{2-} anions. The Cu^{2+} cations, on passage of electricity, are converted to purer plated copper on cathode and the anode is dissolved into the salt. Similarly, acetic acid solutions used for the deposition of Ni contain $\text{Ni}(\text{CH}_3\text{COO})^+$ ions which deposit Ni to the cathode.

For electrodeposition, both one component and multicomponent solutions can be employed but one component solutions have problems of poor quality deposits. That's why one component solutions are not commonly used. Some additional elements, known as supporting electrolytes, are added to the electrolytic solutions according to the requirement of the specific purpose to achieve. But these supporting electrolytes are not involved in the electrode processes and are only present in the solution to improve the quality of deposition.

In addition to the bath composition, electrical conductivity of the deposition baths must be controlled and monitored as it also plays an important role in the process of deposition. Also this conductivity can be used to determine the deposition voltage and the degree of uniform distribution of the metals. The electrolyte conductivity is highly dependent on their composition and can be directly related with the concentration of ions and their ability to freely move in the solution. Less the concentration and mobility of the conducting ions, less is the electrical conductivity of that solution. Electrical conductivity of the depositing solution is given by the following equation as:

$$\kappa = \kappa_1 + \kappa_2 + \dots + \kappa_n \quad \text{Eq. 2.12}$$

Where κ_i represents the conductivities of the ions with respect to their percentage quantities present in the solution. But, the sum of conductivities of the individual concentrations is not equal to the overall conductivity of the solution. This is because of the mutual interactions of all different types of ions present in the solution and also due

to their interaction with the water molecules. Hence for the commercial processes, the actual conductivity of the solutions should be measured instead of calculated from its components' conductivities.

The electric conductivity is always desired to be the higher possible, without compromising the quality of the deposits, because the higher conductivity results in lower energy loss in the form heat and agitations and also the required thicknesses are obtained in shorter times. The conductivity is usually increased by adding alkalis or acids in the deposition bath. Gas bubbles and the small non-conducting particles present in the electrolytes also affect their conductivities.

2.4.5 Bath additives

Various additives are commonly used in the electrodeposition process. The primary effect of these additives is to decrease the surface tension and to facilitate the mobility of ions. The surface tension is detrimental as it keeps the hydrogen bubbles intact to the different areas of the cathode and prohibits these areas to be plated. Hence non uniformities are created over the surface of the plated region called pitting. There are different additives being used today for the process of electrodeposition which are very specific in nature to some specific kind of element. One specific class of additives may not be useful for the other materials and may be in some cases even detrimental.

Additives not only facilitate but also effect on the final surface finish and initial adherence of the plating materials to the surface of the coated substrate. These materials are called 'brighteners' due to the ability to form very fine surface finish which do not require further treatment. Other agents are called 'levelers' which actually smooth the final surface of the plated deposits. Beside these, there are some additives which are used to suppress dendrites, enhance current efficiency, anode activation for dissolution etc. Also the additives reduce or inhibit the deposition by increasing the over potential (η) values. This effect is shown Figure 2.8.

The concentrations of additives are usually kept between 10^{-4} and 10^{-2} moles per liter. But in some cases even very low concentrations are enough for the process to proceed (D. Gamburg & Zangari 2011).

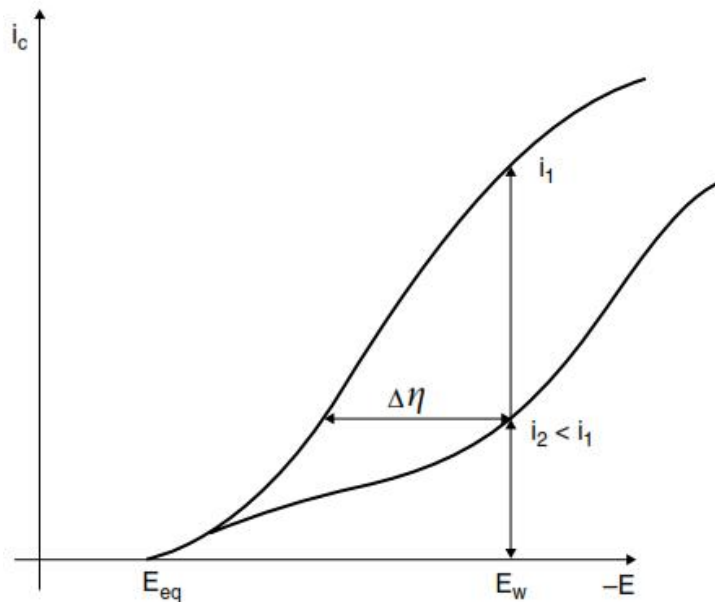


Figure 2.8: General current-potential characteristics: 1 without inhibition, 2 with inhibition. i_2/i_1 is the inhibition extent, $\Delta\eta$ is the additional overpotential at $i = \text{const}$.

2.4.6 Temperature of the bath

The temperature of the electrolytes is another important characteristic that has noticeable effect on the electrodeposition. Actually the temperature affects the electrical conductivity of the solutions by changing the mobility of the ions and as a result it affects the deposition rates and thickness as well as the deposition quality. Normally a 1 °C increase in the temperature of the electrolyte increases its conductivity up to 2%. Usually the operating temperature is between 15 and 70 °C. But sometimes, temperature may approach 99 °C. Higher temperature provide various advantages over lower temperatures like decreased anodic passivation, enhanced solubility of additives and electrolyte, improved electric conductivity.

On the other hand, there are some disadvantages which may include the evaporation of the electrolyte, corrosion of newly formed surface of the plating, etc.. Additives' evaporation also promotes the formation of coarse grains of the deposited metal. But the lower temperatures also come up with some disadvantages like higher electrolytic resistance to the flow of electricity hence higher energy loss, non-uniform layer thickness and composition of the metal deposited. The precise control of the temperature is

required especially at lab scale but, at industrial scale a variation up to a few degrees (± 3 °C) are acceptable. The temperature is also important in rate control of the process as only 1 °C rise results in 10% increase in the rate of process that can result an enhancement in the mass transfer rate up to 2% (D. Gamburg & Zangari 2011).

2.4.7 Substrate surface

The surface finish and cleanliness is also very important to consider in the electrodeposition as it strongly influences the adherence of the plating material to the substrate. If the surface is contaminated, the coating is not uniform because in some areas the current density is higher and in some areas it is lower. But if the substrates is well cleaned and free of oxides and has almost the same crystal structure at the surface as that of the deposited material, even then the influence of substrate may propagate up to 10 μm of thickness. If the surface is smooth and is well polished mechanically, it has small effect on the coating growth and the developing coating is almost uniform and smooth (D. Gamburg & Zangari 2011).

2.4.8 pH of the bath

The pH of the electrolyte is quite important in the perspective of evolution of hydrogen gas and hydroxide activities over the electrodes in the cells. The pH indicates the overall activities of the electrolytic species and is important to control for establishing a well-balanced equilibria.

Different solutions and compounds are used to control the pH of the bath which includes acids, alkalis etc. The pH must be stable to get uniform results for the plating throughout the process. There are various standard tables available to control the pH of different materials during electrolytic process. Different buffers can also be used to maintain the pH constant at various desired levels (D. Gamburg & Zangari 2011).

2.4.9 Stirring of the bath

The agitation of the deposition bath has its effect in increasing the metallic ions transportation towards the substrate but it has no significant effect on the properties of the final deposit. It also limits the thickness of the diffusion layer.

The electrodeposition bath can be stirred by utilizing various available techniques including:

- Mechanical magnetic stirring
- Stirring by compressed air
- Stirring by ultrasounds (using probe sonicators or bath sonicators)

2.4.10 Hydrogen evolution and embrittlement

During the process of electrodeposition, hydrogen gas is evolved usually along with the electrodes due to hydrolysis of water and acids. This evolution brings up with various problems to the metal deposited and to the electrodes. It causes not only the loss of energy but also loss of some mechanical properties of the deposit. Tafel equation (Eq. 2.13) is used to estimate the rate of hydrogen evolution on the electrode:

$$E = a + b \ln i \quad \text{Eq. 2.13}$$

Here E is the electrode potential, a and b are constants which can be found in tables in literature or standard books and i represents the rate of hydrogen evolution.

b is known as Tafel slope which is almost 0.12 V per decade for metals mostly while values of a may be different depending on different situations. The Equation 2.13 can be effectively used to calculate the rate of hydrogen evolution for almost all electrolytic cells. Initially the evolution is higher for the low Tafel coefficients a and mostly observed in Zn/Fe couples. This evolution of hydrogen on the surface is harmful for the quality of deposit being developed on the cathode as H_2 evolution causes porosity in the coatings and also cause embrittlement (D. Gamburg & Zangari 2011).

2.4.11 Current and metal distribution

The distribution of current on the substrate surface is also important during the electrochemical deposition process. It should be controlled and uniform during the whole process as the non-uniformity results in segregated regions of current density. Due to this segregation effect, some regions have more thickness of the coating whereas the other may have less thickness resulting an overall non uniform coating of the metal.

The current distribution can be categorized in microdistribution and macrodistribution. Both type of type of distributions may occur at same time but with different values. Microdistribution is caused by the microscopic surface roughness of the electrode surface

while macrodistribution represents the overall current distribution on the whole electrode. Both effects can be explained by the sketches as shown in Figure 2.9 (microdistribution) and Figure 2.10 (macrodistribution).

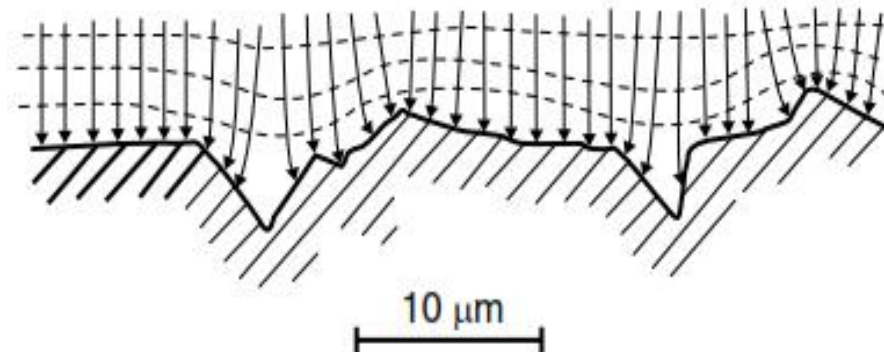


Figure 2.9: Cross section of a rough surface and corresponding current distribution in the adjacent solution (microdistribution)

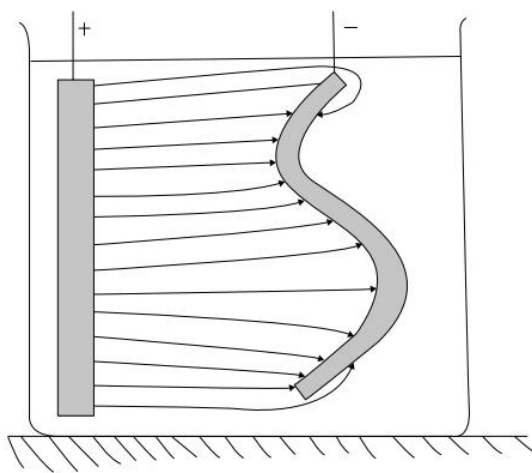


Figure 2.10: Current distribution on the overall electrode surface (macrodistribution)

The two types of current distributions (CD) i.e. microdistribution and macrodistribution can widely differ at the same time and even in the same regions. As an example, in a certain electrode area, macroscopic distribution of current may be same, while the microscopic distribution may be different at the same place due to the presence of micro scale ridges and valleys. Usually current distribution is higher on the ridges and as a

result it causes a preferential and faster growth of the coating in that area as compared to the others (D. Gamburg & Zangari 2011).

2.5 Structure and properties of electrodeposits

The properties and structure of the electrodeposited layer depend on the composition, properties and structure of the deposition bath. In addition, the quality of deposit also depends upon the current density, electrode potentials, pH, temperature of the bath as well which are discussed in the previous section (D. Gamburg & Zangari 2011).

As in the case of other materials, the structure of electrodeposited metals consists of grains. The size and shape of the grains determine and characterize the structure of the deposit. There are four possible structures that are described below:

1. Columnar grains structure: these structures are developed under conditions of low current density depositions. These are ductile and possess low hardness and low strength.

2. Fine grains structure. If the size of the grains in the range of 10-100 nm, the structure is said to be fine grained structure. They are obtained when the deposition is done on high current density values. The fine grained deposits are characterized as brittle and hard structures. Although in some cases rather ductile structures are also possible to be obtained

3. Fibrous Structure: These types of structures have intermediate nature and properties between fine grained and columnar grained structures.

4. Banded Structure: If the grain size is extremely small, less than 10 nm, they give a banded type structure. They have very poor ductility but very good hardness and strength.

Some authors propose another classification of the electrodeposited structures. The columnar and fibrous grain structure is common in both classifications.

1. *Columnar Grain Structure*. This kind of grain structure is developed due to the preferred growth of the electrodeposits in some directions and it is obtained in compact and dense thin films. Some randomly oriented grains are also obtained but their number is less than the others.

2. *Equiaxed Grain Structure*: Equiaxed grains are grown in comparatively bigger size than the columnar grains.

3. *Dendritic Structure*. This type of structure is developed as a result of mass transport-controlled growth. All the grown crystals are not of same size and they vary in their shape as well.

4. *Nodular Grain Structure*. Their name is because of nodular type of appearance. These structures are also often termed as “cauliflower type.”

5. *Fibrous*. These types of structures also develop due to the oriented growth of grains that do not grow uniformly on the whole surface of the substrate.

A schematic summary presentation of four of these grain types is given in Figure 2.11.

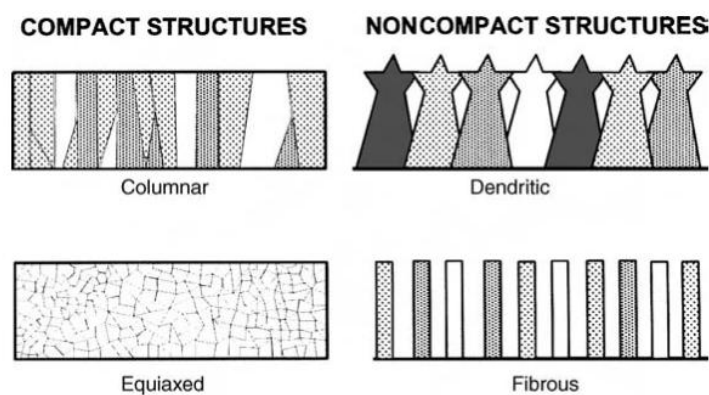


Figure 2.11: Different types of grain structures exhibited by electrodeposited materials

The variables of the electroplating process i.e. metal-ion concentration, additives, temperature, agitation, and polarization have profound effects on the grain structure of electrodeposits. A schematic representation is shown in Figure 2.12. (PAUNOVIC & MORDECHAY 2006)

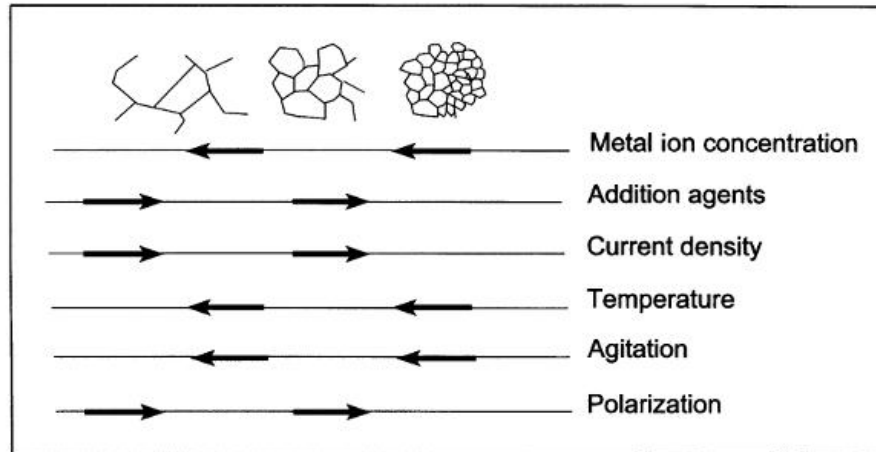


Figure 2.12: Effect of operating conditions on the microstructure of electrodeposits

2.6 Electrodeposition of alloys

Alloys are materials which are made to enhance the various desired properties of the metals which otherwise are sometimes impossible to exhibit by pure metals. These properties include strength, ductility, corrosion resistance, modulus of elasticity, wear resistance, solderability, hardness etc. In the same way higher magnetic susceptibility can also be obtained by the alloying methods. And in some situations the purpose of the coating is the same i.e. to enhance the properties of the materials in a similar way as is done by the pure metal depositions.

Alloy deposits can be made through electrodeposition by changing the composition of the electrolyte of the cells. The desired metal solutions are added according to required alloy composition depending upon their oxidation and reduction potentials. The incorporation of the codeposit metal is made by acquiring its concentration which is determined by Faraday's Law and this is directly proportional to the current density.

This alloying is difficult in case of coatings but not impossible. Different salts of electrolytes are used to obtain a situation where different ions of the required metals are produced and codeposited during the electrodeposition process. Some alloys are easy to deposit like Ag–Ni alloys and Ag–Co alloys. There are also some metals e.g. V, W, Nb, Zr, Ti etc. that cannot be deposited from their aqueous solutions. Thus they are deposited from their molten salts (Djoki 2014).

According to the definition, the electrodeposition of alloys is a codeposition process where two or more different metals are deposited at same time to obtain an alloyed layer of the coating. For this to accomplish, the ions of the desired alloy constituents should be present at the same time to make a coating over the cathode. The deposition potential should be equal or somewhat near to each other of all the constituent metals.

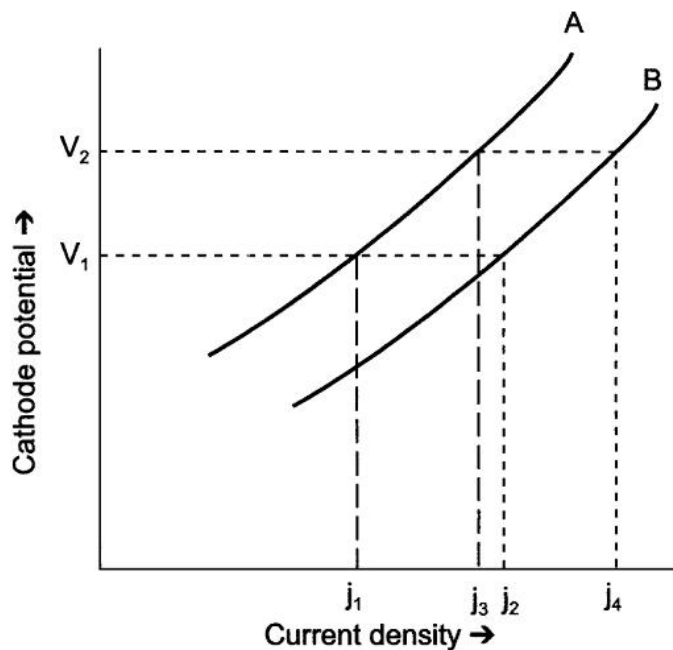


Figure 2.13: Polarization curves for the deposition of alloys

Figure 2.13 shows the typical polarization curves (deposition potentials) for the alloy deposition of two metals (A and B) as a function of current density of the both metals. From these curves, it is deduced that if the potentials of the metals A and B are V_1 and V_2 respectively, it is possible to deposit metals with ratio j_3/j_4 (Paunovic & Mordechay 2006).

2.7 Electrodeposition of composites

Initially it was considered that if there are some insoluble entities in the electrolyte solution and they get deposit in the coating along with the main coating element, they cause adverse effects on the properties of the final coatings. Due to this reason, great care has been taken to avoid the incorporation of unnecessary particles for example anode debris or anode mud, dust from air, impurities for the depositing solution etc. But later it was realized that there could be some benefits of incorporation of these particles

and substances if they are intentionally added and if properties and the effects of these entities in the depositing coating are well understood. By this idea, it became possible to deposit composite materials using electro or electroless deposition techniques with the same purpose i.e. to get the superior properties of the composite than the individual elements. Only the composites based on the metals (i.e. metal matrix composites) can be prepared by this technique, which are able to be electrodeposited.

In the process of composite electroplating, the particles deliberately added to the deposition bath should be inert so that they don't react with and don't dissolve in the electrolytes. For example, silicon carbide (SiC) particles are added in the nickel-phosphorus deposition bath. Silicon carbide particles are co-deposited along with the nickel-phosphorus on the cathode when an external power supply is applied. A micrograph of SiC/Ni-P composite is shown in the Figure 2.14. By using electrodeposition technique, second phase particles of many types e.g. metallic particles, plastics and ceramic particles etc. can be codeposited to obtain various types of metal matrix composites. These composites have higher properties as compared to purer depositing metals in many ways like in strength hardness, wear and corrosion resistance properties etc. (Hovestad & Janssen 2005)

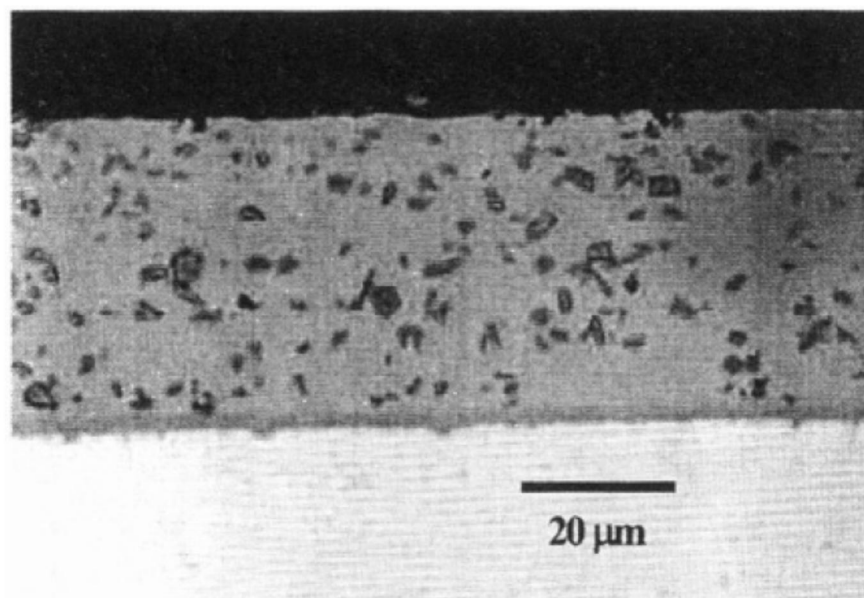


Figure 2.14: Cross-section of SiC particles and nickel-phosphorous composite coating on aluminum substrate

Another example of the composite electrodeposition is the deposition of Zn/GO composites. A schematic representation of the electrodeposition process for the composite deposition is shown in the Figure 2.15.

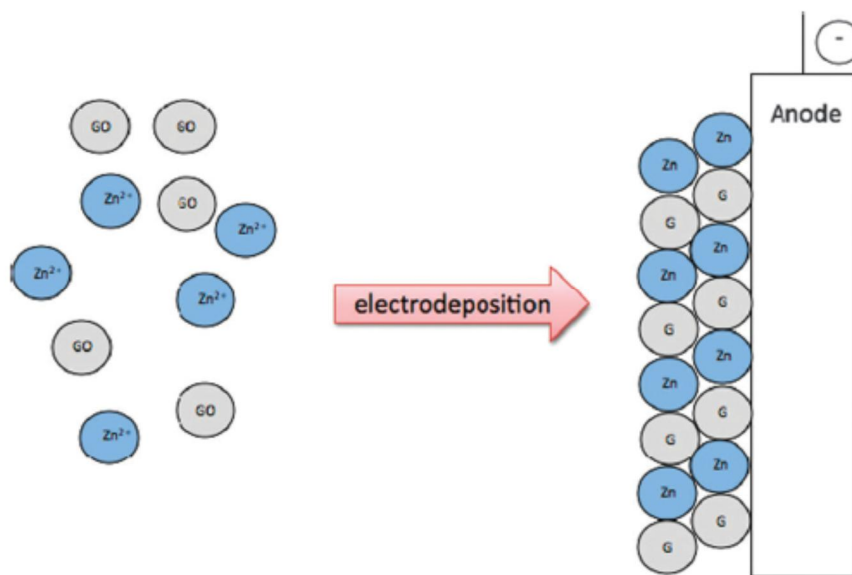


Figure 2.15: Schematic representation of electrochemical codeposition of Zn/Graphene oxide composites. (Hilder et al. 2012)

Although composites can easily be deposited by electrodeposition technique, an important consideration needing attention during this process is the uniform dispersion of the second phase particles in the deposition bath. Stable dispersions can be achieved by adding some additives or surfactants that aid the uniform distribution of the particles in the bath. In addition, certain dispersing techniques e.g. mechanical stirring or ultrasonication is also done to further stabilize the suspensions and even the dispersion can be continued during process of deposition so that the suspended particles remain well dispersed and in the bath as long as the deposition process proceeds.

2.8 Applications

In the past electrodeposition was intended to deposit a thick layer of polycrystalline metals over the cathode substrates. These layers were produced to protect or act as sacrificing elements during corrosion process for the main metal. Sometimes the layers

used to be deposited for decorative purposes, and sometimes even to enhance mechanical properties as well. However, with the development of the electrodeposition techniques and with the possibility of complex control over current density, electrolytic composition has made it possible to control the thickness and quality to such a level that we can produce electrodeposits having very high and advanced properties. So these days electrodeposition process is widely being used in depositing the magnetic thin film heads, in semiconductor and microelectronics technologies. Also these deposition processes are being extensively used in medical industry where different tools are coated according to required surface finish and according to required antibacterial properties. And in recent research, it is revealed that electrodeposition is also viable in nano-sciences and nano-technologies (Paunovic & Mordechay 2006).

For example in semiconductor industry, the copper interconnects on the chips are deposited by the electrodeposition technique replacing the previous technology of vacuum-based deposition techniques used for depositing aluminum or aluminum alloy (Al+Cu) conductors on the chips. In fact, there are various steps involved in the preparation of Cu-interconnects on chips which are shown in the Figure 2.16.

The first step is the deposition of dielectric on the smooth substrate of a silicon wafer. Then in the second step, it is patterned using photolithography and a dielectric-RIE (reactive ion etching) process. Then a Cu seed layer is deposited using PVD and CVD processes. Then Cu is electrodeposited into the holes, trenches and recesses. The excess Cu is removed by chemical and mechanical polishing (CMP) technique. And as the final step Cu line is patterned and deposited (SCHLESINGER & PAUNOVIC 2010).

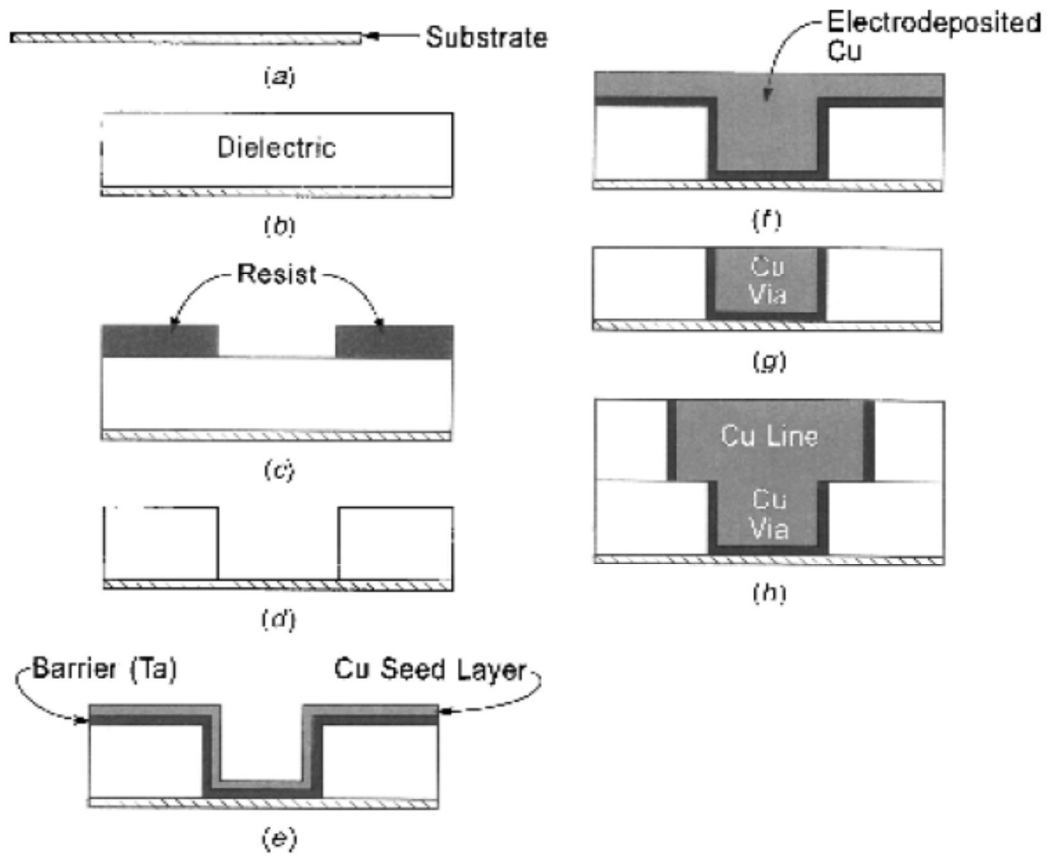


Figure 2.16: Different steps involved in the electrodeposition of Cu interconnects on silicon wafers.

Chapter 3 Materials and Methods

This chapter briefly describes all types of materials and methods that were used during the whole research work. As the work was done on two types of metal matrix composites i.e. fibers reinforced and carbon nanomaterials reinforced composites, so the materials and methods used for each type of composite are described step by step.

3.1 Materials

3.1.1 Metal matrices

The nickel metal was used as the metallic matrix for both types of composites i.e. fiber reinforced composites and carbon nanomaterials reinforced composites. The method employed to produce the composites was electrodeposition. In case of fiber reinforced composites, 99.98% pure Ni anodes of size 20 x 5 x 1 cm obtained from Coventia Srl. were used for the deposition of nickel metal. Whereas for carbon nanomaterials' reinforced composites; 99.98% pure Ni plates of size 10 x 2.5 x 1 cm were used as anodes. The anodes used along with their respective XRD scans are shown in the Figure 3.1 and Figure 3.2 respectively

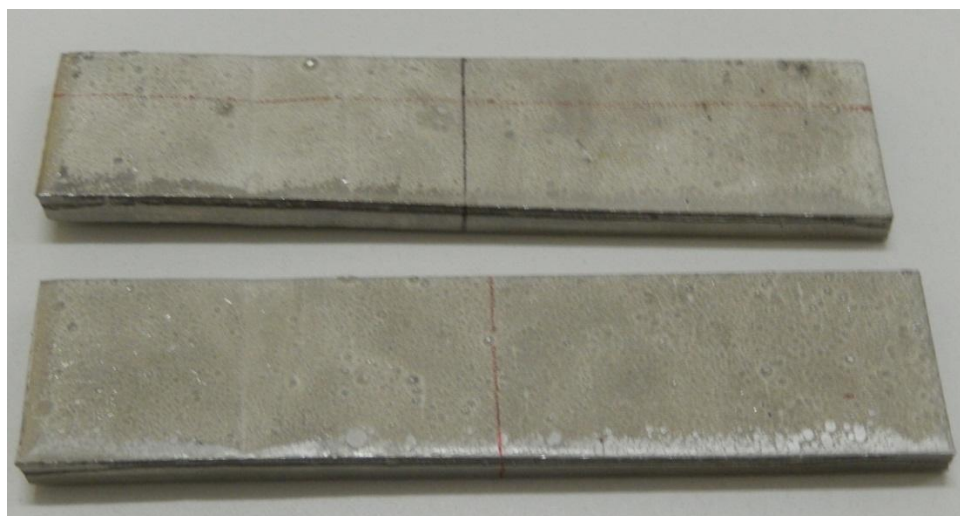


Figure 3.1: Nickel Anodes used for electrodeposition of Nickel

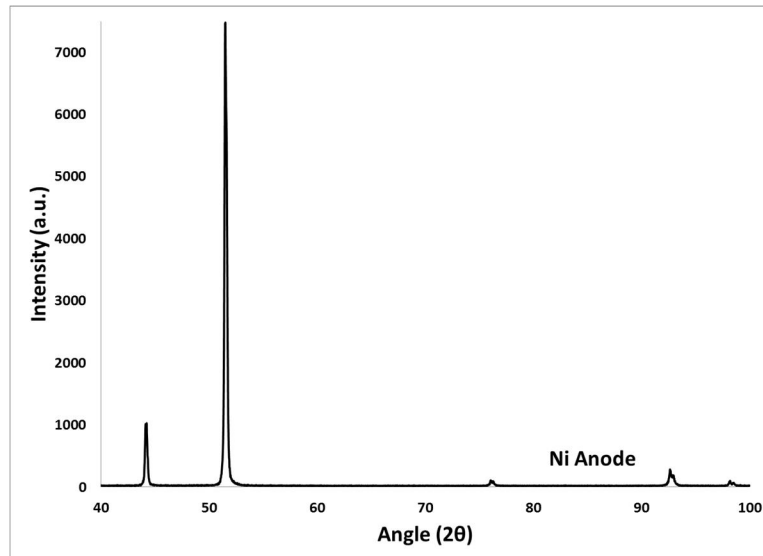


Figure 3.2: XRD pattern of Ni anodes used for electrodeposition

3.1.2 Reinforcements

For fiber reinforced metal matrix composites, monofilament silicon carbide (SiC) fibers (SIGMA 1140+, tungsten core, C coated, diameter 106 μm) were used as reinforcements. Whereas, graphene nanoplatelets (GNPs) and graphene oxide (GO) were used as nano reinforcements in the carbon nanomaterials reinforced metal matrix composites. The specifications of the each of these carbon nanomaterials are given in Table 3.1 and Table 3.2 while the XRD scans are shown in Figure 3.3. Also SEM micrographs of the carbon nanomaterials used are shown in Figure 3.4.

Table 3.1: Specifications of GNPs and CNTs

| Nano material | Purity (wt%) | Diameter | Grade | Surface Area | Manufacturer |
|---------------|--------------|-------------------|-------|----------------------------|----------------|
| GNPs | >99% | 1-2 μm | 4 | >700 m^2/g | Cheaptubes USA |

Table 3.2: Specifications of Single Layer, 2-4 Layers and 4-8 Layers Graphene Oxide (GO)

| Nanomaterial | Purity (wt.%) | Thickness | X-Y Dimension | Production Method | Manufacturer |
|-----------------|---------------|------------|---------------|-------------------|----------------|
| Single Layer GO | >99 | 0.7-1.2 nm | 300-800 nm | Modified Hummer's | Cheaptubes USA |
| 2-4 Layers GO | >99 | 2-4 layers | 300-800 nm | Modified Hummer's | Cheaptubes USA |
| 4-8 layers GO | >99 | 4-8 layers | 300-800 nm | Modified Hummer's | Cheaptubes USA |

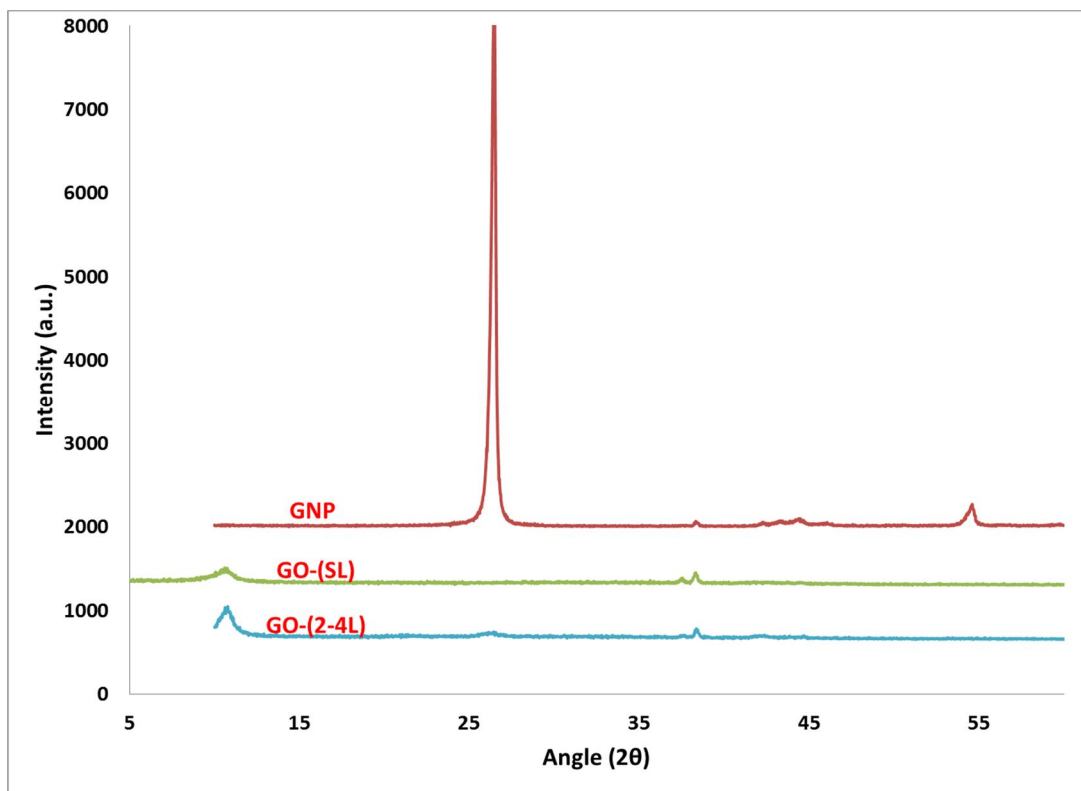


Figure 3.3: XRD patterns of GNPs, SLG and, 2-4LGO

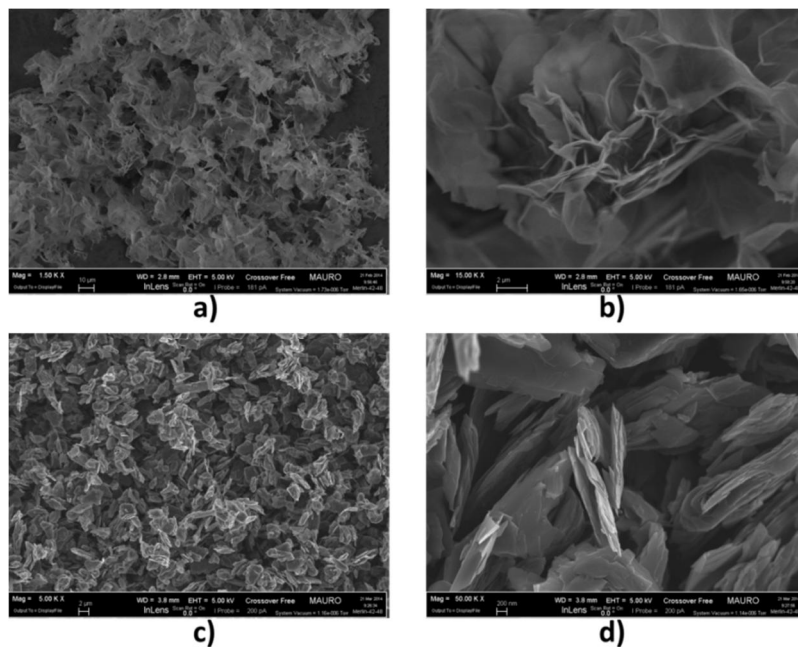


Figure 3.4: SEM images of used carbon nanomaterials: a),b) 2-4LGO and; c),d) GNPs grade4

3.1.3 Surfactants or dispersing agents

For deposition of a uniform composite layer over the substrate, it is important that the carbon nanomaterials should be properly dispersed in the deposition bath. And this dispersion should be stable for a sufficient period of time that is needed for depositing the required thickness of the composite. Some dispersing agents or surfactants can be applied to achieve this goal. Surfactants are the chemical species that modify the surface properties of particles and as a result of which the nature of the interactions between particles is also changed. The word surfactant is basically a short and composite form of the terms SURFace – ACTIVE – AGENT. Surfactants can serve a lot of purposes for example they can be used as dispersants, flocculants, deflocculants, flattening agents, wetting agents etc.

In this research work a surfactant was needed as a dispersing agent. Many surfactants were tried to choose the most suitable one for the required purpose. sodium dodecyl sulphate (SDS), poly acrylic acid (PAA) with mean molecular weight MW 5100, poly sodium naphthalene sulphonate (PSNS), poly sodium styrene sulphonate (PSS). All of these chemicals were purchased from Sigma Aldrich company. The chemical formulas of these surfactants are shown in Figure 3.5. Of all the tried surfactants, poly sodium styrene sulphonate was found relatively more useful and effective in dispersing the

carbon nanomaterials for longer periods of time due to its acidic nature and a pK_a value comparable with the acidic nature of the deposition baths.

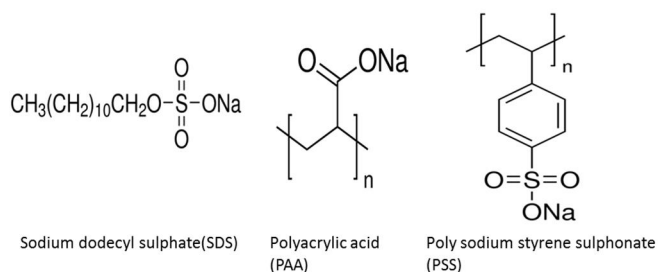


Figure 3.5: Different types of surfactants used

3.1.4 Conducting substrates

Substrates were used as cathodes to deposit composite layers on them. In case of fiber reinforced composites, Inconel 718 was used as cathode whereas; 42CrMo4 steel was used as cathode for depositing carbon nanomaterials reinforced composites on it. The chemical compositions for the both substrates are given in Table 3.3 and the XRD scans are shown in Figure 3.6.

Table 3.3: Chemical compositions of Inconel-718 and 42CrMo4-Steel

| Element (%) | Inconel-718 | 42CrMo4-Steel |
|-------------|-------------|---------------|
| C | 0-0.08 | 0.38-0.45 |
| Cr | 17-21 | 0.90-1.20 |
| Mn | 0-0.35 | 0.50-0.80 |
| Mo | 2.8-3.3 | 0.15-0.25 |
| Si | 0-0.35 | 0.17-0.37 |
| S | 0-0.15 | <0.035 |
| Fe | 17-17 | Rest |
| Al | 0.2-0.8 | - |
| B | 0-0.006 | - |
| Co | 0-1 | - |
| Nb | 4.75-5.5 | - |
| Cu | 0-0.3 | - |
| Ni | 50-55 | - |
| P | 0-0.015 | - |
| Ti | 0.65-1.15 | - |

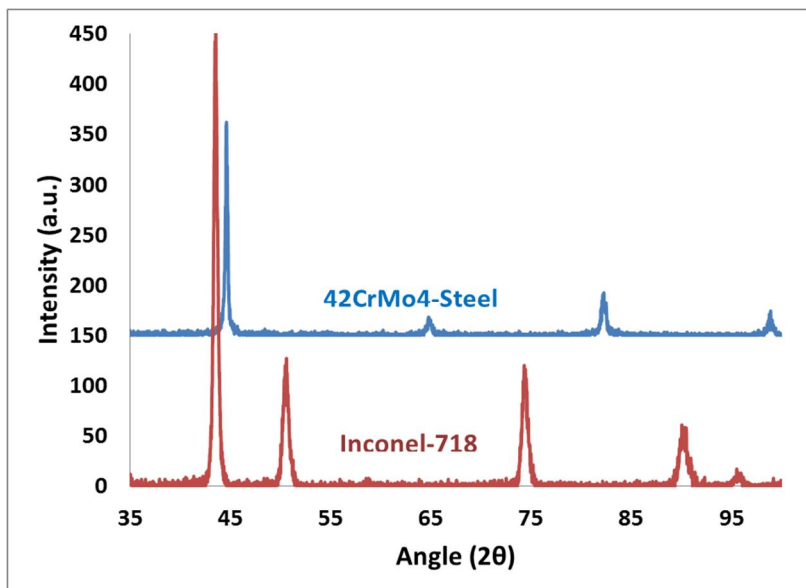


Figure 3.6: XRD of Inconel-718 and 42CrMo4 Steel Substrates

3.1.5 Deposition baths

The composites were deposited from electrolytic solutions on to the conducting substrates. The solutions used for the electrochemical deposition of nickel were Watt's bath ($\text{NiSO}_4 + \text{NiCl}_2 + \text{H}_3\text{BO}_3$) and Wood's bath ($\text{NiCl}_2 + \text{HCl}$) purchased from Coventia Srl. In case of fiber reinforced composite depositions, no additives were used in the deposition bath. Whereas in case of carbon nanomaterials reinforced composites, various surfactant additives were used in order to well disperse the nano particles in the bath so to ensure their uniform codeposition. The composition details of the deposition baths utilized in this work are shown in the Table 3.4.

Table 3.4: Compositions of Deposition Baths

| Composition of Watt's bath | Composition of Wood's bath |
|--|---|
| $\text{NiSO}_4 = 240\text{-}300 \text{ g/l}$ $\text{NiCl}_2 = 30\text{-}90 \text{ g/l}$ $\text{H}_3\text{BO}_3 = 30\text{-}45 \text{ g/l}$ | Nickel Chloride (NiCl_2) Hydrochloric Acid (HCl) |

3.2 Methods

3.2.1 Electrodeposition of fiber reinforced composites

The SiC long fiber reinforced Ni metal matrix composites were prepared by electrodeposition of nickel on a superalloy substrate over which the silicon carbide fibers had previously been positioned. All the composites specimens were obtained by means of a switching rectifier AF00 by Giussani S.r.l. The set up for electrodepositing the fiber reinforced composites is shown in the Figure 3.7.

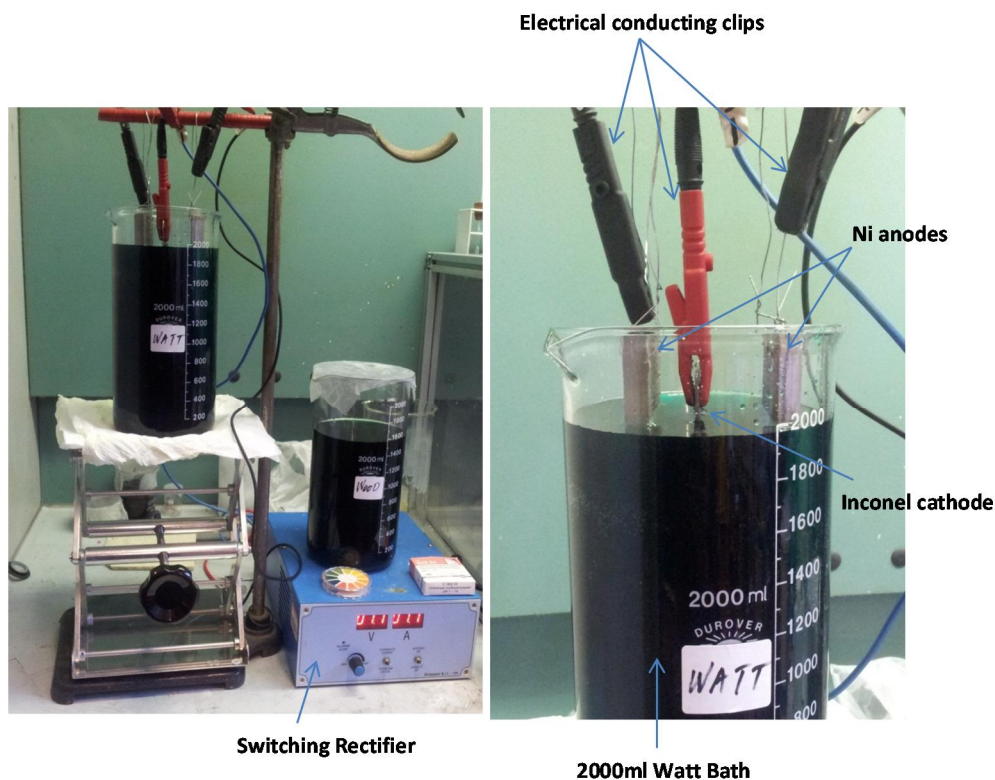


Figure 3.7: Setup for electrodeposition of Ni/SiC composites over Inconel-718

The process involved various steps (Figure 3.8). The first step was polishing and electrochemical pre-cleaning with a solution containing sodium hydroxide and complexing agents and surfactants, in order to obtain clean surfaces for the subsequent deposition steps. A current density of 2 A/dm^2 for 5 minutes at 298 K (25 °C) was applied to the solution, where two steel plates acted as cathodes and the superalloy as anode. Electrical contact was achieved by conducting clips.

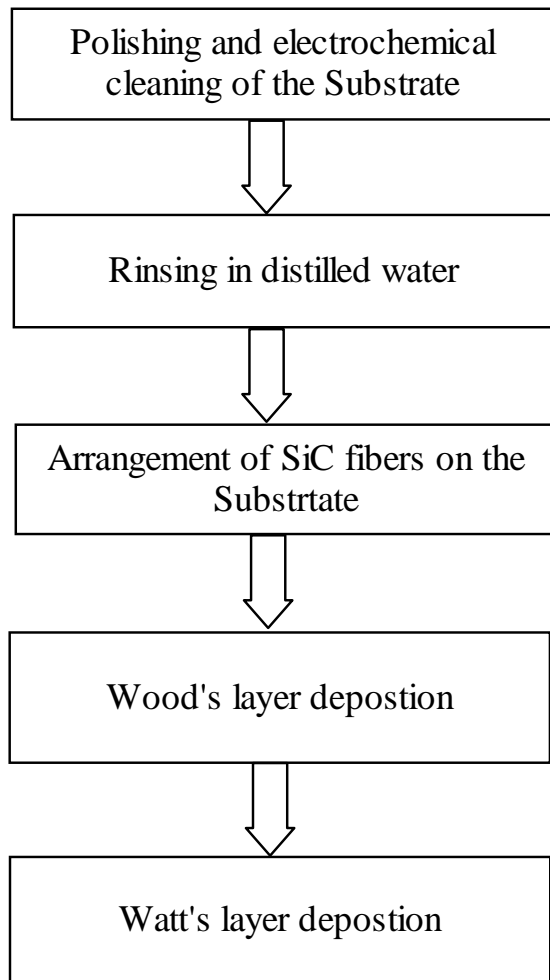


Figure 3.8: Experimental steps in the preparation of Ni/SiC composites

The second step was the arrangement of the fibers on the cleaned superalloy. The fibers were uniaxially positioned on a 180 x 20 x 2 mm superalloy Inconel 718 substrate and fixed at both ends by an epoxy resin. The substrate surface had been polished over 80-grit sandpaper, and the fibers were arranged manually on both sides of the support, creating a parallel array of roughly equidistant fibers, the mean distance between fibers ranging from 300 to 650 μm , corresponding to samples with a mean value between 30 and 40 fibers/cm. The samples after arrangement of the SiC fibers on them are shown in Figure 3.9 while after electrodeposition in Figure 3.10.

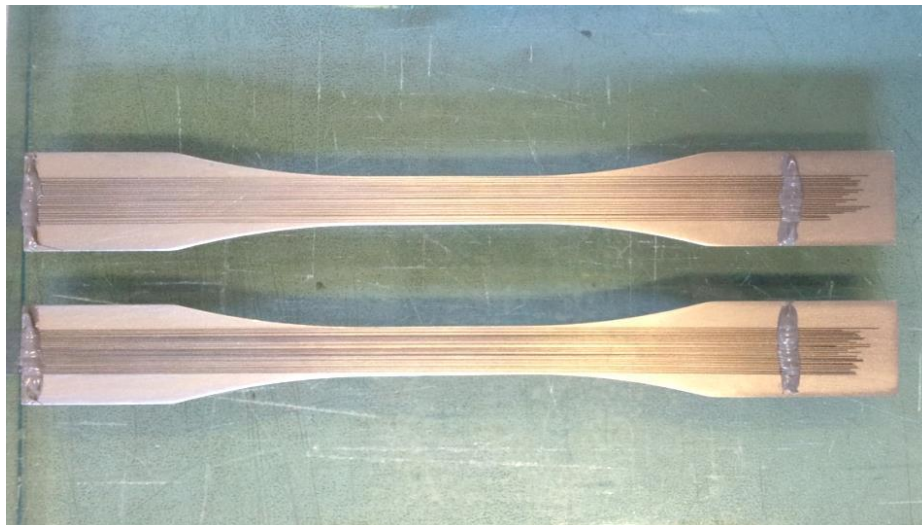


Figure 3.9: Inconel 718 substrates after arrangement of SiC fibers on them

The third step was the nickel deposition. In the first attempts, the support with the fibers was placed in a Watts' solution and electrically connected with two nickel plates and the switching rectifier. The deposition parameters, in particular temperature and current density, were optimized in order to find the best compromise between deposition rate and homogeneity of nickel deposit.

All the subsequent samples were realized at room temperature i.e. at 298 K (25 °C) and 2 A/dm². Since the fiber diameter is 106 μm, the deposition time was set to 5 hours, to be sure that complete coating of fibers and substrate was attained.



Figure 3.10: Inconel 718 substrates after deposition of Ni/SiC composites on them

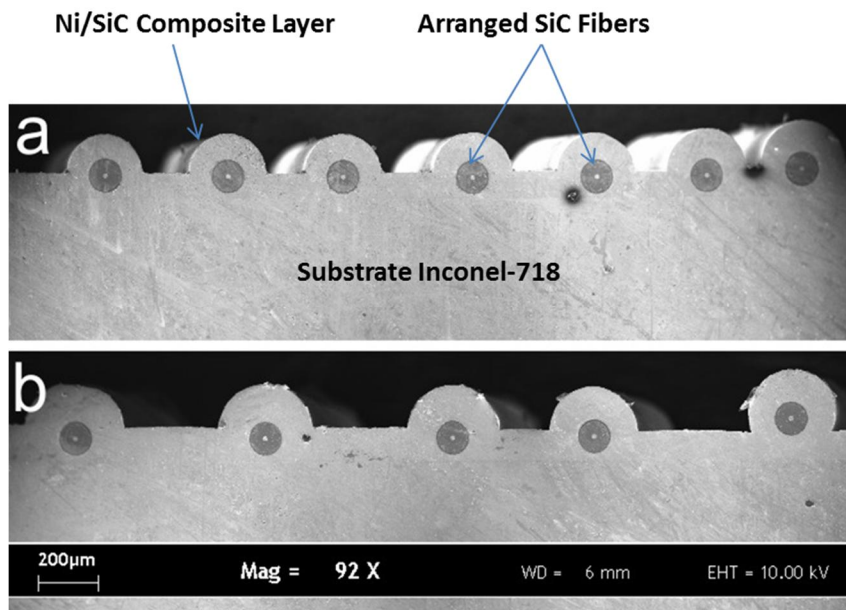


Figure 3.11: Typical sections of the Ni/SiC composite layers on Inconel 718: (a) sample with 40 fibers/cm/side (b) sample with 30 fibers/cm/side

To improve the quality of the interface between superalloy and nickel, an additional step was envisaged, i.e. the pre-deposition of nickel by means of a Wood's bath. This solution is quite aggressive, and it proved able to provide a better contact surface between superalloy and deposited nickel. The procedure consisted in placing the cleaned superalloy in a Wood's solution at $T=298\text{K}$ ($25\text{ }^{\circ}\text{C}$) for 5 minutes, with a current density of 4 A/dm^2 . After that, the samples were immersed in the Watts' solution and the deposition proceeded for 5 hours at 298K ($25\text{ }^{\circ}\text{C}$) and a current density of 2 A/dm^2 . Microstructures of the produced composites are shown in Figure 3.11.

3.2.2 Electrodeposition of carbon nanomaterials reinforced composites

The experimental steps involved in the preparation of carbon nanomaterials reinforced metal matrix composites are shown in Figure 3.12. First step in the preparation of nanocomposites was the preparation of stable suspensions of the nanomaterials (GNPs, GO) in the nickel deposition baths. This stability was achieved by adding suitable surfactants and dispersing the baths by a number of techniques. At first, the composition baths were dispersed by using ultrasonic agitation for 30 minutes with a probe (Sonics VCX750) and then the baths were left overnight on magnetic stirrer for 12 hours at 200 rpm. After 12 hours magnetic stirring the, the baths were again probe ultra sonicated for 15 minutes before starting the deposition process.

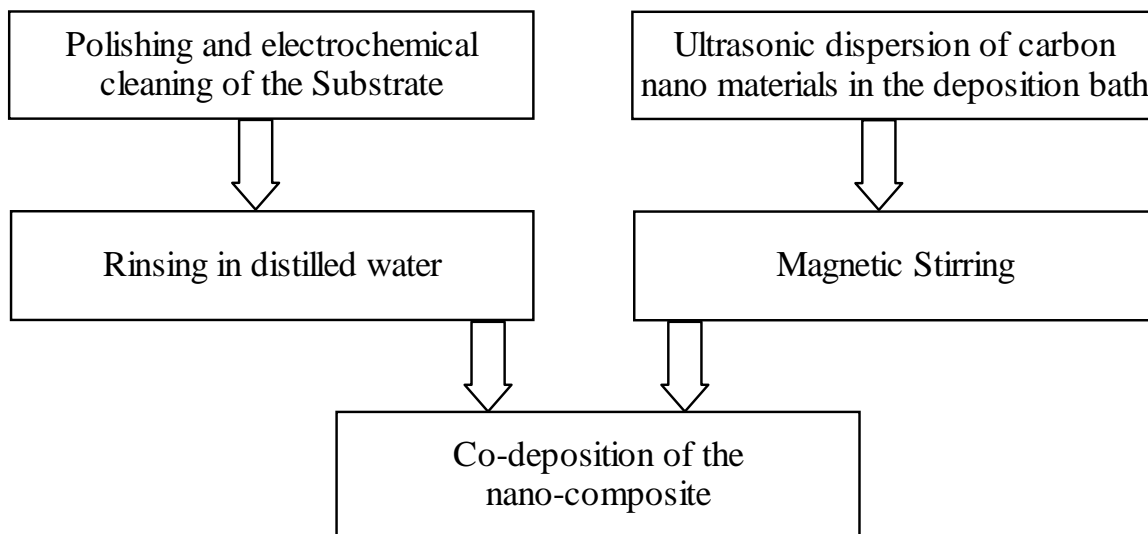


Figure 3.12: Experimental sequence for the codeposition of nano-composites

To ensure the homogeneity of the baths, gentle magnetic stirring at 100 rpm was done during the deposition process too. The 42CrMo4 steel radial substrates of 24mm diameter were electrochemically cleaned in a sodium hydroxide solution for 5 minutes, by utilizing a three electrode cell where substrate to be cleaned acted as anode and two mild steel plates of size 10x5x.01 cm acted as cathodes. This electrochemical cleaning was done at current density of 2 A/dm² followed by rinsing and 5 minutes bath ultrasonication in an acetone solution. After cleaning in acetone solution the substrates were rinsed again before starting the final deposition step. Again, a three electrode cell was used for the codeposition of nano-materials and metal matrices, where substrate were made to act as cathode for deposition on them and pure Ni plates acted as anodes. The co-deposition was carried out at room temperature using a current density of 2 A/dm² for 5 hours. The approximate thickness of the co-deposited composite coatings was about 100 μm. The electrochemical depositions for producing the codeposited nano composites were done by means of a switching rectifier AF00 by Giussian S.r.l. The deposition was realized at 25 °C with a controlled pH in the range between 3 and 4.

The deposition set up utilized for metal matrix nano composites is shown in the Figure 3.13.

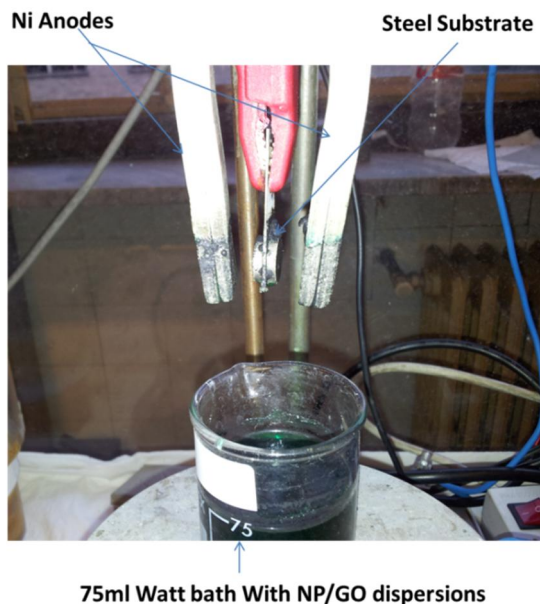


Figure 3.13: The electrodeposition set up utilized for production of nickel matrix nanocomposites

Samples of nanocomposites coatings deposited on steel substrates are shown in Figure 3.14.



Figure 3.14: Picture of Ni-coated (left) and uncoated (right) samples

3.3 Techniques used for characterizing the electrodeposited composites

Ni/SiC composites deposited on the Inconel 718 were characterized by optical microscopy, scanning electron microscopy, Mechanical Testing at room temperature as well as at higher temperatures. Before that, the chemical feasibility of Ni/SiC composite with the Inconel 718 substrate was studied by using the Differential Thermal Analysis

(DTA) and X-ray diffraction (XRD) techniques. The change in microhardness of the superalloy at different temperatures was also recorded using Vickers microhardness tester.

In case of CNT, GNP and GO reinforced nickel matrix composites, the morphology of the samples was studied by using Reichert-Jung MeF3 optical microscope (Leica Microsystems S.P.A, Austria) and Hitachi S4000 scanning electron microscope. The microhardness was tested using a LEICA VMHT hardness tester. The wear properties were studied by using a pin on disk apparatus, by using a pin of Co-cemented WC, with 3 mm radius. Surface roughness profiles were also measured by using as surface profilometer HOMMEL TESTER T1000.

The details of each of these facilities used in characterization of all the electrodeposited composites are given below.

3.3.1 Optical microscopy

Microscopy is a characterization tool used by the metallurgists, physicists, biologists and many other scientists to study micro details of the objects under investigation. The value of microscopic examination in the study of materials has been firmly established and there are a lot of microscopic techniques developed by the scientists for this purpose of studying the microscopic level details of the materials (Philips 1971; McLaughlin 1975; Gifkins 1970; McLaughlin 1977; Zieler 1972). Among these, optical microscopy is very simple and commonly used microscopic examination technique. Although optical microscopy does not give field depth analysis and also it lacks the resolution than the electron microscopy has but it is still very important technique for the metallurgists and other scientists. There are a few possible modes in the optical microscope that can be utilized depending upon the details of the specimen that are to be observed. For example for opaque samples bright field mode is preferred and for other details the observer can chose others illumination procedures. But in all cases, the sample must be well prepared and polished because if the sample is not well prepared then even the most powerful technique will not be able to reveal the required details in the microstructure (Voort 1999).

Optical microscopes are based on the principle of wave nature of light and they can be very simple consisting of one lens or they can have two or more than two lenses when they are called compound microscopes (Rochow & Rochow 1995).

The imaging principal for both types is explained in the following Figure 3.15.

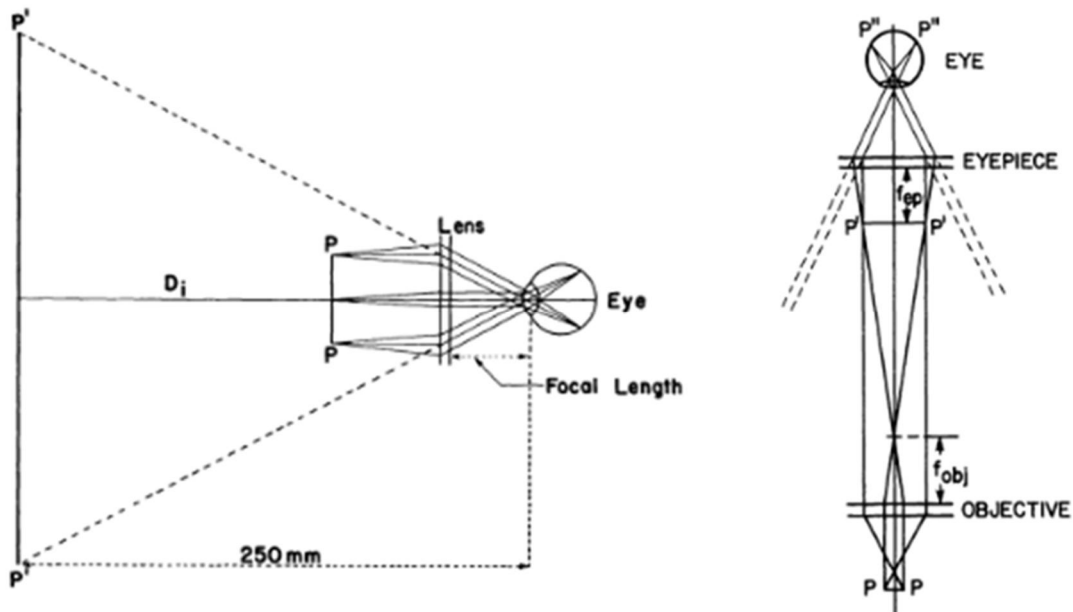


Figure 3.15: Light path in the simple microscope(left) and in the compound microscope(right) (Rochow & Rochow 1995).

The proper illumination of the microscope is important. This can be obtained by using condenser lenses. The resolution of the condenser lens is also as important as that of the objective. In the Figure 3.16 are shown different types of illuminations e.g bright field, dark field etc while Figure 3.17 shows the micrographs taken from optical microscope.

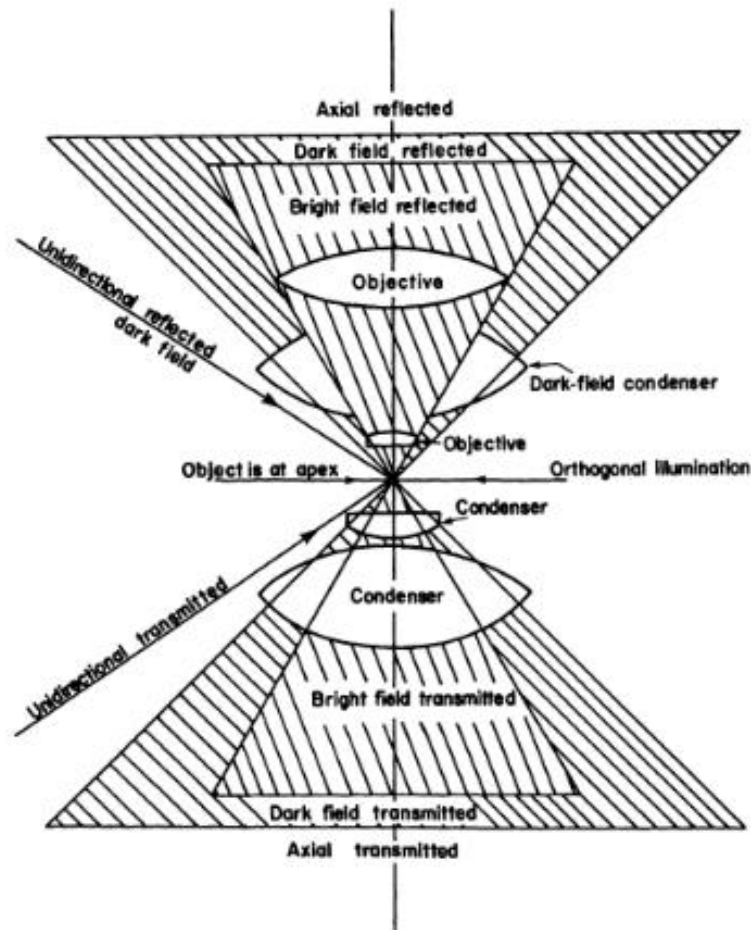


Figure 3.16: Main types of illuminations in an optical microscope (Osterberg 1950; Rochow & Rochow 1995)

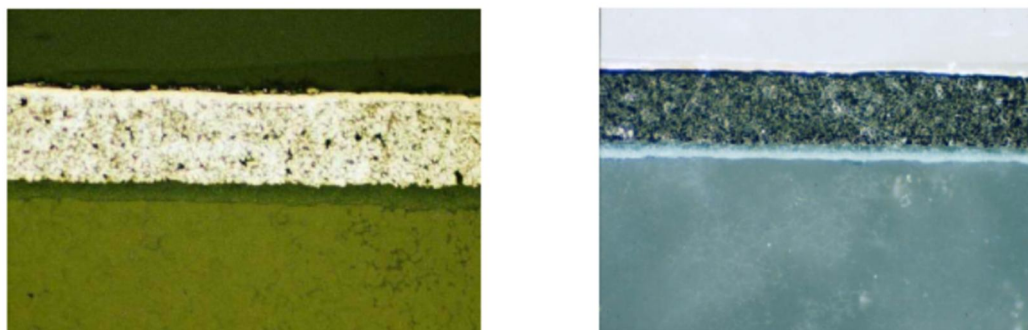


Figure 3.17: Micrographs of aluminum nitride electronic substrate in brightfield (left) and darkfield(right) modes (C. Zipperian 2011)

The resolving power of a microscope is the minimum distance (d) between two points of an object at which both points can be seen clearly separated and distinguished from

each other. Mathematically, this can be represented by the following equation (Rochow & Rochow 1995):

$$d_{min} = 1.22\lambda / (N.A_{objective} + N.A_{condenser}) \quad \text{Eq. 3.1}$$

Where; λ = wavelength of light, $N.A$ = the numerical aperture of lenses.

And the numerical aperture can be given by the equation:

$$N.A = n \sin \alpha \quad \text{Eq. 3.2}$$

Where n indicates the refractive index and α is the half the included angle of the lens.

Smaller the wavelength and larger the refractive index of the lens, better is the resolution of the optical microscope. 200 nm is an approximate theoretical limit of the optical microscope resolution (Yang et al. 2013).

It is possible to generate a micrograph of the specimens being observed under optical microscope by capturing the image by simple light sensitive cameras. These days the digital images can directly be seen on computer screens without needing an eyepiece. This has become possible by development in CMOS (complementary metal-oxide-semiconductors) and CCD (charged-coupled devices).

3.3.2 Stereo microscopy

Stereo microscopy also utilizes optical light just like in case of optical microscopes. But, in contrast to conventional optical microscopes, stereo microscopes enable to analyze, view and record the objects in more than one dimension i.e. it is possible to see the sample details in two or three dimensions. There are two separate optical paths in the stereomicroscope consisting of two objectives and two eyepieces. This arrangement cause two separate viewing angles on both eyes. With the help of this arrangement, the sample under observation can be visualized three dimensionally.

There are two main kinds of stereomicroscopes;

1. Binobjective-binocular stereomicroscope
2. Common main objective(CMO) binocular stereomicroscope

The 1st type i.e. binobjective-binocular stereomicroscope is a classical in the field of microscopy (Chamot & Mason 1958; Schlueter & Gumpertz 1976; McLaughlin 1975). It basically consists of two compound microscopes that are mounted on a single stand in such a way that each compound set is at slightly different angles from each other and the stereo effects can be further enhanced by placing a pair of prisms.

The second type of stereomicroscope i.e. CMO binocular stereomicroscope, contrary to the first type, consists of only one central objective. But similar to the binobjective binocular stereomicroscope, it also has two numbers of eyepieces. Due to CMO, image planes don't tilt toward each other and they are parallel to the plane of the object.

Both types of the stereo microscopes are shown in the Figure 3.18.

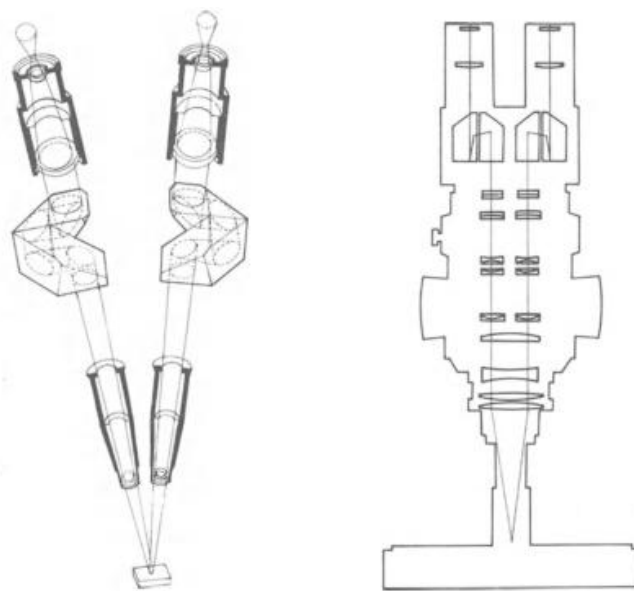


Figure 3.18: Binobjective-binocular stereomicroscope (left) and CMO binocular stereomicroscope (right) (Rochow & Rochow 1995)

The method of determining resolution power of the stereomicroscope is similar to that of the simple optical microscope i.e. it depends upon and is calculated from the numerical aperture and the illumination wavelength. Mathematically, it can be given by the Rayleigh criterion as:

$$\text{Resolution } (d) = 0.61\lambda/nsin\theta \quad \text{Eq. 3.3}$$

Where; d = the smallest possible resolvable distance, λ =the wavelength of light, n = refractive index of medium between the specimen and the objective, and θ =one-half of the angular aperture of the objective.

As in case of optical microscopes, CCD cameras can be coupled with stereo microscopes as well to record the structures on a computer connected with the system.

3.3.3 Scanning electron microscopy

Scanning electron microscopes have become very important in the field of characterization of materials. A scanning electron microscope (SEM) is a type of microscope that utilizes a focused beam of electrons to generate high resolution details of the objects under examination. Due to very short wavelength of bombarding electron beams, scanning electron microscopes have very high resolving powers, more depth of field and improved contrast than the optical microscopes. (Rochow & Rochow 1995)

The schematic setup for a scanning electron microscope labelled with important parts is shown in the Figure 3.19

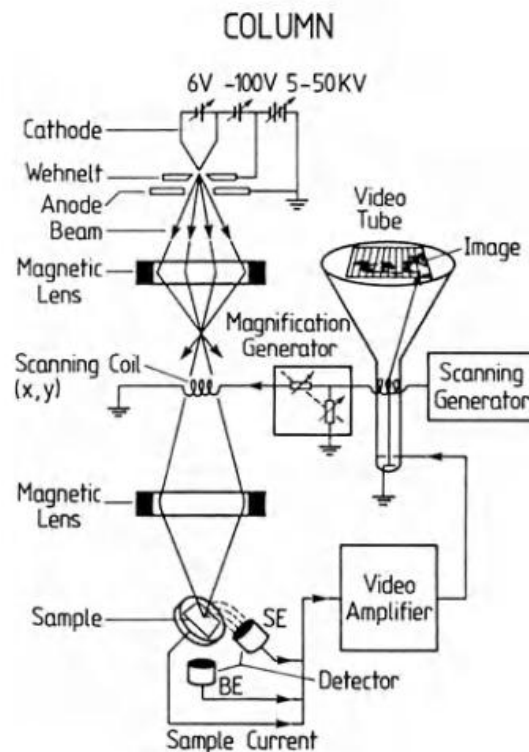


Figure 3.19: Schematic Setup of Scanning Electron Microscope (Luth 1995)

There can be listed several steps to state the imaging process of a scanning electron microscope as given below:

1. A flux of free electrons is created in an electron gun. Electron gun consists of W filament cathode that generates these electrons by thermionic emission process.
2. The electron flux generated by the electron gun is accelerated down in an optical column with the help of high voltage potentials created at the anode.
3. Condenser lenses convert this flux of electrons into a beam of electrons
4. The current of this beam of electrons can be regulated by the condenser lenses and beam regulation aperture.
5. A stigmator is used to remove the ellipticity of the electrons beam
6. A final condensing lens fixes the beam of electrons onto a probe spot.
7. The electron beam bombards on the surface of the sample and as a result of which following types of signals are produced:

Secondary electrons (SE): These are low energy electrons that are emitted from the nearer surface of the sample. These electrons can be collected in a secondary electron detector to get a topographic information of the sample.

Back scattered electrons (BSE): These are actually the bombarded electrons which are scattered back from the inner part of the sample little below the surface. They are higher density electrons than the secondary electrons. As these electrons come almost from the bulk of the sample so they contain information about the density depending upon the average atomic mass and we can say that the image also has information about the compositions of the chemical components of the sample.

X-rays: X-rays are also generated from the sample that can be resolved on the basis of their wavelengths or energies. The characteristic waves resolved on the basis of energy are collected in the Energy Dispersive X-ray (EDX) Analyzer for composition analysis. Whereas, it is also possible to resolve X-rays by diffraction phenomenon through a regular and periodic solid and can be collected in a gas filled counter called Wavelength Dispersive Spectrometer (WDS).

In addition to the secondary electrons, back scattered electrons and X-rays, light photons or heat is also generated as a result of the electrons beam bombardment on the

sample under observation. Generally the secondary electrons come from top few nanometers of the volume of the sample. Whereas the back scattered electrons come from top 40% of the volume and X-rays are emitted from the entire region of bombardment.

Volume and mechanism of electron matter interactions in scanning electron microscopy is shown in the Figure 3.20.

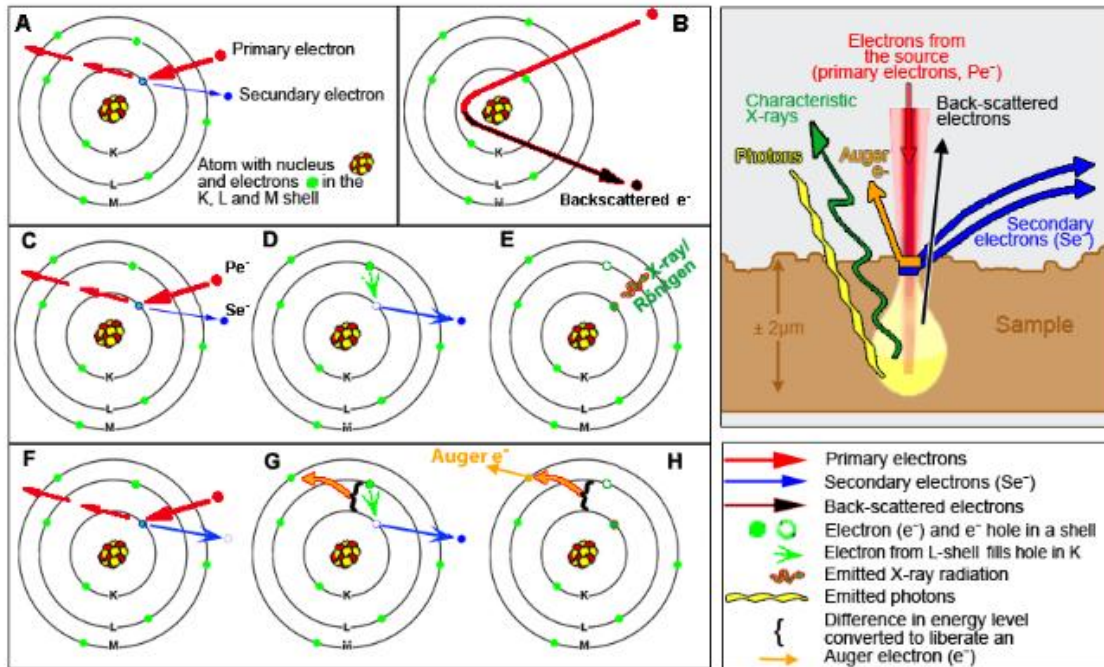


Figure 3.20: Volume and mechanism of electron matter interactions in scanning electron microscopy

3.3.4 X-ray diffraction

X-rays are electromagnetic waves that have 0.01-10 nm wavelength range and have energies in the range of about 100 eV to 10 MeV. These electromagnetic waves travel with the velocity of light and can behave just like particles according to the quantum theory. X-rays were discovered in 1895 by a German physicist Roentgen.

X-rays are produced in an X-ray tube that consists of a tungsten filament. Electrons are generated by the W-filament by thermionic emission and they are made to strike on the anode material by applying voltage. As a result of electrons bombardment on the target metal X-rays are produced that are passed through the windows W to get out of the X-ray tube (Figure 3.21).

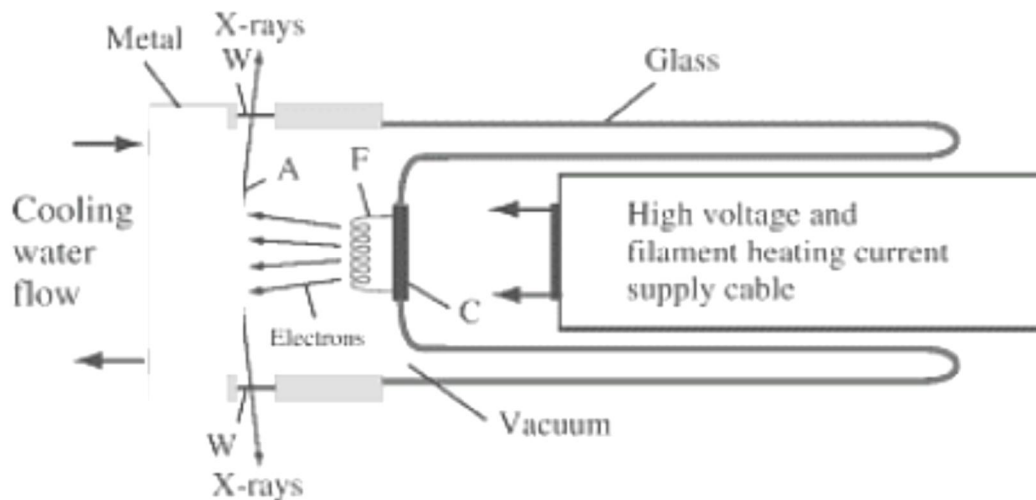


Figure 3.21: Schematic of an X-ray tube for the production of X-rays (Graef & E. McHenry 2007)

The X-ray tube contains filament F, target metal T and windows W through which X-rays come out of the tube.

In the Figure 3.22 is shown a schematic representation of the spectrum of X-rays produced from molybdenum target as a function of the applied voltage. There are two types of signals. One is the white signals while the others are characteristic radiations K_{α} and K_{β} . In X-ray diffraction analysis of materials we want only the characteristic portion of the X-ray spectrum so we need to get rid of the white portion. This is done by applying filters. Generally the filter material selected is of 1 atomic number (Z) less than the atomic number of the anode material used for the generation of the X-rays. A Schematic of copper radiation before and after passing through a nickel filter is shown in the Figure 3.23.

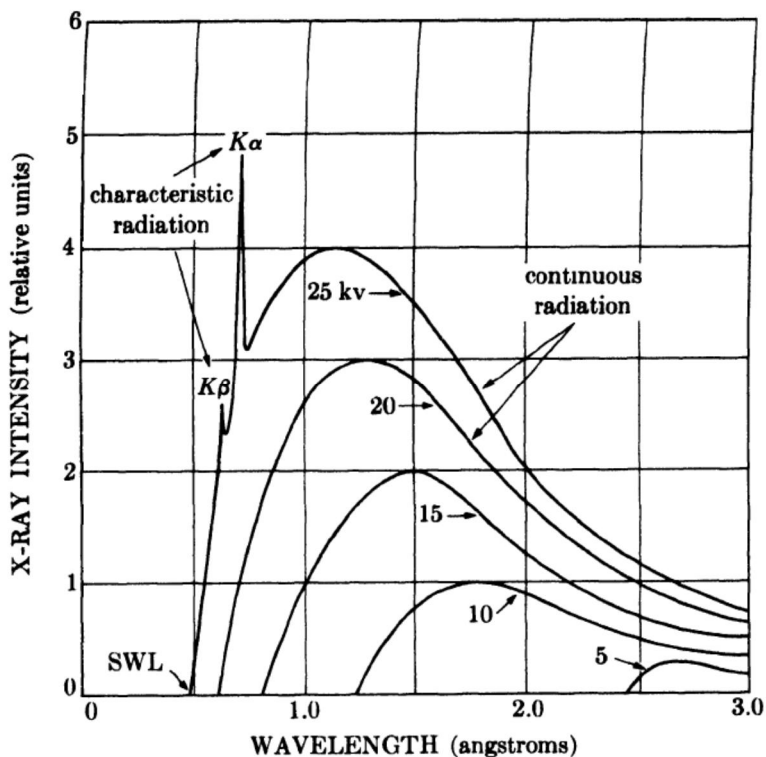


Figure 3.22: Typical X-ray spectrum of molybdenum as a function of applied voltage (Cullity 1956)⁷

Table 3.5: Characteristic radiations of some commonly used anodes and filters used for them

| Target | Filter | K_{α} | $K_{\alpha 1}$ | $K_{\alpha 2}$ | K_{β} | K abs. edge |
|--------|--------|--------------|----------------|----------------|-------------|-------------|
| Cr | V | 2.29092 | 2.08480 | 2.28962 | 2.29351 | 2.07012 |
| Fe | Mn | 1.93728 | 1.93597 | 1.93991 | 1.75663 | 1.74334 |
| Co | Fe | 1.79021 | 1.78892 | 1.79278 | 1.62075 | 1.60811 |
| Cu | Ni | 1.54178 | 1.54051 | 1.54433 | 1.39217 | 1.38043 |
| Mo | Zr | 0.71069 | 0.709226 | 0.713543 | 0.632253 | 0.61977 |

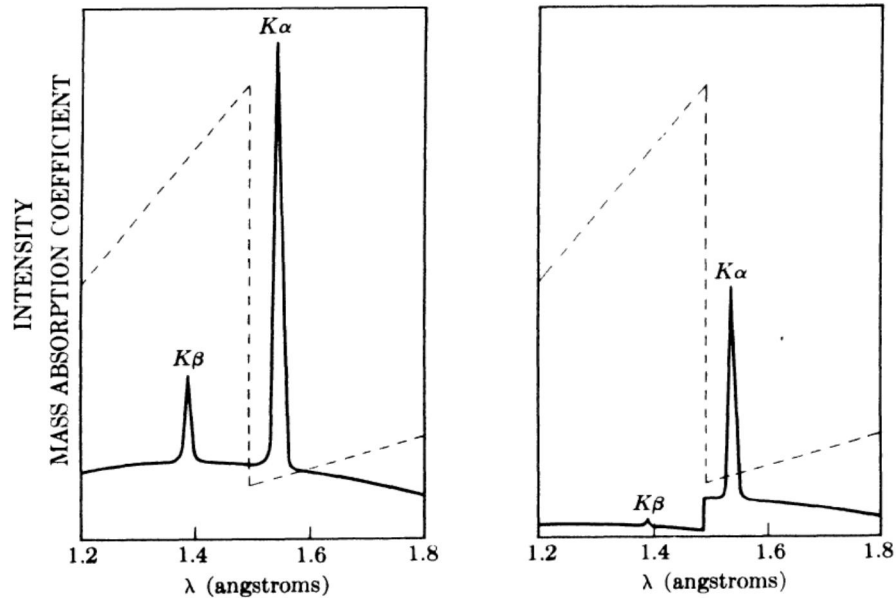


Figure 3.23: Schematic of copper radiation before (left) and after (right) passing through a nickel filter. dashed line shows the mass absorption coefficient of nickel (Cullity 1956)

When X-rays are incident on the materials, there are four main possible types of processes that can occur as the outcome (Figure 3.24). Some X-rays pass through the incident material (transmittance), some cause ejection of the electrons (photoelectric effect), some portion of them cause X-ray fluorescence while the others are scattered in various directions coherently or incoherently. The coherently scattered X-rays are used in the standard X-ray diffractometric technique for the analysis of materials nature and composition.

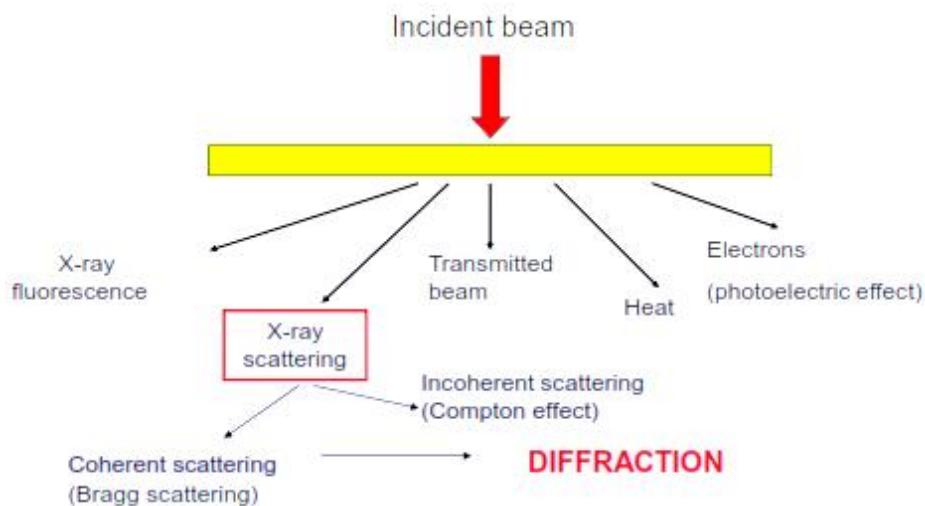


Figure 3.24: Interaction of X-rays with materials

The X-ray tubes are installed in the X-ray diffractometer equipment used to carry out the diffraction analysis of materials. A monochromatic beam of K_α radiations are struck on the samples after passing through the collimator and antiscatter slit. After the impingement on the sample, X-rays are scattered in various directions and they enter into an X-ray counter normally placed at the same angle as that of incident X-ray beam.

The main components of an X-ray spectrometer are shown in the Figure 3.25. They include an X-ray source F, sample holder S and detector G, Rowland circle passing through points F (target focal spot), S (center point of diffractometer), and G (the focal point of the diffracted beam), the divergent slits DS and the scattering slits SS, the receiving slit RS. (Waseda et al. 2011)

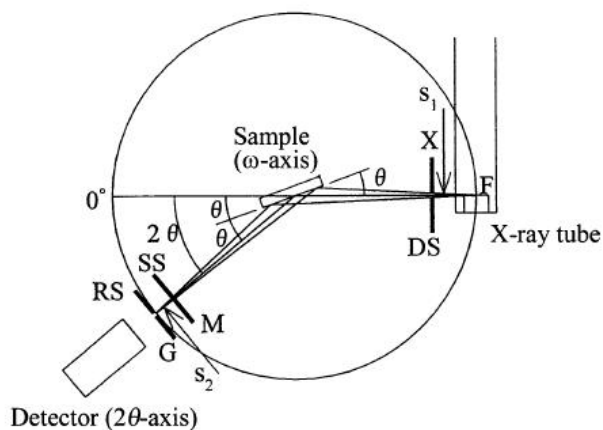


Figure 3.25: Schematic of a typical diffractometer (Waseda et al. 2011)

Elastically scattered X-rays from a crystal lattice can cancel each other (destructive interference) in some directions or can add up (constructive interference) in the other directions before entering to the counter. Bragg's law explains these diffractions as:

$$2d\sin\theta = n\lambda \quad \text{Eq. 3.4}$$

The Equation 3.4 is a well know Bragg's equation where d is interplaner distance, θ is the incidence angle, λ is the wavelength, of the incident X-rays and n is an integer.

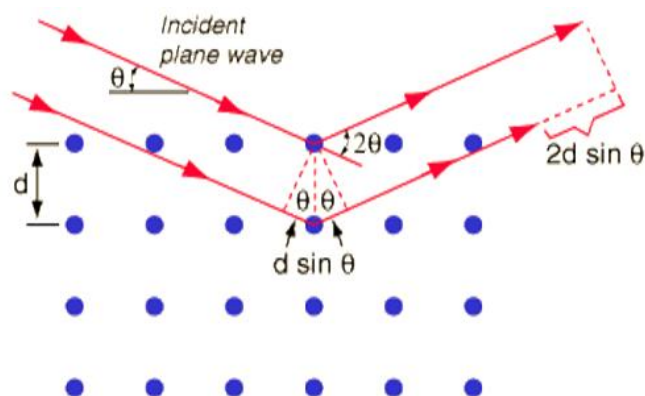


Figure 3.26: Interference of X-rays scattered by crystals

We get $I-2\theta$ data when X-ray source S is fixed and sample platform and counter rare is rotated at speeds of ω and 2ω separately. In this condition the diffractometer is called $\theta-2\theta$ type diffractometer. Whereas if the sample platform is fixed but X-ray source and the X-ray counter both rotate with a same speed of ω , then we obtain $I-\theta$ data. In this arrangement, the diffractometer is called $\theta-\theta$ type diffractometer. In this research $\theta-2\theta$ type scans were done by using a Philips diffractometer between 20 and 80° (2θ). The Cu K_α radiations with wavelength (λ) 0.1504 nm were used. The generator voltage and generator current were set to 40 kV and 20 mA respectively. Whereas $0.08^\circ/\text{min}$ was set as the speed of scanning and the step size used was 0.02° respectively.

The diffraction patterns obtained from the diffractometry can be used and analyzed to have a lot of useful information about the samples. From angular position (2θ) of the diffraction pattern peaks, we can have the knowledge about crystal system, spatial group symmetry, unit cell and the phases present. From the intensity I of the peaks give information about content of the unit cell, point symmetry, quantitative composition of the mixture as well as the preferred orientation or texture. Whereas from profile and width peak analysis of the diffraction patterns, we can have an idea about crystallite size (ranging from $1-100$ nm), defects, residual stresses and texture.

For crystallite size measurement from XRD patterns, an equation developed by Scherrer is used which is given as:

$$d = k\lambda/B\cos\theta \quad \text{Eq. 3.5}$$

where d is the crystallite size, K is a constant depending on the geometry of the grains, λ is the copper $K\alpha$ wavelength, B is the width of the XRD peaks (full width at half maximum, FWHM), and θ is the diffraction angle.

The value of the B is calculated by subtracting the width contributions due to the instrumental errors. The instrumental contributions to the peak width can be calculated by doing a reference scan on a well crystallized reference sample of Si or LaB_6 whose peak widths are only due to the instrumental effects.

The actual contribution just from the sample to the broadening of the peak is then calculated by the following equation:

$$B = (B_{obs}^2 - B_{ref}^2)^{1/2} \quad \text{Eq. 3.6}$$

The value of B obtained from the Equation 3.6 is then used in the Scherrer equation (Eq. 3.5) to have the crystallite size.

3.3.5 Mechanical characterizations

The mechanical characterization of the specimens was done by the following techniques

3.3.5.1 Tensile testing

Tensile testing is a very important testing method that is used for determining mechanical properties of different materials. These properties are very helpful in designing the components by keeping in view their service requirements. Tensile test is also known as tension test in which a specimen is held between two cross heads that move in opposite direction while a uniaxial load is applied on the specimen. This test basically measures the resistance of the materials against the applied load. The load applied can be static or slowly increasing with the time and deformation. (Askeland et al. 2010) The rate or velocity at which the cross head moves to deform the samples is known as strain rate. The same material behaves differently in a tension test if the strain rate used is different. So strain rate is very important in the tension tests. Normally strain rates are small (10^{-4} to 10^{-2} s^{-1}). Also the testing temperature is another important consideration as materials behave mechanically different at different temperatures. The strength of the materials is usually lowered with increasing the testing temperatures. We get the values of displacement against the applied load as the output of the tension test.

This displacement-load data then can be used to calculate engineering stress and engineering strains to have a stress strain plot. Mathematically, engineering stress and engineering strain can be represented as:

$$\text{Engineering Stress} = S = F/A_o \quad \text{Eq.3.7}$$

$$\text{Engineering Strain} = e = \Delta l/l_o \quad \text{Eq.3.8}$$

From the stress strain plot we can determine a number of important mechanical properties that are shown in Figure 3.27.

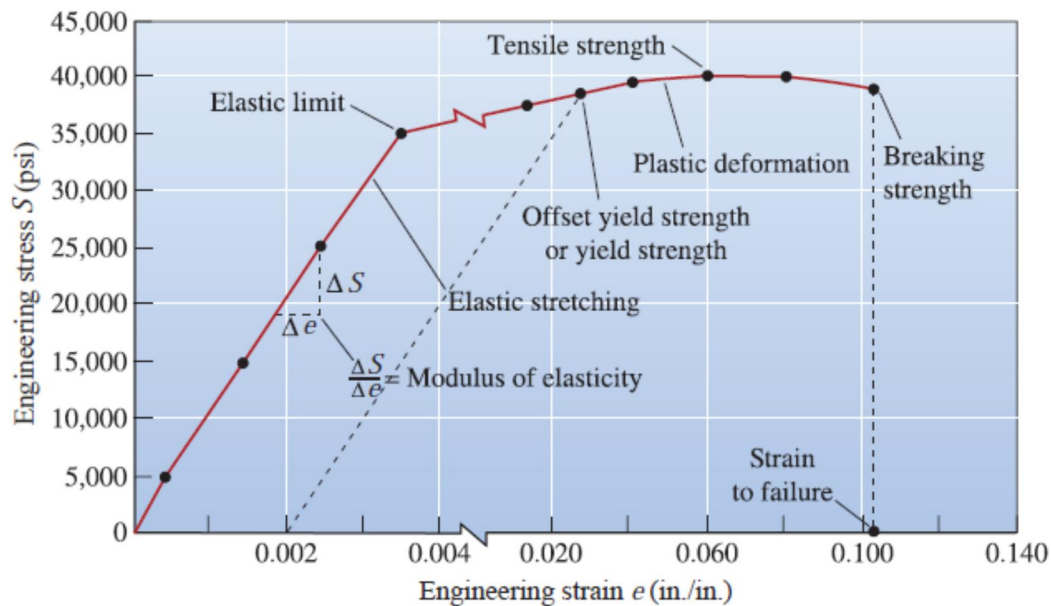


Figure 3.27: Typical engineering stress-strain curve for an aluminum alloy showing important points in it (Askeland et al. 2010)

Among all the properties that can be calculated from stress-strain plot, Young's modulus or the modulus of elasticity is more important. Modulus of elasticity is actually the material's resistance to elastic deformation and it can be calculated from the slope of the stress strain curve in the elastic region as represented in the Figure 3.27. Elastic modulus decreases with the increase in the testing/service temperatures. This typical effect is shown in Figure 3.28.

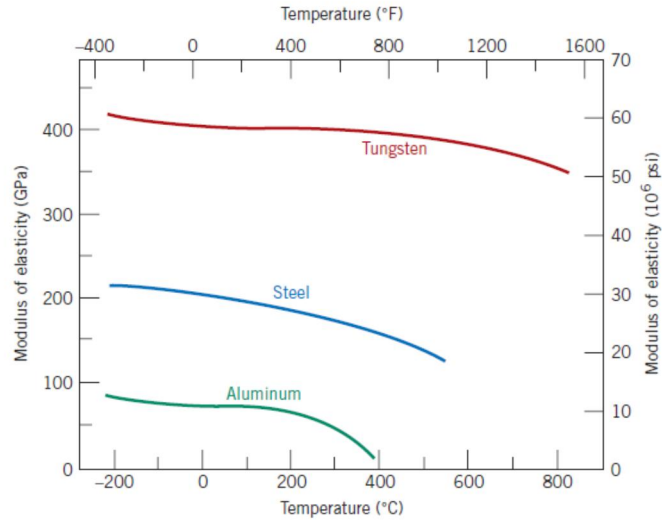


Figure 3.28: Effect of temperature on modulus of elasticity for different types of materials (Callister & Wiley 2010)

In this particular study, mechanical tensile testing of the SiC fiber reinforced nickel matrix composites deposited on Inconel-718 samples was done to evaluate the maximum load bearing capability and Young's modulus at room temperature as well as at 400 °C and 600 °C. The machine used for this purpose is shown in the Figure 3.29.

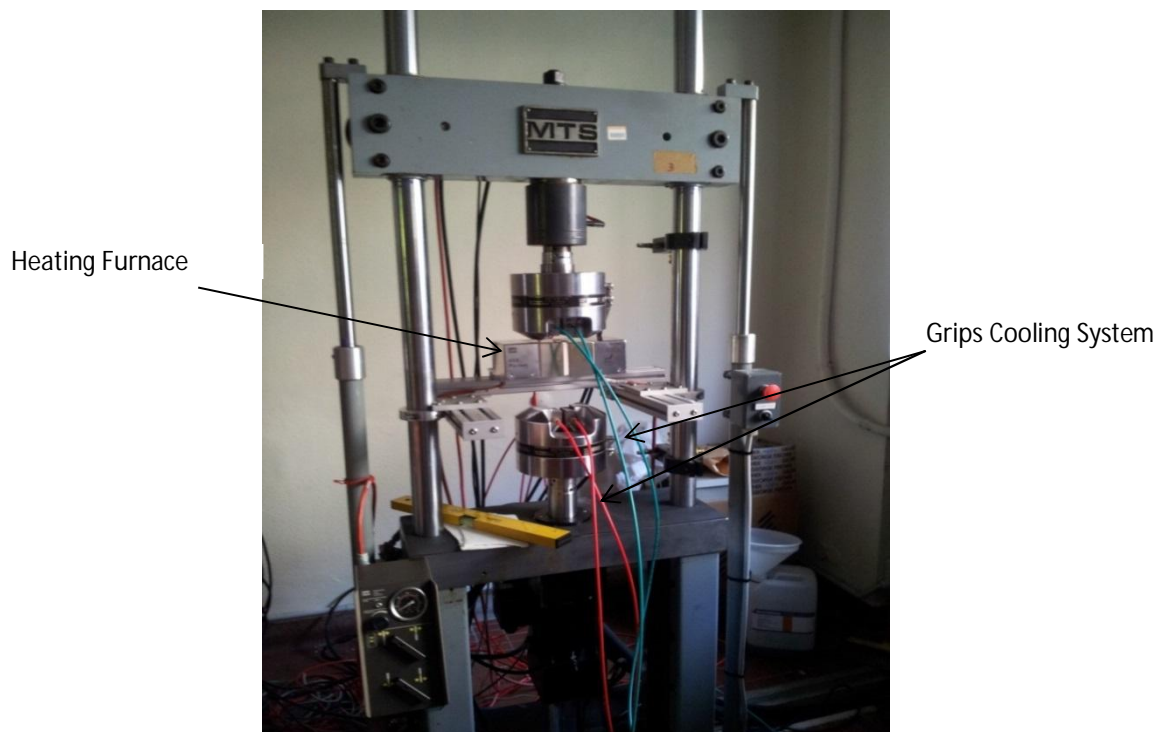


Figure 3.29: Tensile testing machine used for Ni/SiC fiber composites deposited on Inconel-718

This MTS testing machine (by MTS Systems Corporation, Minnesota, USA) was equipped with a 100 kN load cell, a furnace facility (MTS Series 653.02, a multi-zones temperature controller (type 409.83), an hydraulic wedge grips (MTS Series 647.10) and a water cooling system. All this arrangement made it possible to evaluate the mechanical behavior of the samples at higher temperatures as well. The samples were tested at room temperature, at 400 °C and 600 °C. While testing at high temperatures, the upper and lower head jaws for holding the samples are cooled down with water in order to avoid their heating and damage. The samples were prepared in standard dog bone shape with the dimensions as shown in the Figure 3.30.

Two testing velocities (strain rates) were used to deform the samples. First velocity was 0.05mm/min for about 15 minutes. In 15 minutes, yield point was crossed and after that the cross head speed was changed to 1.5mm/min until the fracture of the specimens.

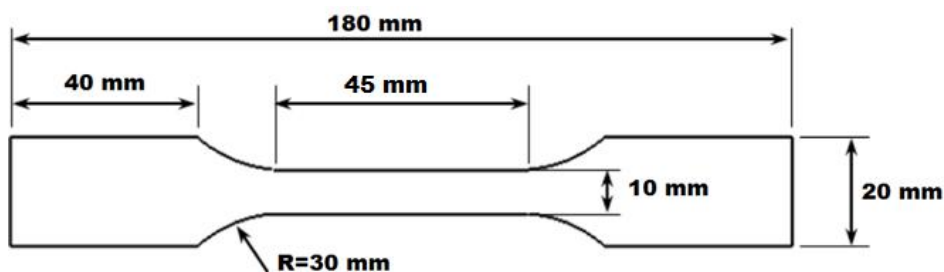


Figure 3.30: Schematic of dog bone specimen used for mechanical testing

The values of stress-strain and Young's modulus were then determined from the load-displacement data obtained from the tensile testing machines.

Some mechanical tests were performed on the nickel deposited single SiC fibers in order to study the interface resistance between nickel matrix and the silicon carbide fiber. The gage length of the fibers was 50 mm and a 100 N load cell was used.

The testing machine used for tension tests on the single fiber is shown in the Figure 3.31.



Figure 3.31: MTS machine used for single fiber testing

3.3.5.2 Microhardness testing

Like tensile strength, hardness of the materials is also used to assess the mechanical properties of a material. Hardness also gives the resistance of a material to plastic deformation under the applied load (Callister & Wiley 2010).

Many methods are used for the measurement of the hardness of materials. The commonly known methods are Brinell, Rockwell, Vickers and Knoop hardness testers. Among these, Vickers and Knoop hardness testers are characterized as microhardness testers because these can be used to estimate the hardness of very small regions at micrometer levels. They use much smaller loads (ranging from 1 to 2000 g) and a very small diamond indenter that is pressed in a well prepared and polished sample at a pre fixed load for a specific period of time. This causes an indent in the specimen. The diagonals of this indent, measured with the help of an optical microscope coupled with the indenter, give the Vickers hardness (HV) of the material.



Figure 3.32: Microhardness tester (Leica VMHT) used for Vickers hardness measurements

The HV number is given by the ratio F/A , where F represents the applied load on the sample through the diamond indenter in kilograms force and A denotes the surface area (in square millimeters) of the indent. Surface area A is calculated by the following formula:

$$A = d^2/2\sin\left(\frac{136^\circ}{2}\right) \quad \text{Eq.3.9}$$

Where d is the average value of two diagonals of the indent which is measured with the help of microscope. By evaluating the sine value, we get:

$$A \approx d^2/1.8544 \quad \text{Eq. 3.10}$$

As hardness is force per unit area, so Vickers hardness can be given as:

$$HV = F/A \approx 1.8544F/d^2 \quad \text{Eq.3.11}$$

Where HV is Vickers hardness and F is the force applied on the specimen.

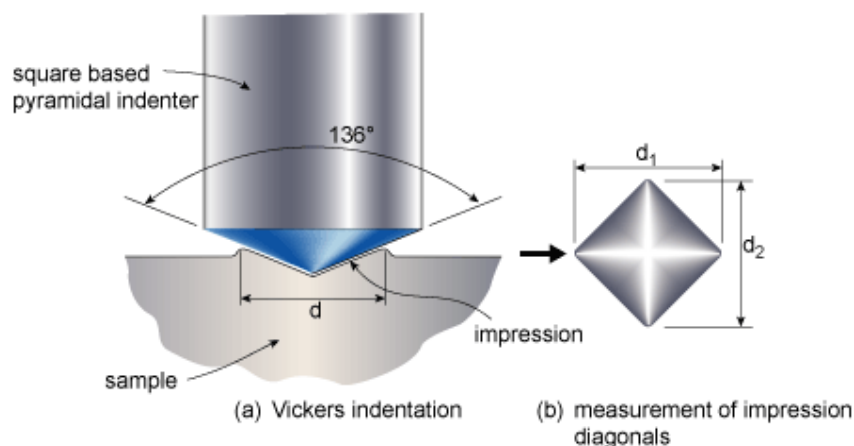


Figure 3.33: A schematic of Vickers indenting and diagonal measurement of the impression (Mathers 2014)

The values of hardness of materials are reported in such a way that one can have an idea about the force used along with the application time. For example 240HV 10/30 means that 240 is the Vickers hardness (Figure 3.34).

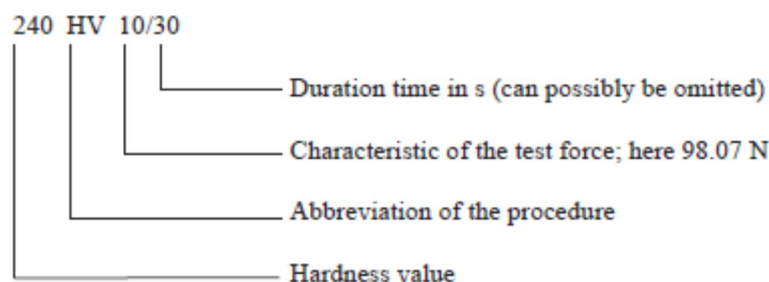


Figure 3.34: Abbreviation used for Vickers hardness readings (Herrmann 2011)

3.3.6 Techniques for dispersion of carbon nanomaterials

For the codeposition of carbon nanomaterials reinforced nickel matrix composites, a well stable and uniform dispersion of the nanomaterials in the deposition bath is necessary to get a uniform composite coating. Different types of techniques can be used to disperse the nano-phase in the nickel deposition bath. A brief description of the methods used is given below:

3.3.6.1 Ultrasonication

Ultrasonication is a technique in which ultrasounds energy is applied to a liquid or solution in order to agitate and uniformly disperse the second phase particles in it. The frequency of the ultrasounds normally used in the process of ultrasonication is higher than 20kHz.

The main principle involved in the dispersion of particles by ultrasonication is the ultrasonic cavitation and the air bubbles formation by the applied ultrasounds (Figure 3.35). The ultrasound waves cause cycles of low pressures and high pressures in a liquid that is exposed to these sound waves. As a result of the pressure cycles, mechanical stress acts on the agglomerated particles and tries to overcome the forces between the particles causing their coalescence together. The sound cavitation creates very high speed liquid jets (approximately up to 1000 km/h) and the liquids are pressed at very high pressures between the individual particles in the agglomerates. On the other hand, the air bubbles keep on forming and collapsing as long as the ultra sound waves are applied. Also due to the high ultrasound energy some particles collide with the other particles or agglomerates at very high speed. As a result of these high pressure liquid jets, collapsing bubbles and the high speed collision of the particles, the agglomerated particles separate from each other and get dispersed in to the liquids. If the applied ultrasound energy is higher to good extent, even some particles can get reduced in their size as well (Ultrasonics 2014; Chemists 2014).

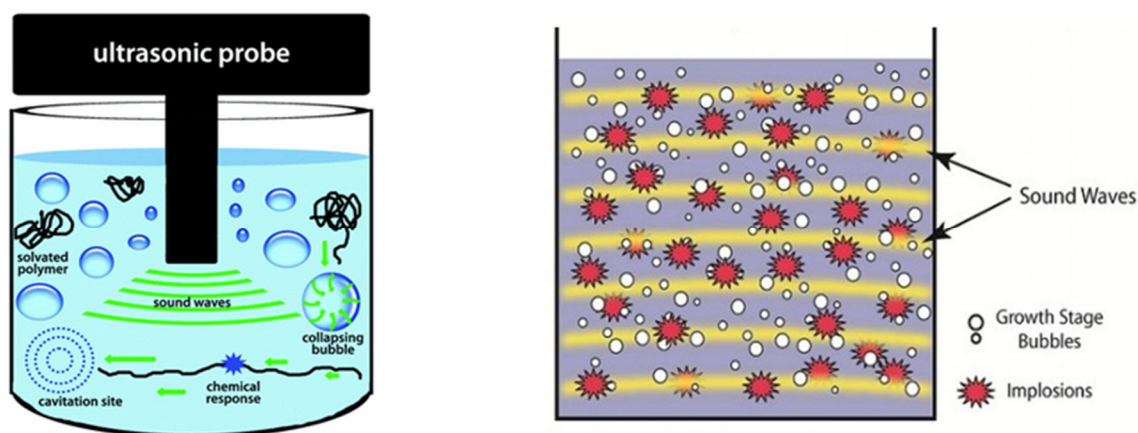


Figure 3.35: Cavitation bubbles formation and implosions leading to dispersion in an ultrasounds probe sonicator (left) and bath sonicator (right)

The size and dispersion quality of the carbon nanomaterials in the required solvent or liquid depends upon frequency and power of the sonicators. Normally if the probe sonicators are used at low power, more energetic cavitation bubbles are produced as a result of which better dispersion of the nano particle is obtained (Hilding et al. 2003)

There are many ways through which ultrasound waves can be applied for the said purpose but in this study, water bath sonication and probe sonication methods were used in order to disperse the carbon nanotubes, graphene nanoplatelets and graphene oxide particles in the respective deposition solutions. The bath sonicator (SONICA Ultrasonic cleaner by Soltec™) and the probe sonicator (SONICS®, Vibra-Cell VCX 750) are shown in the Figure 3.36.



Figure 3.36: Ultrasound probe sonicator (left) and ultrasound bath sonicator (right)

3.3.6.2 Mechanical magnetic stirring

A magnetic stirrer was used to mechanically disperse the carbon nanomaterials inside the deposition bath after they have been dispersed by probe and bath sonicators. The purpose was to further stabilize the dispersed phase. The magnetic stirring was continued during the process of deposition as well to ensure a homogeneous bath during the whole duration of the composite deposition.

Magnetic stirring uses simple equipment that stirs a magnetic bar placed inside the solution or liquid in which nanomaterials are to be dispersed. When the power is applied stirrer revolve at certain RPM speed that can be adjusted by a knob. A typical magnetic stirrer with the stirrer bars is shown in the Figure 3.37.



Figure 3.37: A typical magnetic stirrer

3.3.7 Thermal characterization

3.3.7.1 Differential thermal analysis

A differential thermal analysis (DTA) is a very common technique widely used in the thermal characterization of the samples. The working principle of the DTA technique is very simple. The sample under thermal observations is heated or cooled against an inert reference and the difference of temperatures (ΔT) between them is monitored (Figure 3.38). In this way, the changes in the thermal behavior of the sample can be obtained with respect to the reference sample (Haines 2002).

$$\Delta T = T_S - T_R \quad \text{Eq. 3.12}$$

In the above equation, T_S and T_R are the temperatures of the sample and reference respectively. This difference in temperature is plotted against the programmed temperature to obtain a thermogram of the shape as shown in the Figure 3.39. There can be two types of curves obtained from the data. If the difference in temperature ΔT is negative, a negative curve i.e. endothermic curve is obtained showing the decrease in the temperature of the sample with respect to the reference. This indicates an endothermic event for example melting. If the temperature difference of the sample and the reference is positive, an exothermic curve (positive curve) is obtained that shows an exothermic thermal change in the sample behavior, for example oxidation (Brown 2001).

In the study of nickel and silicon carbide fiber composite coatings deposited on the superalloy, DTA was used to study the chemical reactivity of the nickel matrix with the super alloy Inconel-718, with the SiC fibers and C or TiB₂ that are used normally as coatings on SiC fibers.

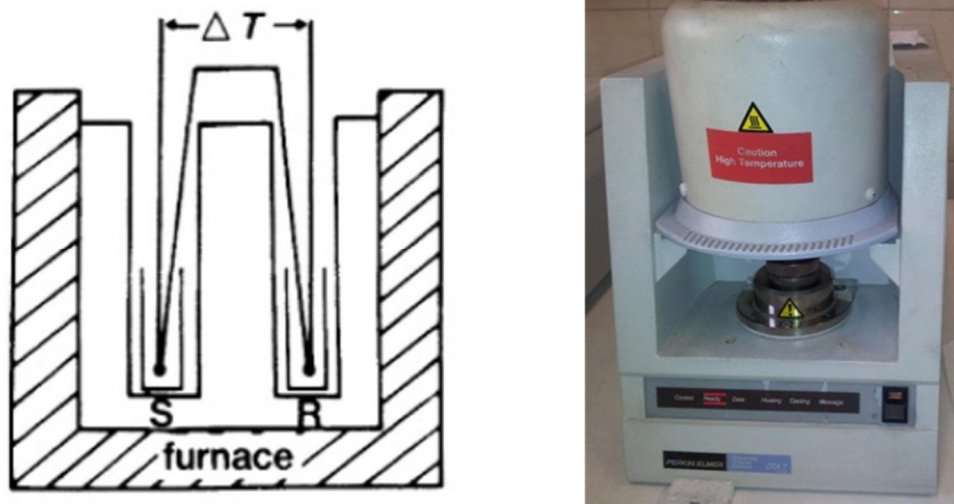


Figure 3.38: Schematic representation (left) and actual instrument (right) for the DTA technique; S=sample, R=reference (Brown 2001)

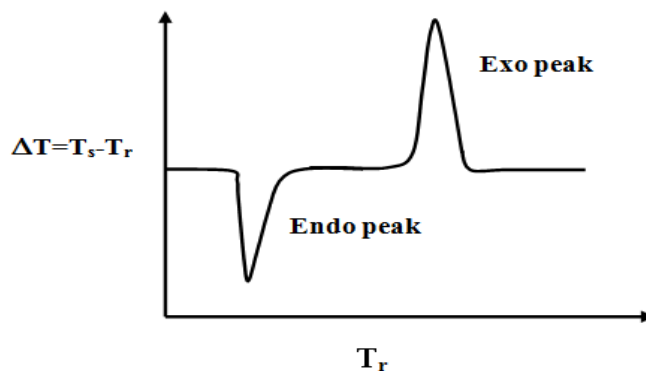


Figure 3.39: Thermogram obtained from DTA instrument

3.3.8 Tribological characterization

3.3.8.1 Pin-on-disk

Pin-on-disk refers to an instrument that is used to investigate sliding wear behavior of the materials. The pin-on-disk procedure is in very common use because it is fast, readily available and easy to conduct (Budinski 2009). From an engineering perspective, the

main reason for executing wear tests of the samples is to have an idea of the life of the sample up till when it can provide the predetermined reliable performance for the specific application (Bayer 2004). The values of co-efficient of friction can also be obtained. The basic working process of the instrument consists of sliding a pin against the disk of the materials to be tested. The disk specimen revolves at a prefixed speed for a predetermined period of time and distance. A variety of loads e.g 5 N, 10 N, 15 N can be used according to the type and hardness of the materials being tested. The main variables to be optimized before the tests are applied loads, revolving velocities or sliding speeds and diameters of the pin and radius of the wear track. A schematic representation and an actual set up of the pin-on-disk technique are shown in the Figure 3.40 and Figure 3.41.

In this thesis work, pin-on-disk facility was used to study the friction and wear behavior of carbon nanomaterials reinforced nickel matrix composite coatings deposited on a 24 mm diameter steel substrates. The optimized values of all the parameters (10 N load, 180 RPM, 20 mm track diameter and 20 minutes) were used. A WC/Co pin of 3 mm diameter was chosen for sliding against the sample's surface. The data obtained from the program of the instrument includes time, sliding distance and the co-efficient of friction. The weight or mass loss of the samples was calculated by weighing the specimens before and after the experiment and an idea of the wear rate of the sample can be obtained by plotting this mass loss against the time or the sliding distance. The volume loss of the material removed from the sample can be calculated either by dividing the already determined mass loss with the density or by using the well-known Archard's equation:

$$\text{Total volume loss} = Q = KWL/H \quad \text{Eq. 3.13}$$

Where K is the constant, W is the applied normal load, L is the total sliding distance and H is the hardness of the material (Contributors 2014).

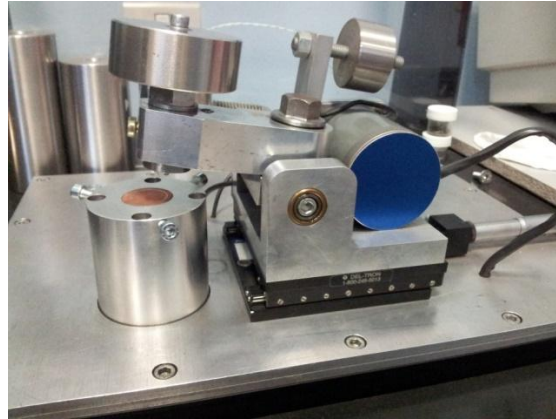


Figure 3.40: Pin-on-disk apparatus

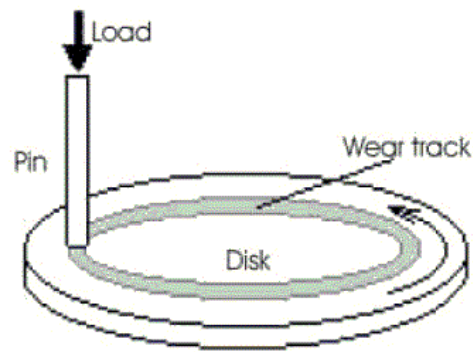


Figure 3.41: Schematic of pin-on-disk

Although pin-on-disk is a simple method for wear testing of the materials, it has certain disadvantages too. Among the major drawbacks of the pin-on-disk arrangement are: asymmetric sliding conditions, large differences in the contact zone areas of the pin and disk, unequal adsorption and different rates of wear of the disk and pin etc. (Gnecco 2015).

3.3.8.2 Roughness measurator and profilometer

As friction and wear are the surface properties so it is always important to observe the surfaces before and after the wear or friction tests. By analyzing the surface profiles, one gets an idea and some obvious details about the sample that what have happened with it. So it is recommended that the surface texture of the specimens must be recorded, at

least the roughness number (R_a). A cross-section of the real surface on most of the engineering materials is shown in the Figure 3.42.

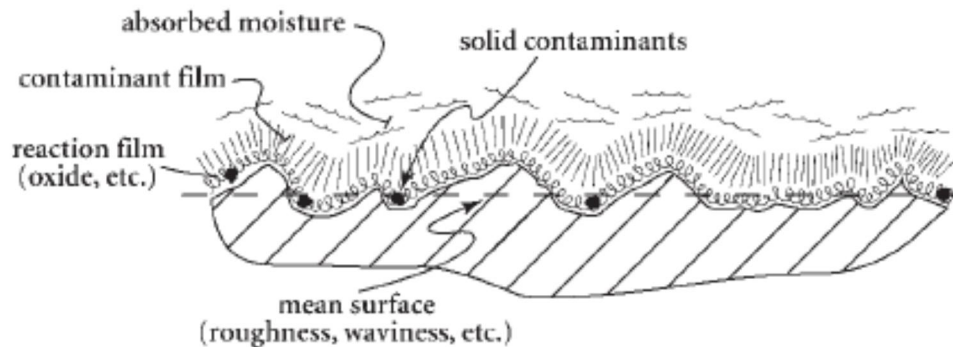


Figure 3.42: cross-section of a real surface on the materials (Budinski 2009)

Modern profilometers, available for the surface texture or roughness measurement purposes, use two types of probes; contact probes or noncontact probes. Some profilometers have both types of probes. A typical contact profilometer uses a conical diamond stylus with a 2- μm 90° tip radius. The forces applied through the tips during the surface scan range from 3 to 30 mg (Budinski 2009).

In this research work, the analysis of the surface roughness was done by using a surface profilometer “HOMMELWERKE T1000” that is shown in the Figure 3.43. The instrument records the roughness profile and also gives the average roughness number (R_a) in micrometers. This profilometer can also be used to measure the wear track area of the specimens after the pin on disk tests that helps further to evaluate the volume loss of the debris.



Figure 3.43: Surface profilometer used for roughness

Chapter 4 Results and Discussions

4.1 Ni-SiC long fibers composites

The reason for the preparation of the Ni-SiC long fibers composites derives from the need of stiffening the Inconel-718 alloy at high temperature. Thus, silicon carbide fibers were the best choice, since the silicon carbide has high stiffness at low temperature and in particular at high temperature. However, neither the nickel matrix nor the superalloy must react with silicon carbide at high temperature. Moreover, the layer of nickel must enclose the silicon carbide fibers, creating a strong link with the Inconel-718 support and also with the silicon carbide fibers, in order to allow the transfer of the stress from the Inconel718 to the nickel matrix to the silicon carbide fibers.

The chosen silicon carbide fibers were high modulus ones, and since strength and stiffness were required, monofilament fibers were deemed the best choice. High stiffness and high strength, coupled with high temperature performance, were the requirement and thus fibers with a hundred micrometers diameter were chosen. Since silicon carbide fibers can be produced with a carbon or carbon/titanium diboride coating, the best coating choice was also studied to optimize the chemical interaction.

The composites were then produced and characterized at room temperature and high temperature in order to understand their mechanical performance.

4.1.1 Optimization of electrodeposition parameters

The first step in the research was to study the electrodeposition process and its suitability to produce the Ni matrix composites with SiC long fibers. The parameters of electrodeposition, current density and deposition time were evaluated and optimized for the deposition of the composites. For this purpose trial Ni metal depositions were performed using different combinations of current density and the deposition time. The results of these investigations are summarized in the Figure 4.1 and Figure 4.2.

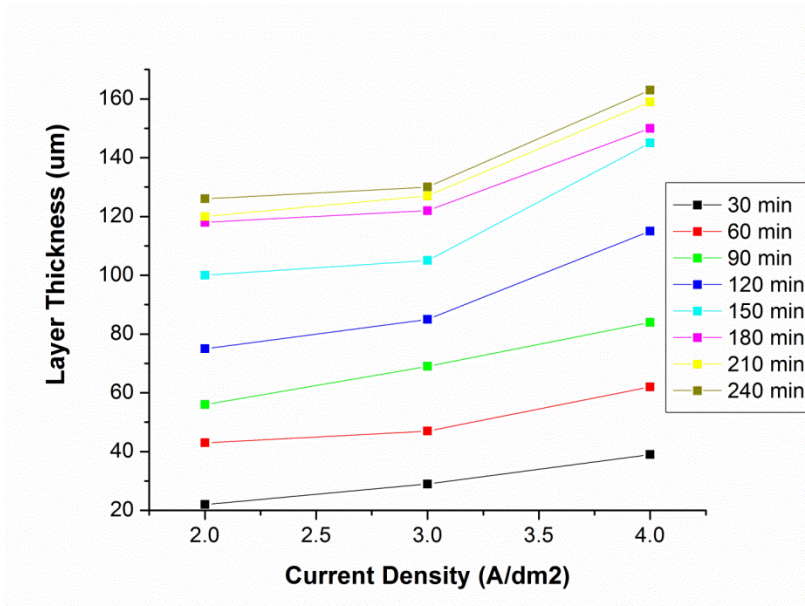


Figure 4.1: Layer thickness as a function of current density

The thickness of the nickel layer increases with increasing the deposition time as well as by increasing the current density which is in accordance with the already published literature (Sadiku-Agboola et al. 2011; OLORUNTOBA et al. 2011; Lee et al. 2013).

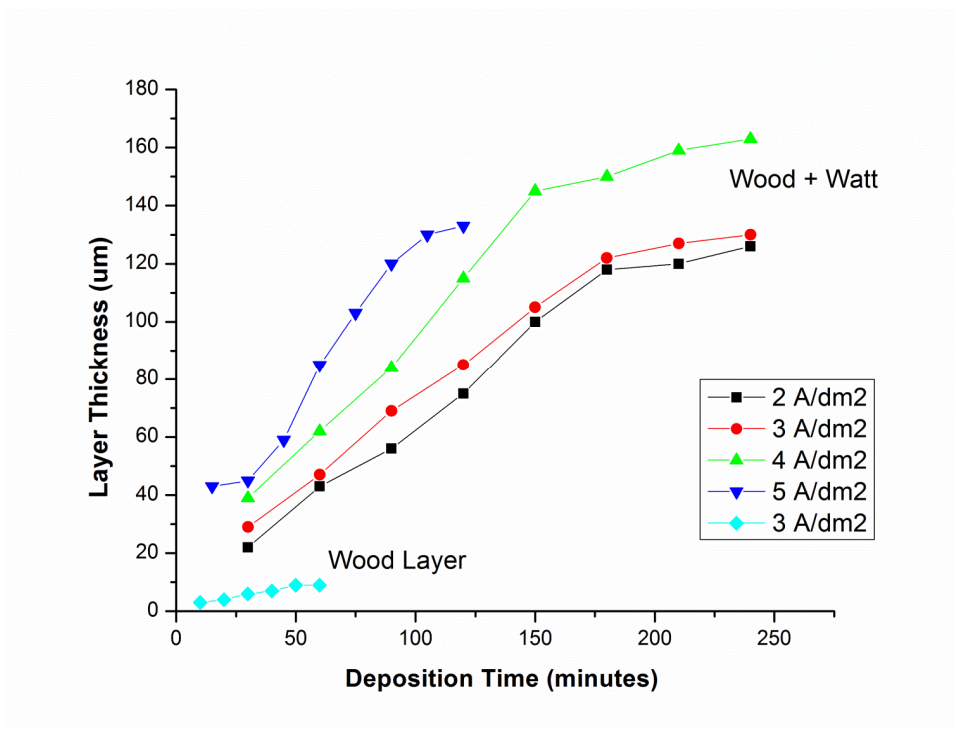


Figure 4.2: Effect of deposition time on the deposition thickness

This increase in the deposited layer thickness obeys a linear trend till 180 minutes of the deposition time in case of all current densities except for the 5 A/dm^2 . But after about three hours, the thickness increase is not linear with the time. Also if the current density is increased to values higher than 4 A/dm^2 , the quality of the deposit starts worsening due to an increase in the evolution of the hydrogen gas at the cathode surface causing porous and brittle deposits (Figure 4.3).

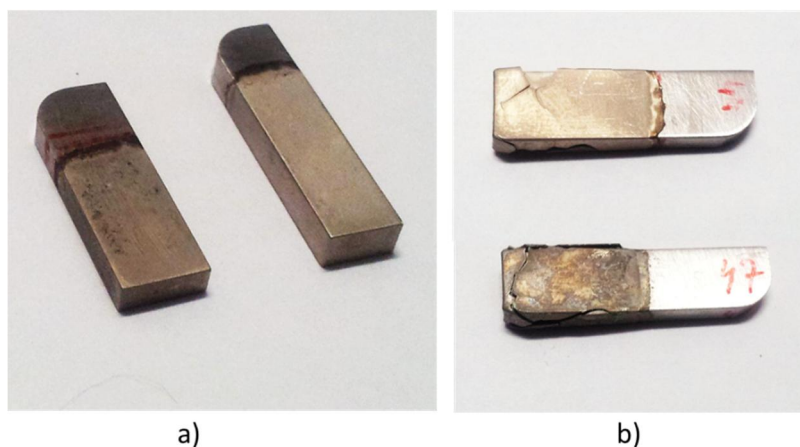


Figure 4.3: Nickel layers electrodeposited on Inconel-718 substrates at; (a) 2 A/dm^2 and, (b) 5 A/dm^2

As the silicon fibers used were of $106 \mu\text{m}$ diameter, a current density of 2 A/dm^2 and a deposition time of 4 hours were chosen for the final experiments because these conditions ensure the deposition of a sufficient thickness (approximately $120 \mu\text{m}$) of the nickel matrix in order to completely embed the whole diameter of the fiber.

4.1.2 Feasibility of producing composites

In addition to the optimization of the electrodeposition parameters, chemical feasibility of depositing the Ni/SiC_r composites on nickel super alloy Inconel-718 was also studied to choose the best type of fiber. In particular the reactivity between the components of the Inconel718 and the SiC fibers or their coatings was studied. For this study two routes were followed. The first was to take into account theoretical considerations and the second route was to use DTA and XRD measurements to verify theoretical calculations.

4.1.2.1 Theoretical considerations

In order to verify the chemical compatibility between the Inconel 718 superalloy and the SiC fibers, two different studies were carried out: the analysis of the binary phase diagrams of the elements that can react, and thermodynamic calculations to determine the stability of phases at various temperatures. The study considered the main constituents of Inconel 718 (Ni, Fe, Cr), silicon carbide (SiC) and the compounds that can be present on the surface of the silicon carbide fiber as coating, i.e. carbon (C) or titanium diboride (TiB₂).

The phase diagrams for all the possible combination between the main elements in the superalloy and Si, C, Ti and B were considered. Several possible reactions were taken into account between the main superalloy elements and the SiC reinforcement, both in the coated or uncoated state. In order to choose the most probable, thermodynamical calculations (Barin & Platzki 1995) were performed between 25 and 1000 °C and the reaction with the lowest ΔG for each couple of compounds is presented in Table 4.1 for 25 °C and 525 °C. The intermediate phases that can be stable in this temperature range are also shown.

Table 4.1: Possible reactions between components of superalloy and fibers, with stable intermediate phases and calculated ΔG at 25°C and 525 °C

| Reaction | Stable intermediate phases | ΔG at 25 °C [kJ/mol] | ΔG at 525 °C [kJ/mol] | $\Delta G < 0$ |
|---|---|------------------------------|-------------------------------|----------------|
| $\text{Ni} + \text{SiC} \rightarrow \text{NiSi} + \text{C}$ | NiSi, NiSi ₂ | -14.0 | -16.3 | yes |
| $3 \text{Ni} + \text{C} \rightarrow \text{Ni}_3\text{C}$ | - | +64.2 | +56.1 | no |
| $5 \text{Ni} + \text{TiB}_2 \rightarrow \text{Ni}_3\text{Ti} + 2 \text{NiB}$ | Ni ₃ B, Ni ₂ B, Ni ₄ B ₃ , NiB, Ti ₂ Ni, TiNi, TiNi ₃ | -12.1 | -1.9 | < 600 °C |
| $9 \text{Cr} + 2 \text{SiC} \rightarrow 2 \text{Cr}_3\text{Si} + \text{Cr}_3\text{C}_2$ | Cr ₃ Si, Cr ₅ Si ₃ , CrSi, CrSi ₂ | -218.8 | -229.2 | yes |
| $3 \text{Cr} + \text{C} \rightarrow \text{Cr}_3\text{C}_2$ | Cr ₂₃ C ₈ , Cr ₇ C ₃ , Cr ₃ C ₂ | -86.3 | -92.0 | yes |
| $2 \text{Cr} + \text{TiB}_2 \rightarrow \text{Ti} + 2 \text{CrB}$ | TiCr ₂ , Cr ₂ B, Cr ₅ B ₃ , CrB, Cr ₃ B ₄ , CrB ₂ , CrB ₄ | +165.6 | +151.4 | no |
| $\text{Fe} + \text{SiC} \rightarrow \text{FeSi} + \text{C}$ | FeSi, FeSi ₂ | -7.6 | -10.2 | yes |
| $5 \text{Fe} + \text{TiB}_2 \rightarrow \text{FeTi} + 2 \text{Fe}_2\text{B}$ | TiFe, TiFe ₂ , Fe ₂ B, FeB | +140.6 | +137.5 | no |
| $3 \text{Fe} + \text{C} \rightarrow \text{Fe}_3\text{C}$ | Fe ₃ C | +20.0 | +2.5 | > 600 °C |

From the observation of the phase diagrams, only the Ni-C system does not contain intermediate phases. From the thermodynamical calculations results it is possible to observe that: (i) the reaction with the uncoated fibers is thermodynamically favored for all the elements (Ni, Cr, Fe) considered at any temperature; (ii) the reaction with carbon (therefore with the SiC fiber coated with C) is thermodynamically favored for Cr at any temperature, for Fe at $T > 600$ °C and is always impossible for Ni; (iii) the reaction with TiB₂ (therefore with the SiC fibers coated with C and then with TiB₂) is difficult to evaluate due to lack of literature data about titanides and silicides. However, the reaction seems to be favored only with Ni at $T < 600\text{-}700$ °C.

A particular mention must be given to Fe_3C compound. Even if it is generally accepted in the scientific community that Fe_3C is a metastable phase (Sinha 2003), thermodynamical data confirm this assumption only up to 600-750 °C. Data by Barin and Platzki (Barin & Platzki 1995) suggest that roughly over 600 °C the Gibbs energy of formation is lower than 0. This is not very different from the very recent calculations by Hallstedt et al (Hallstedt et al. 2010). By contrast, Chipman (Chipman 1972) proposes 750 °C as the temperature at which ΔG becomes negative. In our calculations we decided to consider the phase stable over 600 °C but to verify experimentally if this formation occurs after a DTA course up to 1450 °C.

4.1.2.2 DTA and XRD measurements

To confirm calculations, DTA experiments were conducted on systems consisting of Ni, Fe or Cr, and C, SiC or TiB_2 . DTA measurements were performed on three different samples for every reaction, in a temperature range of 30-1450 °C.

The DTA curves for the mixtures of nickel with C, SiC and TiB_2 are presented in Figure 4.4. It is evident that nickel does not react with carbon and the only endothermic peak observed perfectly corresponds to the melting temperature of the Ni-C eutectic. On the other hand, a heavy reaction is already present with SiC at lower temperatures, with exothermic peaks at 730, 1100, and 1140 °C. Two endothermic peaks are also observed, at 1180 and 1280 °C, corresponding to different eutectics in the Ni-Si phase diagram.

X-ray diffraction was used in order to recognize the reactions occurred during the DTA experiments. In the system Ni+C (Figure 4.5a), XRD confirmed that no reaction occurs, even after the eutectic formation. On the contrary, in the system Ni+SiC (Figure 4.5b) many phases are observed: δ -Ni₂Si, C, residual SiC, and traces of other nickel silicates: β 1-Ni₃Si, γ -Ni₃₁Si₁₂ and ϵ -Ni₃Si₂. This suggests that the endothermic peaks observed in the DTA are due to the β 1+ β 2 eutectic and to the γ + δ eutectic respectively.

A small reaction is also observed between nickel and TiB_2 . Even if DTA curves do not show important reaction peaks, two small endothermic peaks are observed at 1070 and 1130 °C. XRD analysis shows the formation of a small nickel boride quantity, suggesting that the two melting peaks on the DTA are due to the Ni+Ni₃B and Ni₃B+Ni₂B eutectics.

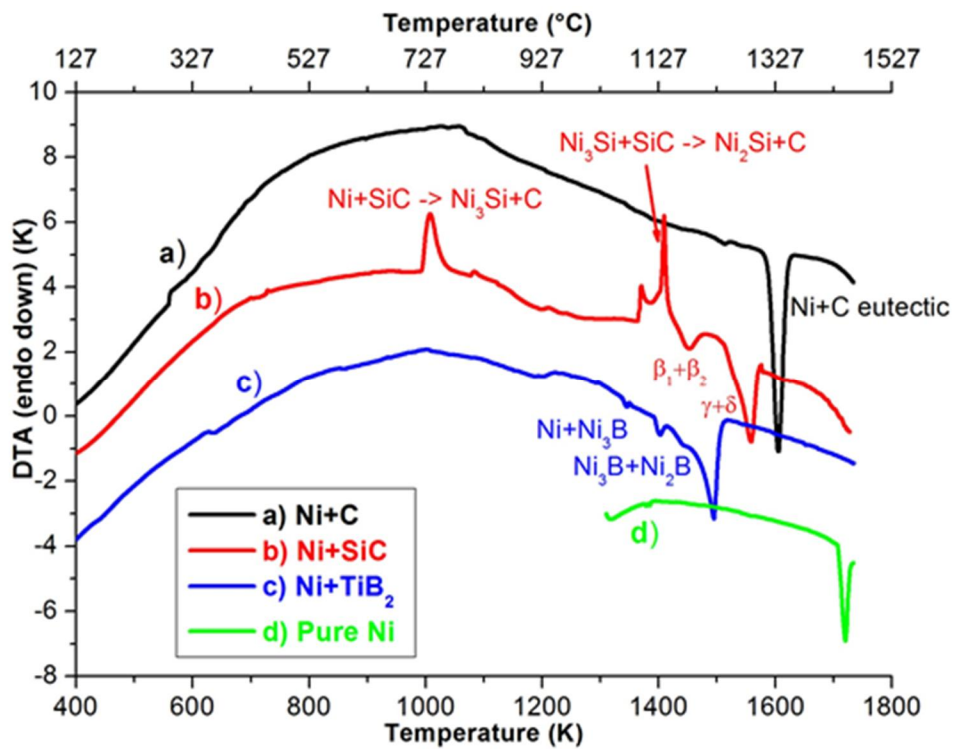


Figure 4.4: DTA curves for the systems (a) Ni + C; (b) Ni + SiC; (c) Ni + TiB₂; (d) pure Ni.

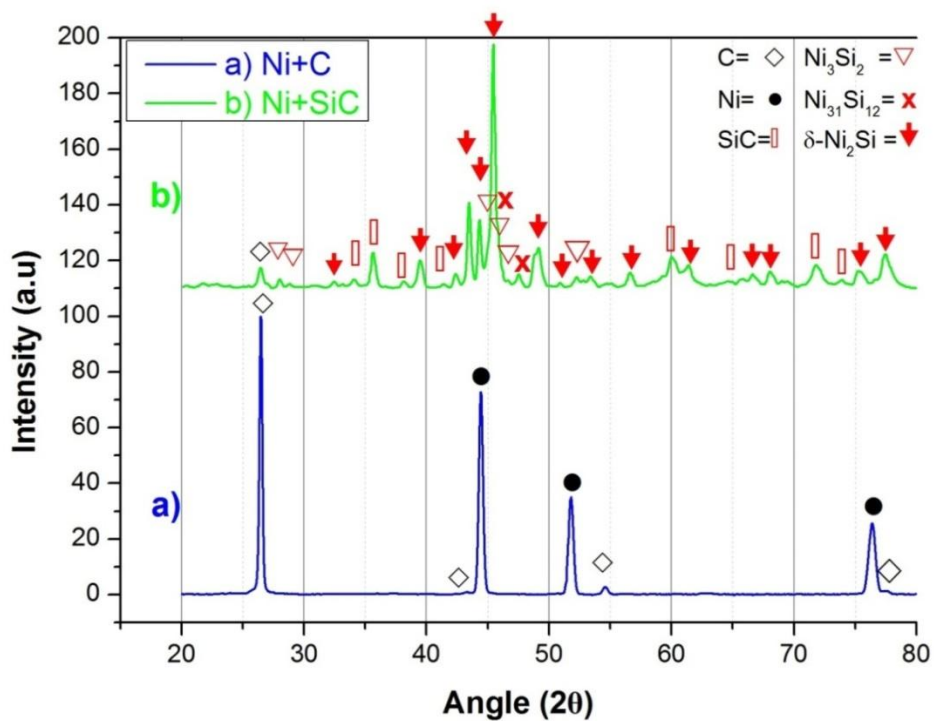


Figure 4.5: XRD patterns of (a) Ni/C and (b) Ni/SiC mixtures

The DTA curves for the mixtures of carbon with Fe, Ni and Cr are presented in Figure 4.6. No evident exothermic peak is observed before the eutectic between iron and carbon or nickel and carbon. No melting at all is observed in the Cr-C system, since the eutectic temperature is close to 1500 °C, which is higher than the maximum DTA temperature. However, XRD measurements show that a very small quantity of chromium carbide is formed after the DTA course, while no iron carbide is observed. It appears that kinetic aspects prevail, even with thermodynamically favored reactions, so that no thermal signal is observed.

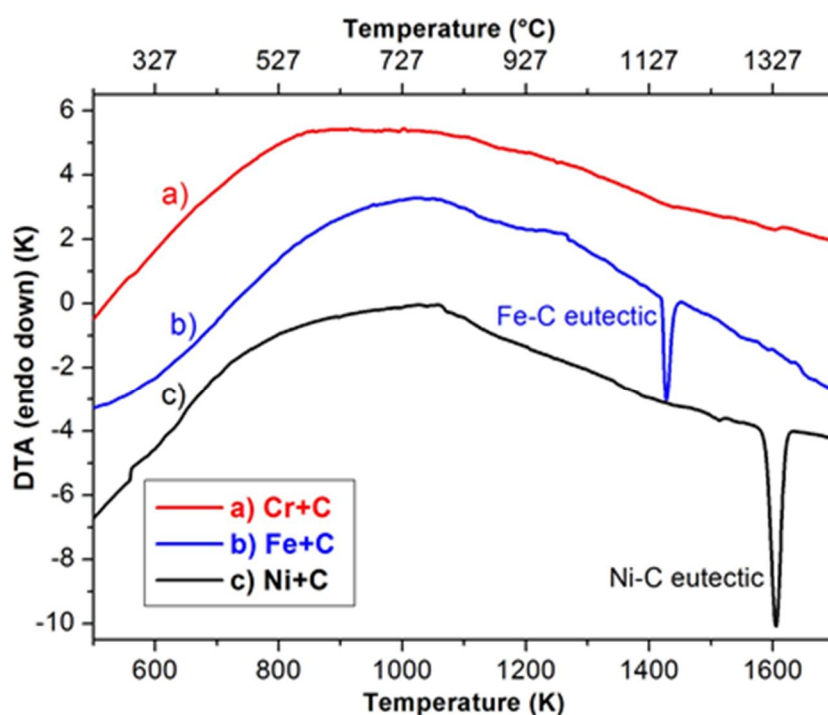


Figure 4.6: DTA curves for the systems (a) Cr + C; (b) Fe + C; (c) Ni + C

Finally, DTA and XRD measurements were performed on mixtures of Inconel 718 with SiC, C and TiB₂. The results are in accordance with the previous ones, i.e. the superalloy reacts with all kind of SiC reinforcements, both coated and uncoated.

Since nickel is the most present element in the superalloy, and it is not reactive with carbon, the calculations confirm that the best choice envisaged for the composite is nickel as the electrodeposited matrix and carbon-coated silicon carbide fibers as

reinforcement. However, it seems necessary to separate the fibers and the superalloy with a buffer layer of nickel, in order to avoid possible reactions at high temperature due the diffusion of alloying elements up to the fiber.

4.1.3 Study of interfaces

In the metal matrix composites, interface is a very important entity because the load is transferred from the matrix to the fibers through this interface. If the interface is not so good, there will not be an effective transfer of the load from the matrix to the fibers and as a result the composite will fail at a lower stress. In case of the composites prepared in this study, there are two kinds of interfaces needing to be taken care of: the interface between nickel matrix and silicon carbide fibers, and the interface between Ni/SiC composite and Inconel-718 substrate.

4.1.3.1 Ni-SiC fiber interface

The interface between SiC fibers and the electrodeposited nickel matrix is very important to consider. It was noticed that this interface depends upon the electrodeposition parameters especially on the deposition current density. At higher current densities the interface obtained is not so good and well adherent because the hydrogen gas evolution at the cathode is higher at higher current densities. In Figure 4.7 are shown the micrographs depicting the quality of interface observed under optical microscope and scanning electron microscope. The interface between SiC fiber and the nickel matrix was obtained by using current density of 5 A/dm² for the electrodeposition.

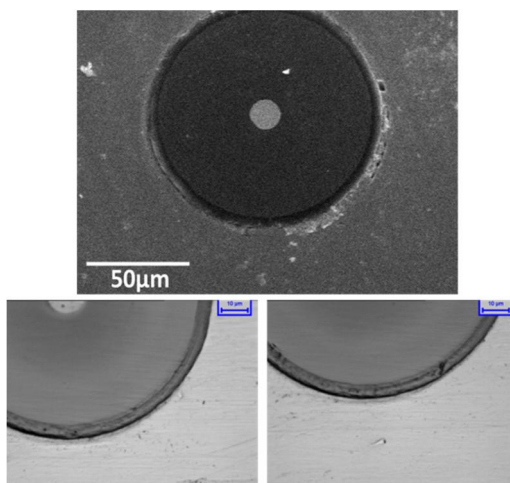


Figure 4.7: Interface between Ni matrix and SiC fiber without treatment

This interface can be further improved by hot pressing the composites. Hot pressing would induce the residual compressive forces at lower temperatures which help good interface between Ni matrix and SiC fibers. So it was tried to do uniaxial pressing at 600 °C for 24 hours in an argon inert atmosphere. As a result there was noticeable improvement observed in the quality of interface as shown in the Figure 4.8.

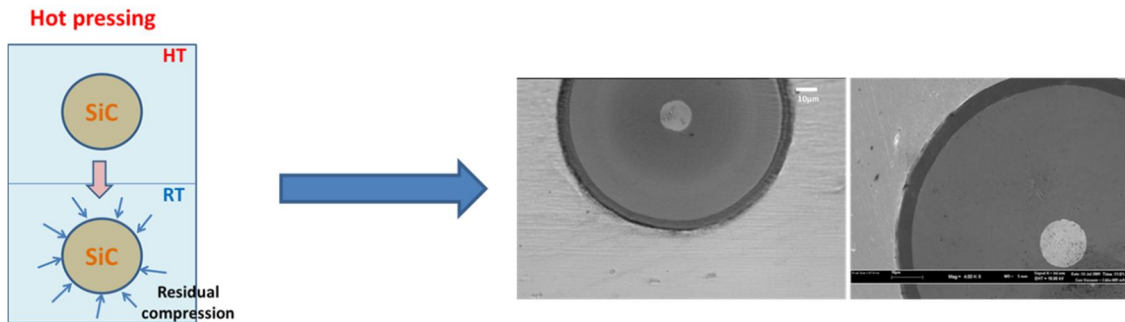


Figure 4.8: Interface between Ni and SiC after hot pressing at 600 °C for 24 hours

4.1.3.2 Ni-SiC/Inconel-718 interface

This interface is basically the interface between the substrate Inconel-718 and the nickel metal deposited as the matrix all around the SiC fibers arranged on the Inconel-718 substrate. So in this case SiC fibers do not come in direct contact with the substrate and the interface remains solely between electrodeposited nickel layer and the substrate. Here again the produced composites were uniaxially pressed at 600 °C for a period of 24 hours in the argon inert atmosphere in order to see its effect on the interface.

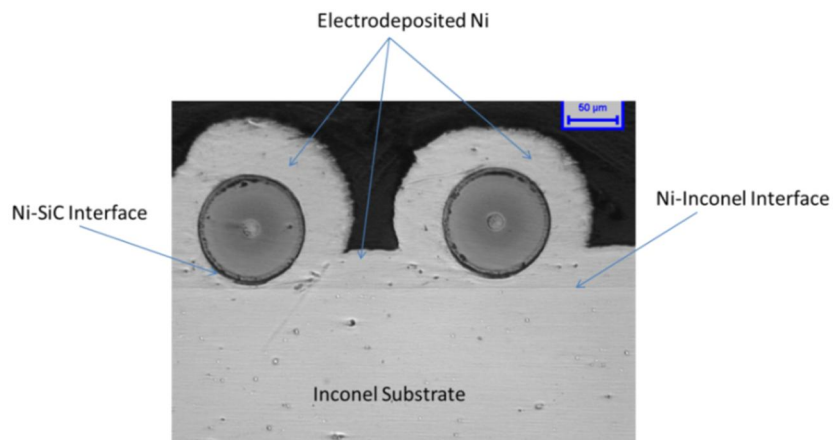


Figure 4.9: Ni/SiC composite deposited on /inconel-718 substrate

Figure 4.9 shows the electrodeposited Ni-SiC composite on the Inconel-718 substrate. The interface Ni/Inconel-718 is clearly visible since a demarcation line appears. On the as-deposited composite the interface is not of extremely good quality; when the specimens are hot pressed, instead, the quality of the Ni/Inconel-718 interface gets improved as shown in the Figure 4.10.

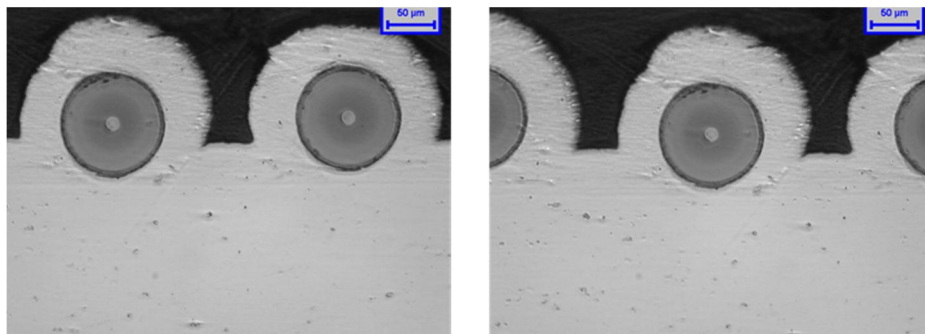


Figure 4.10: Composites after hot pressing at 600 °C for 24 hours

In addition to hot pressing, another step can also be introduced that favors in getting better interfaces. This step involves depositing a very thin intermediate layer of nickel from a Wood type bath for 10 minutes before proceeding to the final deposition by the Watt's bath. This intermediate layer deposited between the substrate and the nickel Watt's layer is acidic and aggressive in nature and causes a strong interface bond (Figure 4.11) so that the interface quality is greatly improved.

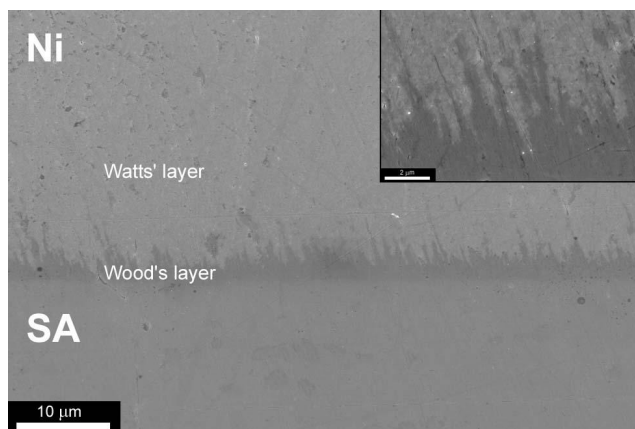


Figure 4.11: Quality of Interface between Ni and super alloy support with intermediate Wood's layer

4.1.4 Production of the composites

After evaluating the electrodeposition parameters, the chemical reactivity and the quality of interfaces, the final composites were produced by using all the optimized parameters. All the nickel Watt layer depositions were done using current density of 2 A/dm^2 for 4 hours. The Wood's layer deposition was also done at current density of 2 A/dm^2 but for a duration of 10 minutes. Before the SiC fibers arrangement on the substrates and the nickel depositions, the substrate is first electrochemically cleaned at 2 A/dm^2 current density in a sodium hydroxide bath. Two types of composites are produced on the superalloy support; one with 30 fibers per cm and the other with 40 fibers per cm on each side of the support. In Figure 4.12a and Figure 4.12b, the cross sections of the produced composites observed under the scanning electron microscope are shown.

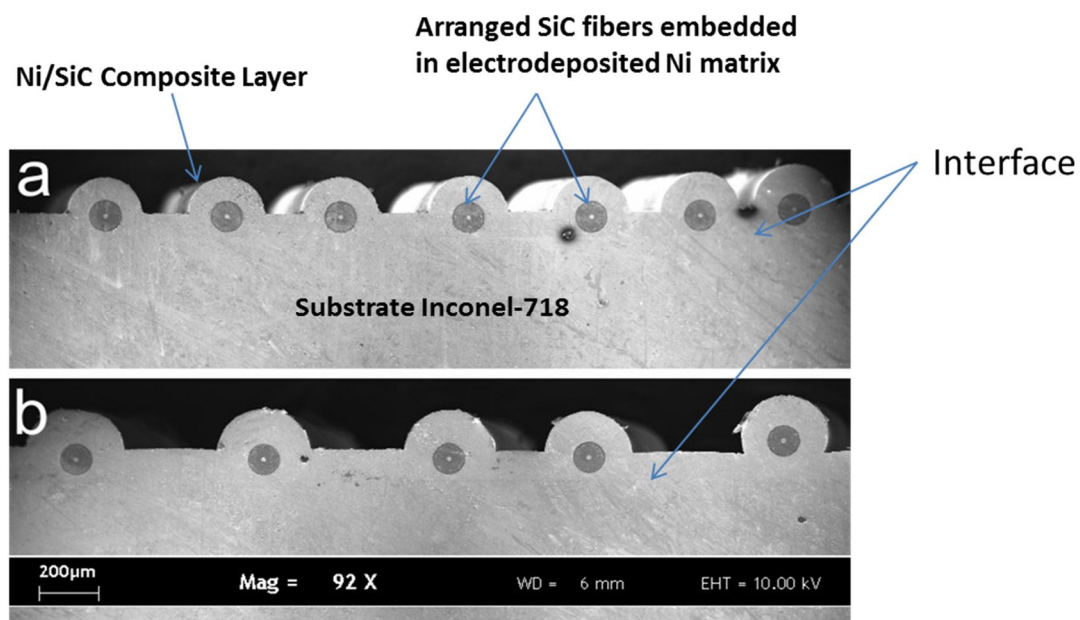


Figure 4.12: Typical sections of the Ni/SiC composite layers on Inconel 718: (a) sample with 40 fibers/cm (b) sample with 30 fibers/cm

4.1.5 Mechanical properties

The tensile mechanical tests were performed on the final prepared composite specimens to evaluate their mechanical properties. The specimens were tested at three temperatures; 1) at room temperature, 2) at $400 \text{ }^\circ\text{C}$ and 3) at $600 \text{ }^\circ\text{C}$ to evaluate the

yield strength values at each temperature. The mechanical behavior exhibited by the composites under tension loads at 25 °C, 400 °C and 600 °C is shown by the stress strain curves in Figure 4.13, Figure 4.14 and Figure 4.15 respectively.

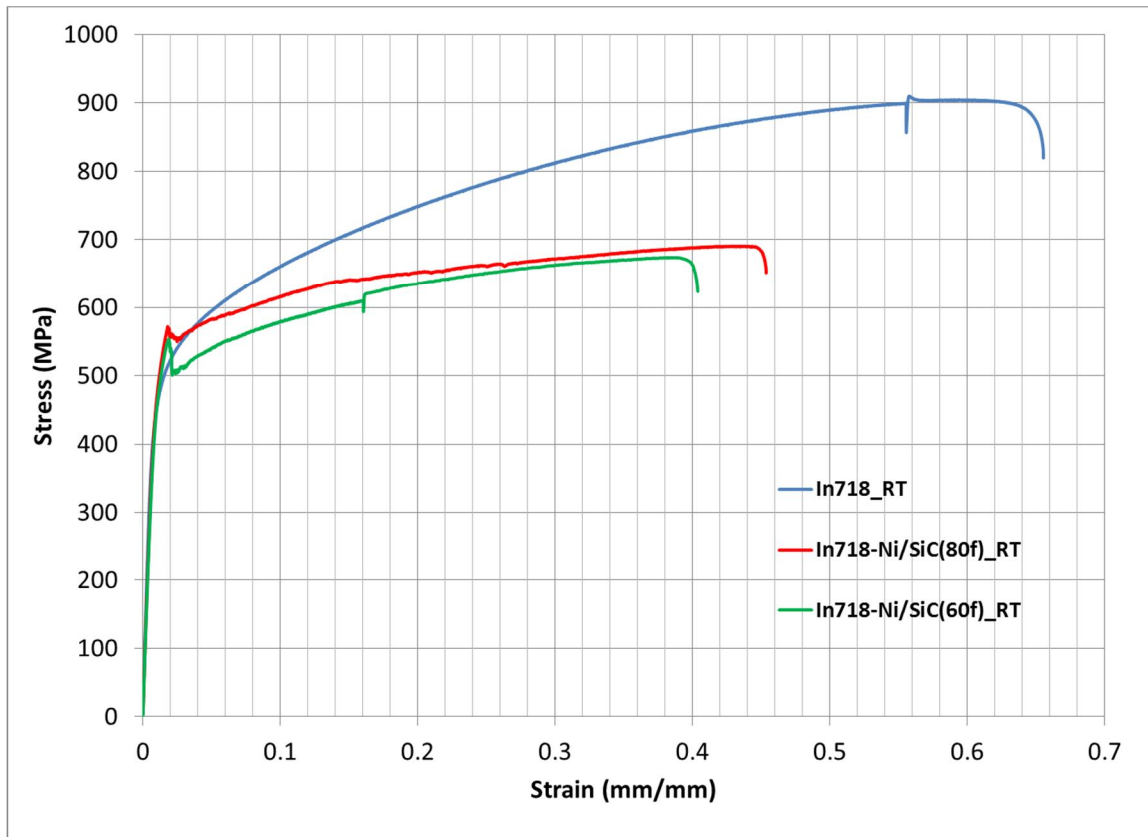


Figure 4.13: Stress vs strain curve for the materials at room temperature

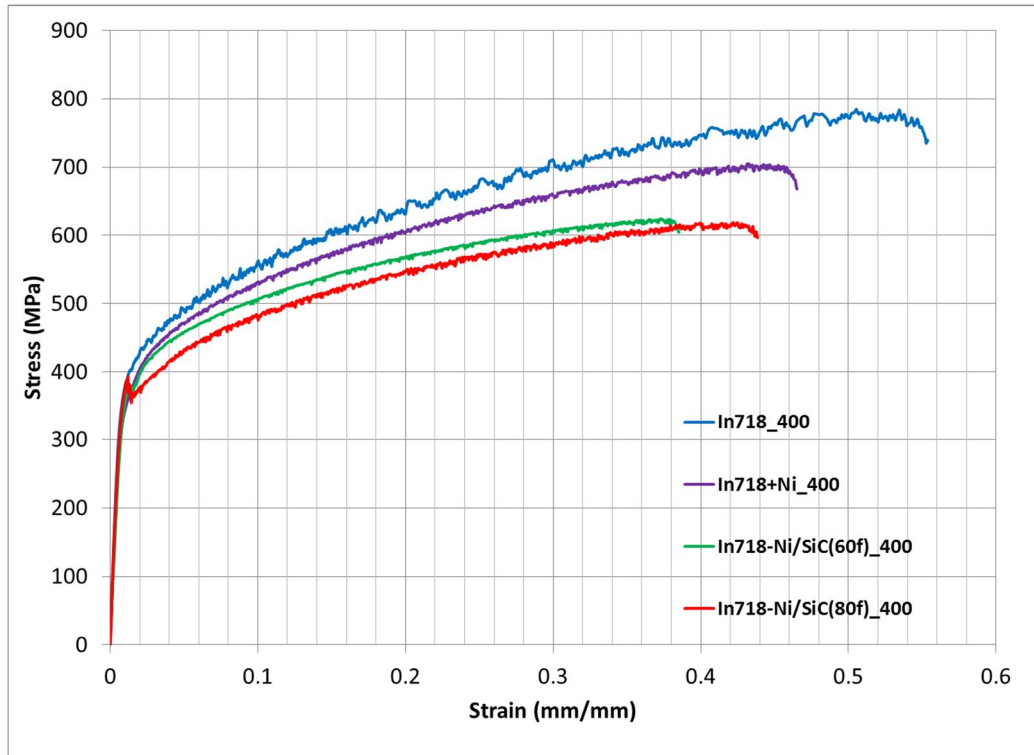


Figure 4.14: Stress vs strain curve for the materials at 400 °C

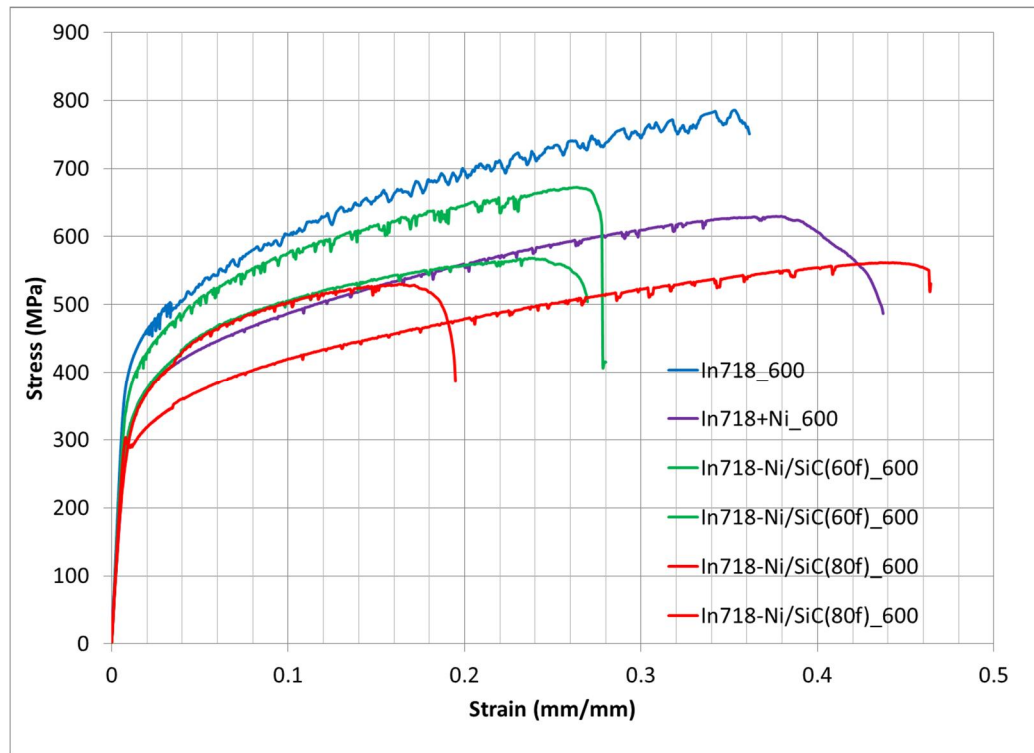


Figure 4.15: Stress vs strain curve for the materials at 600 °C

From the figures it can be seen that when the composites are loaded under tensile testing conditions, elastic deformation occurs in the whole material system but most of the load is carried by the SiC fibers. In the elastic region the three components (Ni matrix, SiC fibers and Inconel-718) deform elastically and with the same amount of strain. Since SiC fibers have the highest elastic modulus, they sustain a higher stress than the other two components. However, because the SiC fibers are ceramic and brittle in nature, so a point arrives when the value of applied load exceeds the strength of the fibers, so that the fibers start to fail because they do not have ability to undergo plastic deformation. When the applied load is further increased, the debonding of the broken fibers from the nickel matrix takes place. The fibers breaking and the debonding correspond to a drop in the overall load experienced by the specimen because fibers are less or no more contributing for the resistance to the applied load. In this region, the nickel matrix and the superalloy substrate start deforming plastically. With the further proceeding of the applied load in the tension test, the broken and debonded fibers are finally pulled out of the nickel matrix while substrate continues its plastic deformation till the point of fracture. It was observed by visual examination of the samples after the test that when the fibers are broken, debonded and pulled out from the nickel matrix, the broken parts of the Ni/SiC composites (which are now single fibers coated with the nickel other than the pulled out portion of the fiber) detach from the substrate surface leaving troughs on the thin layer of deposited nickel still present on the substrate (Figure 4.19a,c,d) The yield strength of the composites was calculated from the stress strain curves. The values obtained at all the considered temperatures are given in the Table 4.2 and are represented graphically in Figure 4.16.

Table 4.2: Stiffness of the material systems at different temperatures

| Material System | Yield Strength (MPa) | | |
|------------------------------------|----------------------|-------|-------|
| | 25°C | 400°C | 600°C |
| Inconel-718 | 420 | 355 | 380 |
| Inconel-718 + Ni | - | 320 | 300 |
| Inconel-718 + Ni/SiC (60fibers) | 450 | 335 | 330 |
| Inconel-718 + Ni/SiC (80fibers) | 450 | 330 | 285 |

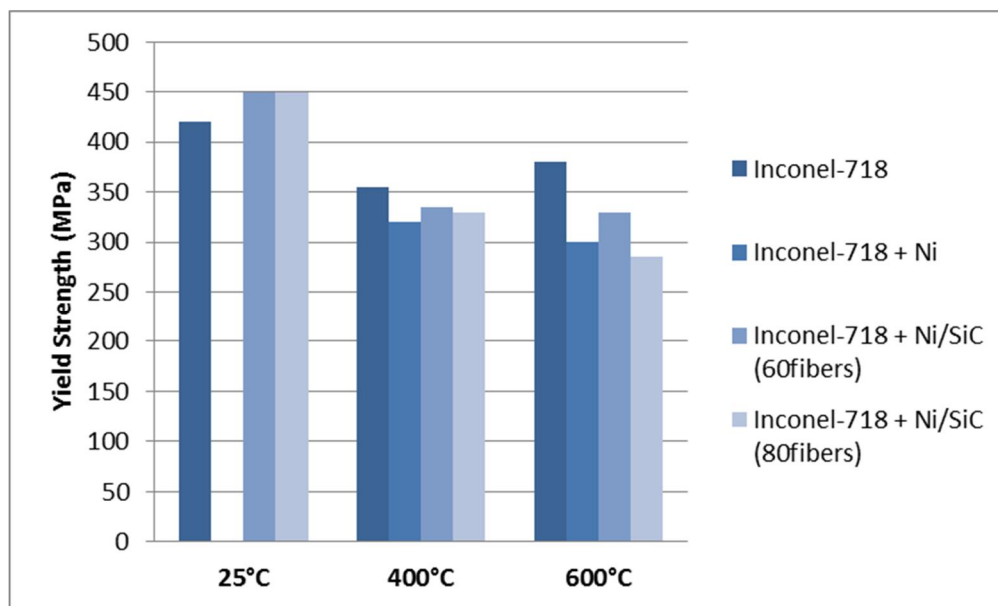


Figure 4.16: Comparison of yield strength for the produced composites at various temperatures

From the yield strength results, it is obvious that the superalloy substrates with Ni/SiC fibers deposited on them show higher values of strength as compared to the superalloy alone at room temperature. This increase in the yield strength is believed to be contributed by the electrodeposited Ni/SiC composite on the superalloy substrate. However there is a decreasing trend observed in the values of the yield strength when

the specimens are tested at higher temperatures. This is probably due to the reason that the interface between nickel and SiC fibers is weak at higher temperatures. Due to higher thermal expansion of nickel with respect to SiC, the interface yields at higher temperatures which is the main reason of decreased yield strength values.

However, this problem of weak interface can possibly be solved by hot pressing the specimens. After hot pressing, there will be residual compression stresses on the fibers when material comes at lower temperature (Figure 4.8). These residual compression stresses are not harmful rather they would increase the interface quality and strength.

4.1.6 Fracture behavior

The mechanically tested samples at room temperature as well as at higher temperatures were examined under the scanning electron microscope in order to study the fractured surfaces and understand the failure mechanisms. As Ni/SiC fibers composite is deposited on the Inconel-718 substrate, so there are three main things important to observe in the microstructures. First thing is the fracture mechanism in the Ni/SiC composite layer deposited on the Inconel, second the fracture mechanism at the interface of Ni/SiC composite layer and superalloy substrate and; the third and last one is the fracture behavior of Inconel-718 itself.

The elastic and plastic behaviors of the composite layer plus the Inconel-718 are already discussed with the help of the load-displacement curves in the previous section. In this section the fractures surfaces of the specimens are presented.

The fractographs presented in the Figure 4.17, are obtained from the samples tested at room temperature. From the micrographs, the fibers breaking, debonding and pull out phenomena are visible. The fibers broken in the tensile test were detached from the superalloy support, and were gathered and glued together vertically by a conductive adhesive tape in order to make it possible to observe the cross sectional views under the scanning electron microscope. In Figure 4.17 a) we see pulled out fibers whereas in Figure 4.17 b) are shown the holes in the nickel, indicating that fibers have been pulled out, after breaking and debonding during the test. Also there are signs of plastic deformation on these holes mouths, causing the striction at their upper ends.

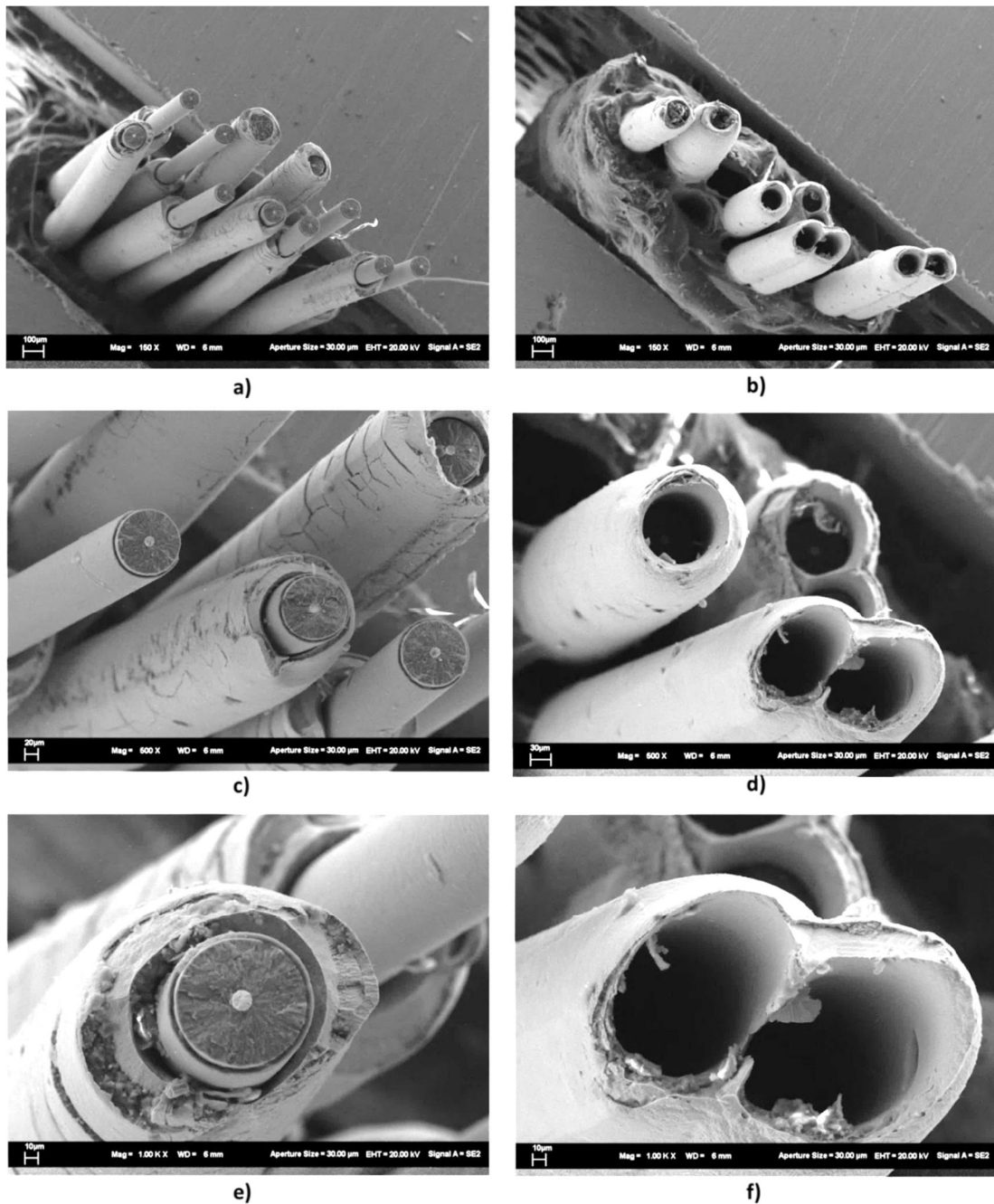


Figure 4.17: SEM images of fractured surface of Ni/SiC composites after tension test at room temperature. Images a), b) are taken at 150X; c), d) at 500X and e), f) at 1000X magnifications.

In order to better understand the mechanism of the fracture, a schematic of the fiber's breaking in the matrix, debonding and pull out phenomena is shown in the Figure 4.18.

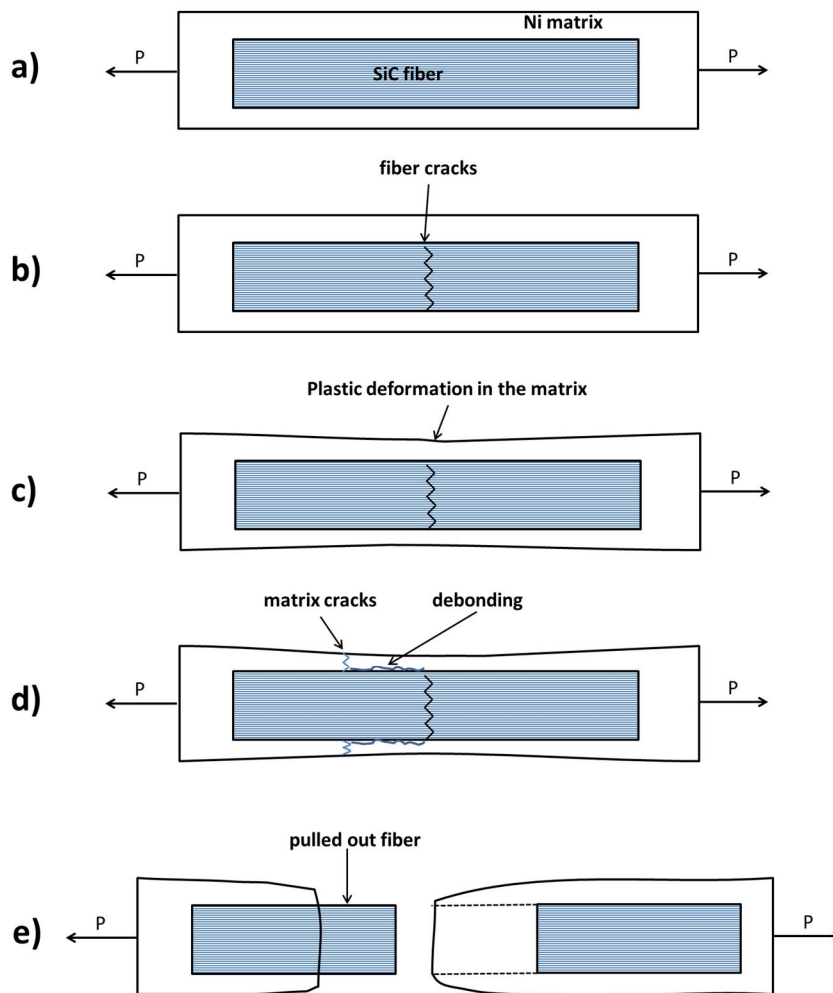


Figure 4.18: Schematic of the fracture mechanism in the Ni/SiC composites

Figure 4.19 shows the fractographs explaining the fracture of Inconel-718 during the mechanical tests. Figure 4.19 a) and Figure 4.19 b) represent, with different angles, some part of the lateral surfaces and some part of the cross-section of Inconel-718 substrate after the breakage in tensile test at room temperature. The lateral surface clearly shows the occurrence of plastic deformation and development of the micro cracks in the nickel matrix and also the regions of crests and troughs on the lateral surface of substrate. Troughs are the regions where SiC fibers were aligned before their fracture and debonding from the nickel matrix hence from the substrate. Fractographs c), d) in the Figure 4.19 c) and d) show magnified view of the crests and troughs.

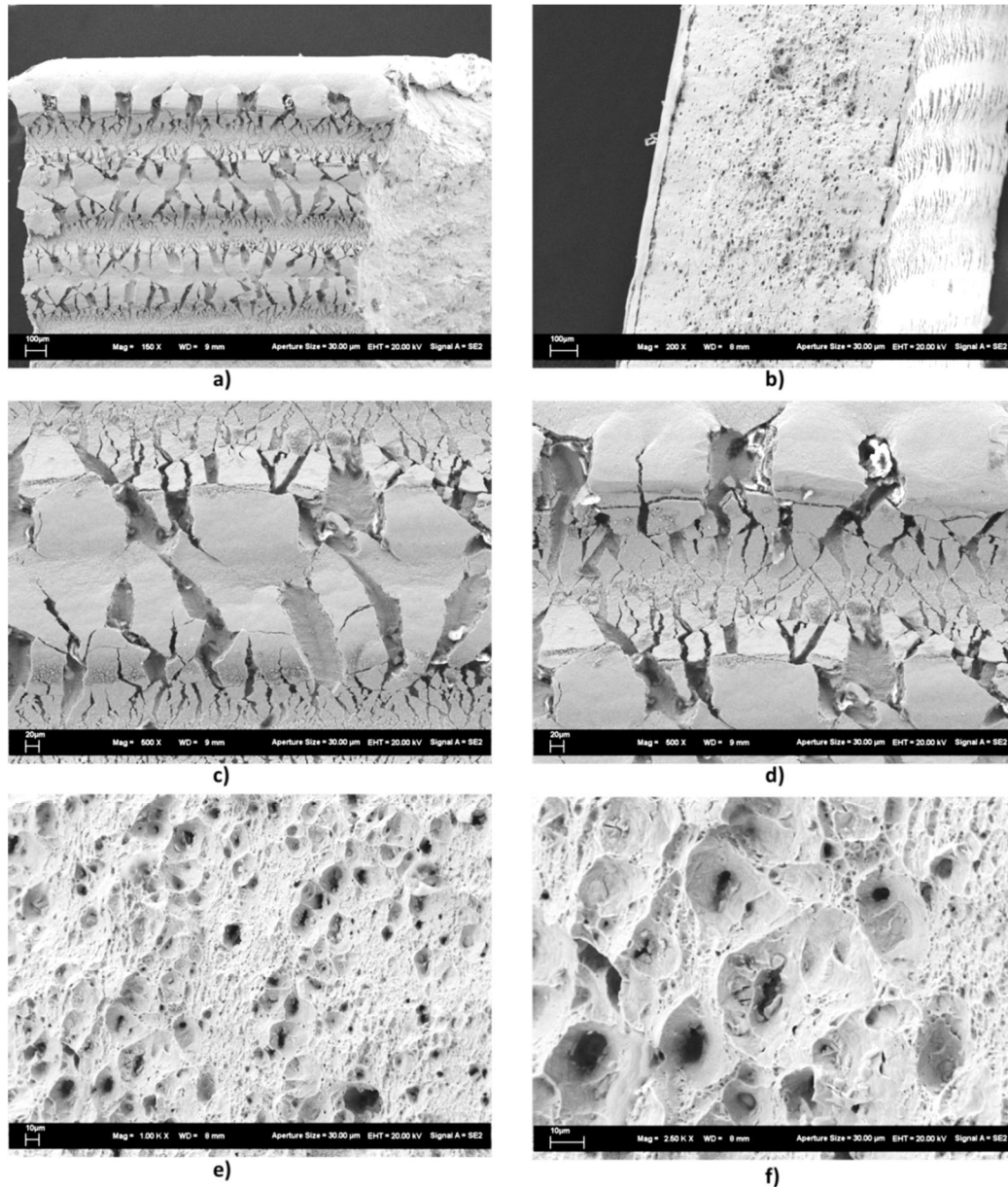


Figure 4.19: SEM fractographs of Inconel-718 at after tension test at room temperature.

The Inconel substrate fractures at the end when Ni/SiC composite deposited on it has already failed. As Inconel-718 is a metallic alloy having nickel metal as the major element in the composition, so the fracture follows almost the same fracture behavior that is typically exhibited by the metallic materials. The cross sections of the fractured surfaces of substrate as represented in Figure 4.19 e) and f). These fractographs show the dimples or voids effect that are created at the places of precipitates and inclusions present in the alloy at the grain boundaries. This dimple type fracture is a characteristic

of the intergranular type or grain boundary fracture (Sajjadi & Zebarjad 2006; Price & Good 1984). At each dimple (hole), there was a precipitate. These precipitates were part of the Inconel in order to improve its hardness and strength. The reduced sections are more elongated when the tests are performed at higher temperatures. There is a considerable amount of plastic deformation that occurs before the alloy breaks in the reduced and deformed region (neck).

In Figure 4.20 are represented the micrographs of the composite material system mechanically tested and fractured at 600 °C. The fracture behavior is almost similar as for the composite system tested at room temperature. But the main difference is the higher thermal expansion of nickel matrix and Inconel substrate with respect to SiC fibers. This difference in coefficients of thermal expansions between nickel matrix and SiC fibers results in the decreasing of the nickel-SiC interface strength. Due to weak interfaces, the fibers carry less stress, and the plastic deformation, debonding and cracking of the nickel matrix start earlier than at the room temperature. It is also observed that in the tests at higher temperatures the nickel matrix cracks at various points on and around the SiC fibers as compared to less cracking regions at room temperatures. The micrographs a), b), c) and d) in the Figure 4.20 show these effects clearly. Also the superalloy behaves in a more ductile way than at the room temperature. In micrographs of Figure 4.20 a), b), e) and f), the cross section of the fractured surfaces of the Inconel substrate show signs of more plastic deformation before fracture and more elongated neck region as compared to room temperature.

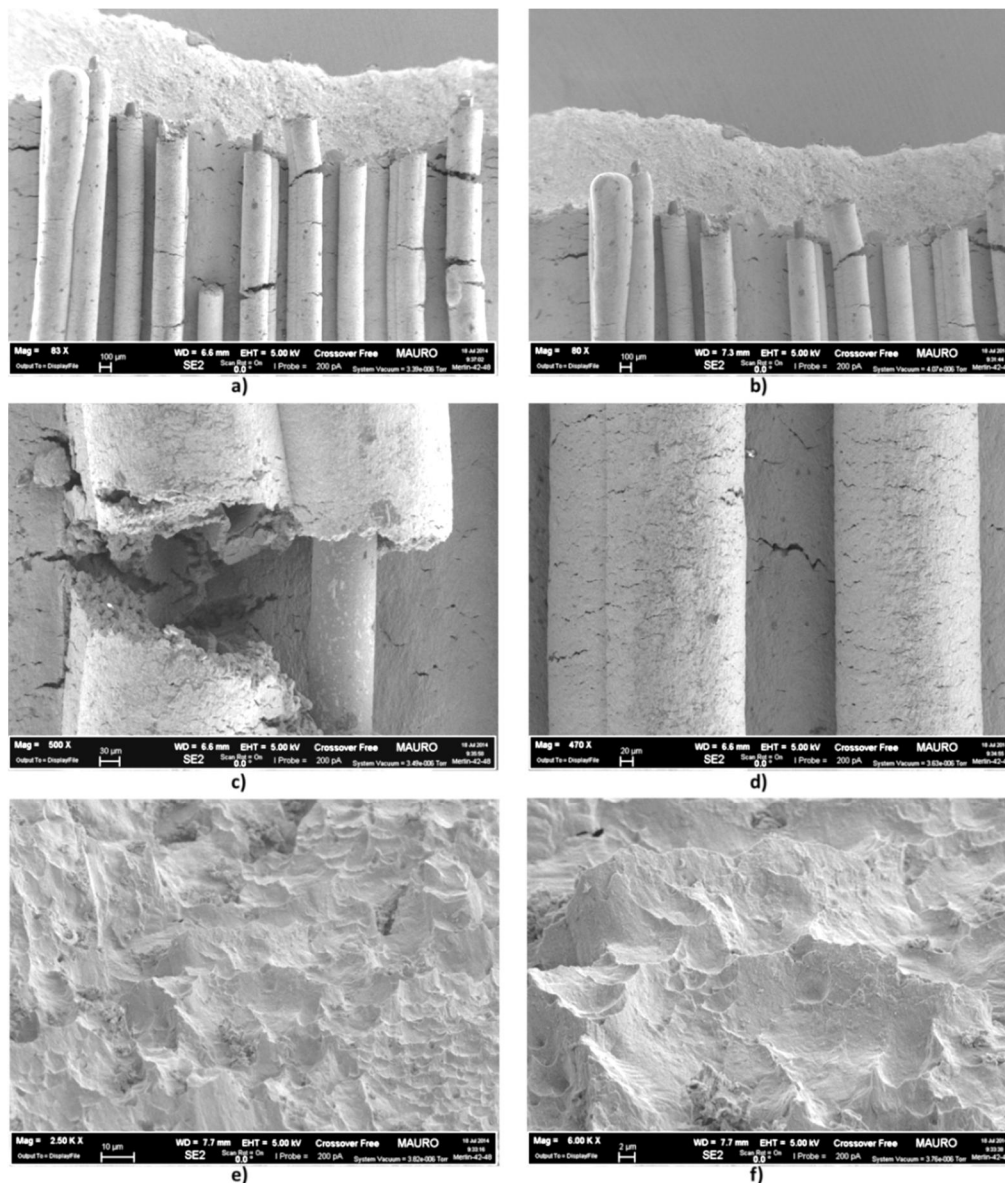


Figure 4.20: SEM fractographs of Inconel-718/Ni-SiC composites after tension tests at 600 °C

Figure 4.21 shows the fractographs of the surfaces after mechanical tests at 800 °C. At this temperature the thermal stresses at the nickel-SiC interface are still higher, so that a higher number of localized cracks are observed in the nickel matrix around the SiC fibers. Micrographs a), b), c) and d) in Figure 4.21 show this effect more prominently. The nickel matrix gets very easily debonded from the SiC fibers at various points and after that it slides along the length of the fibers. The overall strength of the material system is much reduced at this temperature and the material behaves in a very ductile manner. The Inconel substrate also elongates and plastically deforms with increased

amount of strain before fracture. The fractured surface of the superalloy base is more elongated and thin as shown in micrograph 4.21 a), representing the more ductile behavior, and micrographs 4.21 e) and f) showing extensive amount of plastic deformation and slip in the nickel based superalloy before the fracture (Sajjadi & Zebarjad 2006; Price & Good 1984) at high temperature. Due to substantial low strengths, further testing was not done at the 800 °C temperature. Rather 400 °C and 600 °C were chosen for the evaluation of mechanical properties of the composites.

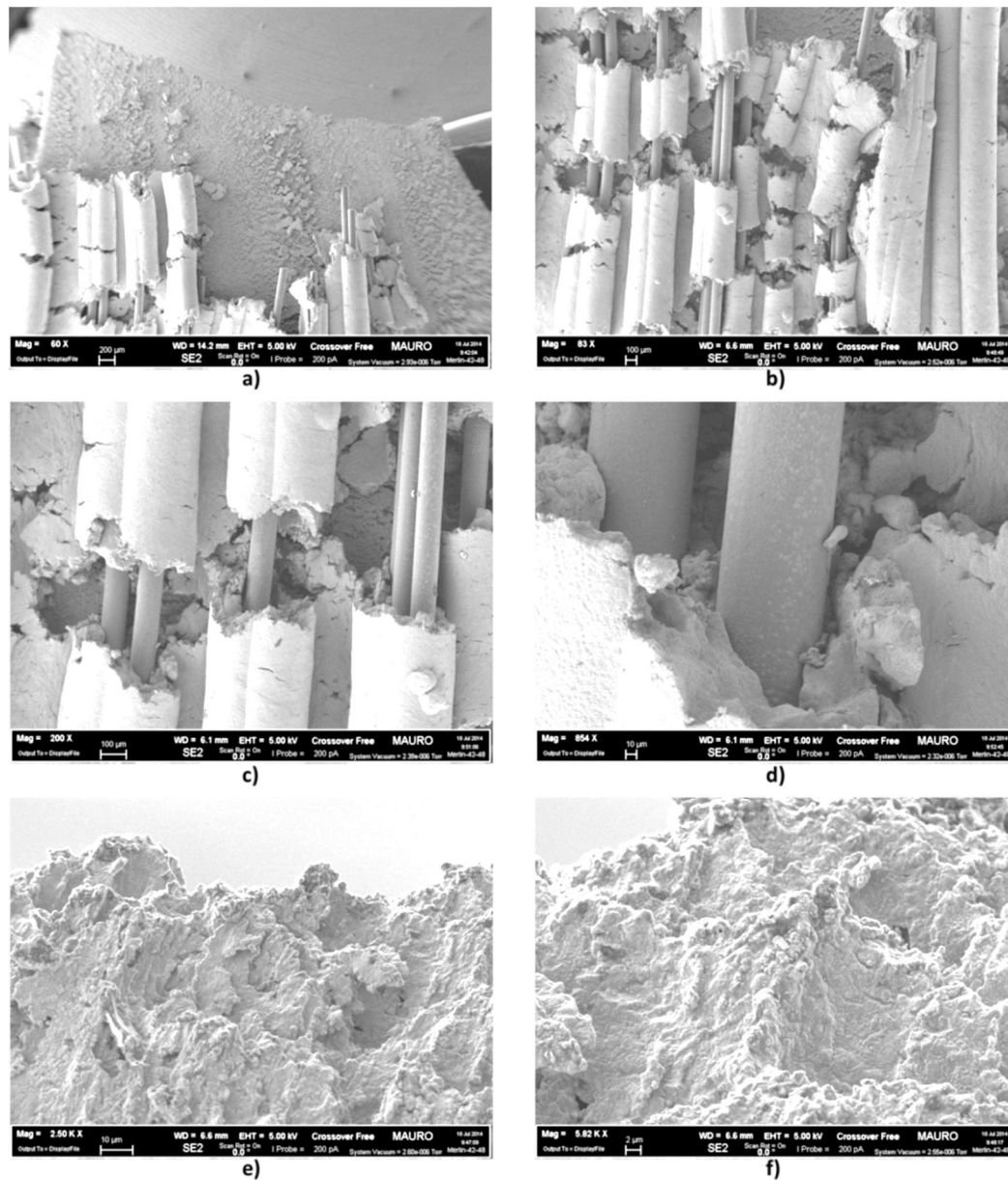


Figure 4.21: SEM fractographs of Inconel-718/Ni-SiC composites after tension tests at 800 °C

4.1.7 EDS analysis

Energy dispersive spectroscopy analysis was performed in order to understand the elemental composition present at different places on the composites. Figure 4.22 shows the EDS spectra of nickel coating and the Inconel substrate that were taken on the un-treated and un-tested polished sample.

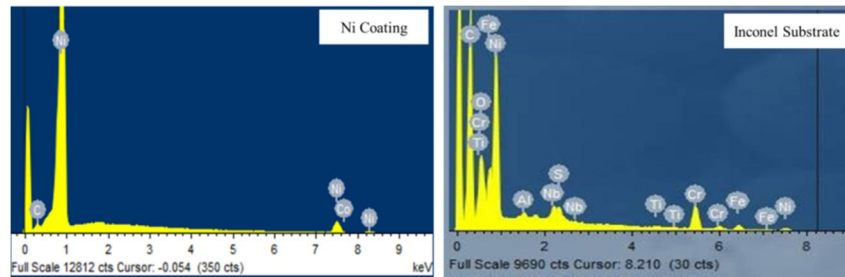


Figure 4.22: EDS graphs of polished surfaces of Ni coating and Inconel substrate

The EDS spectra for the evaluation of elemental composition of the composites at higher temperatures were taken on the fractured surfaces of the composites after the mechanical testing. At the interface between nickel and silicon carbide fibers, two regions were selected for the EDS analysis at both 600 and 800 °C. One region was on the pulled out peripheral surface of the silicon carbide fiber whereas the second region was cross section of the nickel coating very close to the silicon carbide fiber.

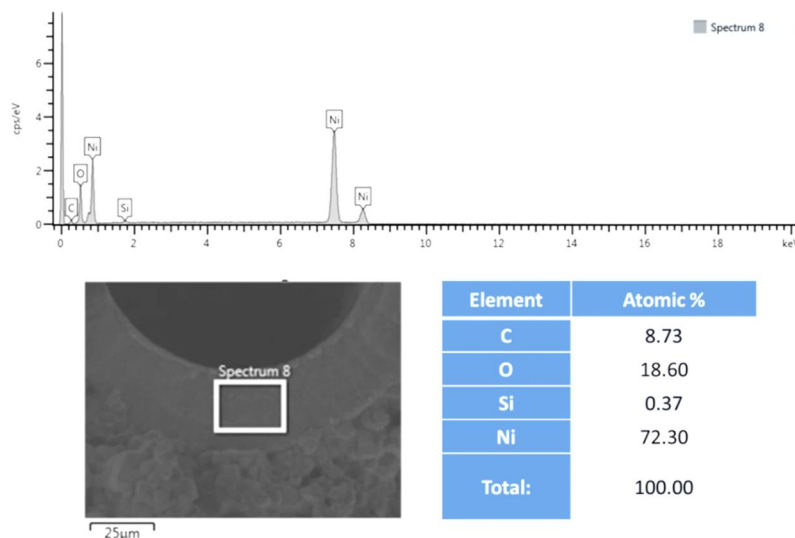


Figure 4.23: EDS on the nickel coating near the interface for the specimen tested at 600 °C

Figure 4.23 shows the results of the analysis of the nickel coating section close to the nickel/fiber interface for the samples tested at 600 °C. Although the main percentage present in the elemental composition corresponds to nickel, small atomic percentages of silicon and carbon are present too. This is because of their diffusion inside the nickel, due to the high temperature. Even if carbon is quantified very badly by EDS, and a small carbon peak was observed also on the untreated samples, silicon presence is probably due only to diffusion. Oxygen is instead linked to the oxidation suffered during the testing at 600 °C.

In Figure 4.24, the results obtained by analysis at fibers surface on the samples tested at 600 °C are shown. Here the major elements present in greater amount are the silicon and carbon which are the main constituents of silicon carbide fiber. Carbon is also present as a thin coating on the fibers. A small amount of nickel is also present from the nickel matrix which could be due to the reason that a very thin layer of nickel (possibly nickel Wood's layer) is still present on the fiber's surface even after its pull out from the nickel matrix.

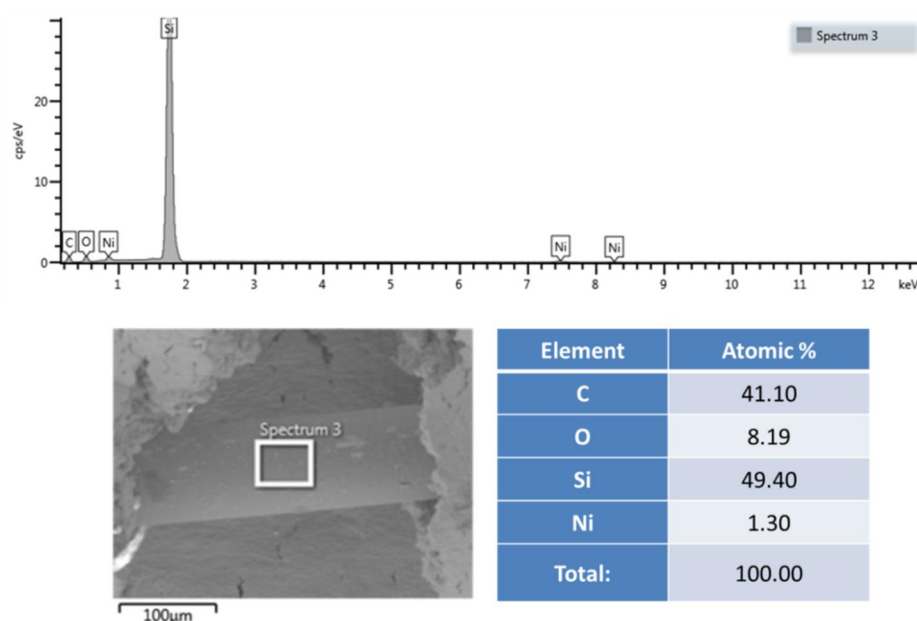


Figure 4.24: EDS on the lateral surface of pulled out SiC fiber after testing at 600 °C

The EDS curves along with the atomic percent of the elements for the specimens tested at 800 °C are shown in Figure 4.25 and Figure 4.26. With respect to the case of 600 °C, silicon content is higher, confirming the diffusion of silicon inside the nickel matrix. At

the higher temperature of 800 °C, the diffusion is relatively more favored and the amount of silicon diffused from the fiber to the nickel has increased from 0.37 % to 1.21 % (Figure 4.25).

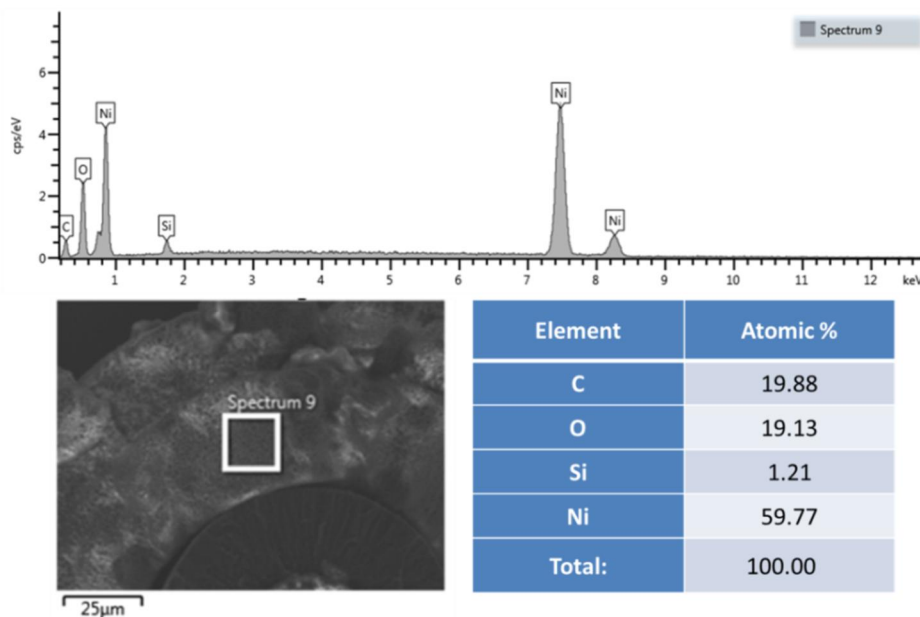


Figure 4.25: EDS on nickel coating near the interface for the specimen tested at 800 °C

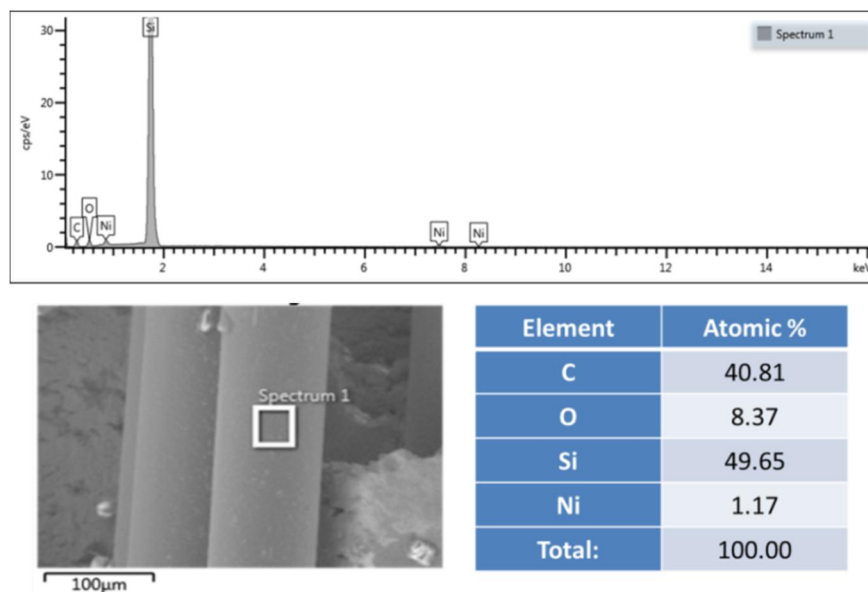


Figure 4.26: EDS on the lateral surface of pulled out SiC fiber after testing at 800 °C

4.2 Ni-GNP and Ni-GO composites

As a second part of the research work, Ni-graphene nanoplatelets and Ni-graphene oxide composites were electrochemically deposited on a steel substrate by using a three electrodes electrochemical cell system. The properties investigated for this kind of composites include the dispersion stabilities of the nanomaterials in the deposition baths, Vickers micro-hardness, crystallite size, wear rate and frictional behavior of the final produced carbon nanomaterials reinforced nickel matrix composites.

4.2.1 Dispersion stabilities of carbon nanomaterials

First of all the dispersion stability of the graphene oxide and graphene nano-platelets in the Watt type baths was evaluated. The dispersion technique employed for this purpose was ultrasonic probe sonication. The power applied by the probe sonicator was 70-100 W and the dispersion times used were 30 and 60 minutes. The dispersion stability for both of the nanomaterials was evaluated by using different percentage quantities of the nanomaterials as well as the dispersing agents. Initially sodium dodecyl sulphate (SDS) and poly acrylic acid (PAA) were tried as the dispersing agents. These worked well for the dispersions of the nanomaterials in water but did not work for dispersing them in the Watt type nickel deposition bath. It is because the Watt type bath is slightly acidic and so a surfactant with relatively strong acid in nature was thought to be tried. Poly sodium styrene sulphonate and poly sodium naphthalene sulphonate were used to investigate their effect on the stability of the dispersions. The dispersants adsorb at the surface of the nanomaterials and prevent their agglomeration. The results of the stability, as measured by the visual observations, for the used compositions of carbon nanomaterials and surfactants are depicted in the in the Table 4.3.

Table 4.3: Dispersion stability evaluations for GO

| | GO (Wt./V%) | Dispersant (Wt./V%) | GO-Dispersant Ratio | Probe Sonication (Minutes) | Dispersion Stability (Minutes) |
|--------------------------|----------------|------------------------|------------------------|-------------------------------|-----------------------------------|
| No Dispersant | 0.01 | x | 1:0 | 15 | 45 |
| | | | | 30 | 60 |
| | | | | 60 | 45 |
| PSNS | 0.01 | 0.1 | 1:10 | 30 | 60 |
| | | | | 60 | 75 |
| | | 0.2 | 1:20 | 30 | 90 |
| | | | | 60 | 75 |
| | | 0.4 | 1:40 | 30 | 120 |
| | | | | 60 | 90 |
| PSS | 0.01 | 0.02 | 1:2 | 30 | 105 |
| | | | | 60 | 90 |
| | | 0.05 | 1:5 | 30 | 180 |
| | | | | 60 | 120 |
| | | 0.1 | 1:10 | 30 | 255 |
| | | | | 60 | 150 |
| | | 0.2 | 1:20 | 30 | 135 |
| | | | | 60 | 135 |

The dispersion stability of graphene nanomaterials was not more than one hour when not using any surfactant. But the stability increases with the use of surfactants as shown in Table 4.3. There is not much difference in the stability by increasing the ultrasonication time from 30 minutes to 60 minutes, instead in most of the cases a decrease was observed at one hour of sonication. But the concentration of the surfactant affects to considerable extent in terms of stability of the graphene oxide in the Watt type deposition bath. Also the surfactant PSS gives better stability than the PSNS even with lower concentration. Based on these observations, a ratio of 1:10 for the quantities of nanomaterials and the PSS (poly sodium styrene sulphonate) dispersant was selected as the suitable surfactant concentration with 30 minutes of probe sonication duration.

The dispersant stabilities of the Watt bath without dispersant and with 0.1% PSS dispersant at 30 minutes of ultrasonication with the probe are represented in the Figure 4.27 and Figure 4.28.

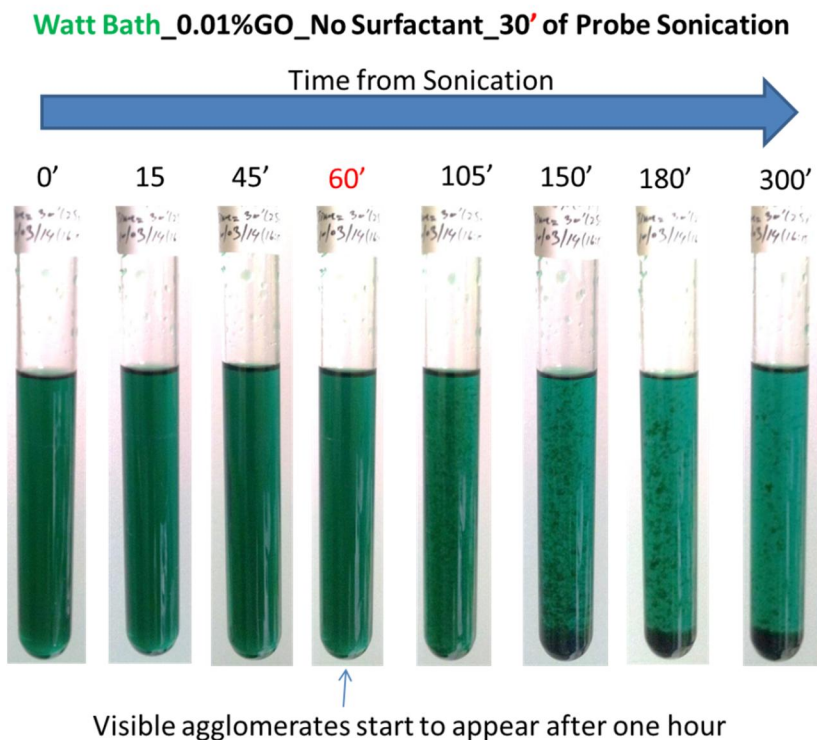


Figure 4.27: Dispersion stability of graphene oxide in Watt bath after 30 minutes of sonication without any dispersant used

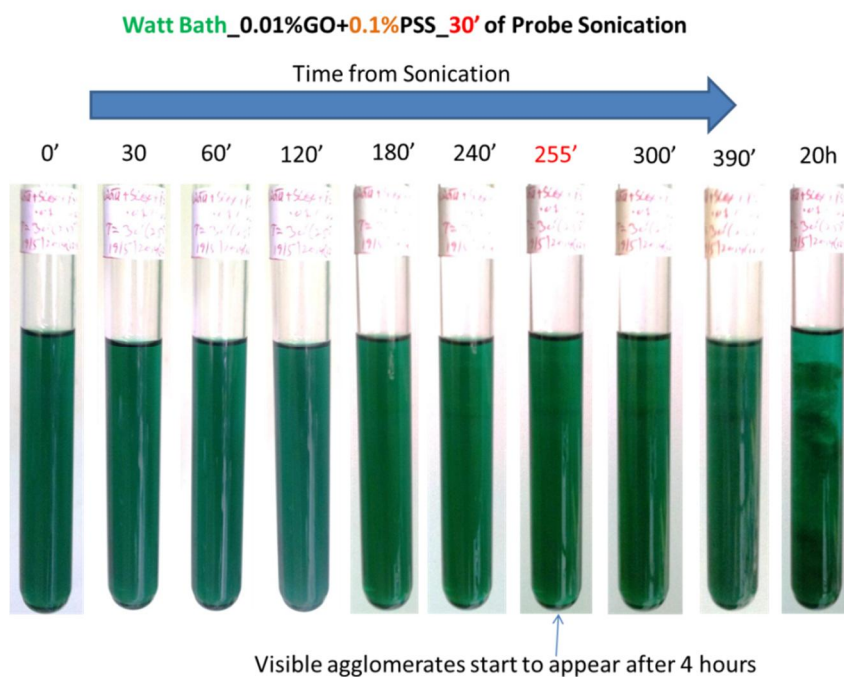


Figure 4.28: Dispersion stability of graphene oxide in Watt bath after 30 minutes of sonication with PSS dispersant

4.2.2 Production of the composites

After the evaluation of the dispersions the nickel matrix composites reinforced with the graphene oxide and graphene nanoplatelets were obtained using the optimized conditions of experimentation. The matrix composites were prepared by using different compositions of the carbon nanomaterials i.e. 0.05%, 0.1% and 0.2%. The scheme of the samples produced with different compositions is shown in Table 4.4 and the aspects of the coating in Figure 4.29.

Table 4.4: Details of the electrodeposited composites

| composites | % of nano material (Wt/Vol.) | % of surfactant (Wt/Vol.) | Probe Sonication (minutes) | Gentle magnetic Stirring during deposition (Hours) | Current density (A/dm ²) | Time of deposition (hours) |
|-------------------|------------------------------|---------------------------|----------------------------|--|--------------------------------------|----------------------------|
| Ni-GO Composites | 0.05 | 0.5 | 30 | 4 | 2 | 4 |
| | 0.1 | 1.0 | 30 | 4 | 2 | 4 |
| | 0.2 | 2.0 | 30 | 4 | 2 | 4 |
| Ni-GNP composites | 0.05 | 0.5 | 30 | 4 | 2 | 4 |
| | 0.1 | 1.0 | 30 | 4 | 2 | 4 |
| | 0.2 | 2.0 | 30 | 4 | 2 | 4 |



Figure 4.29: Ni composite-coated (left) and uncoated (right) samples

Two SEM images of the nickel composite coatings are shown in Figure 4.30. The coatings can present zones with good quality and no defects, on the left, or zones with agglomerates of GO or GNPs, as shown on the right.

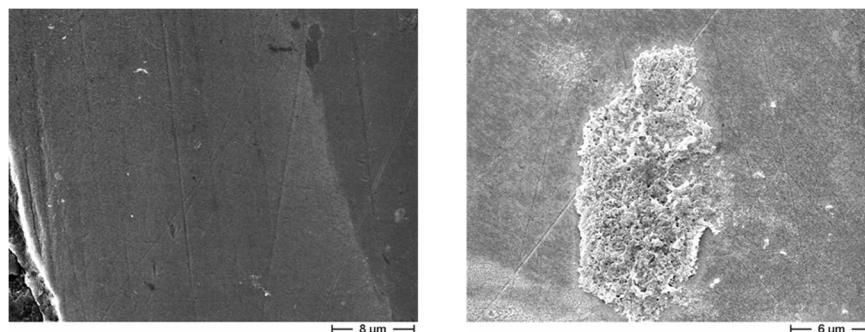


Figure 4.30: Carbon nanomaterials containing nickel layer with good quality (left); agglomerate in a nickel layer (right).

Some of the composite coatings were detached from the substrate and were broken to see the fractured surfaces under SEM. The micrographs are shown in the Figure 4.31. The fractured surfaces of pure nickel show a ductile type fracture while the surfaces of the Ni/GNP and Ni/GO composites represent a brittle type fracture. This ductile to brittle transition of the fracture mechanism suggests that it is due to the incorporation of carbon nanomaterials in the nickel matrix (Xiao et al. 2001).

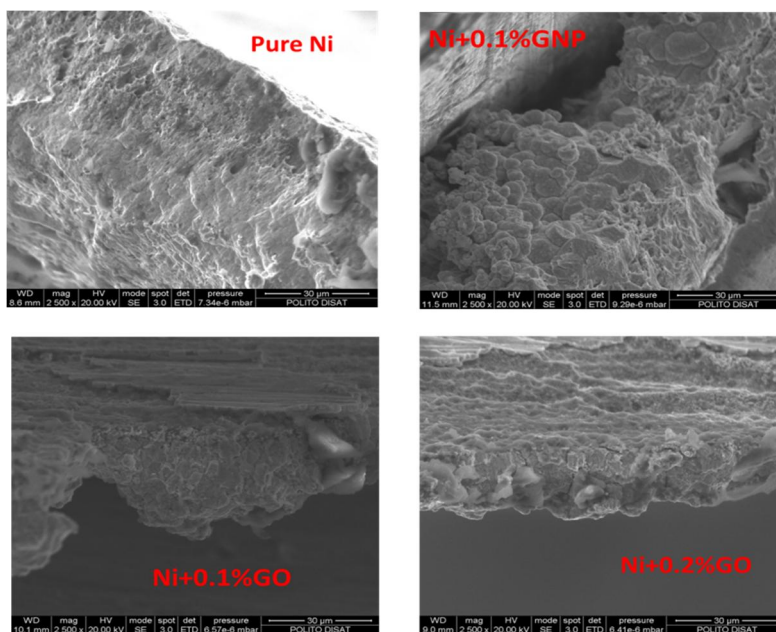


Figure 4.31: SEM images of torn specimens of nickel nano composites

4.2.3 Hardness and grain size measurements

Micro-hardness of the coatings was determined by using Vickers micro-hardness tester. A 100 g load was applied for 20 seconds and then the diagonals of the indents were measured to calculate the hardness values.

In order to measure the size of the nickel crystallites, X-ray diffraction (XRD) was also performed and the Scherrer formula was applied:

$$d = K\lambda/b\cos\theta \quad \text{Eq. 4.1}$$

where d is the crystallite size, K is a constant depending on the geometry of the grains, λ is the copper K_{α} wavelength, b is the width of the XRD peaks, and θ is the diffraction angle. The instrumental contribution towards the broadness of the peaks were also considered and determined using an XRD scan on a silicon monocrystal. The instrumental broadening calculated was subtracted from the peaks broadenings of the nickel composite coatings in order to have the real crystallite size. The values of micro-hardness and the crystallite sizes measured are depicted in the Figure 4.32.

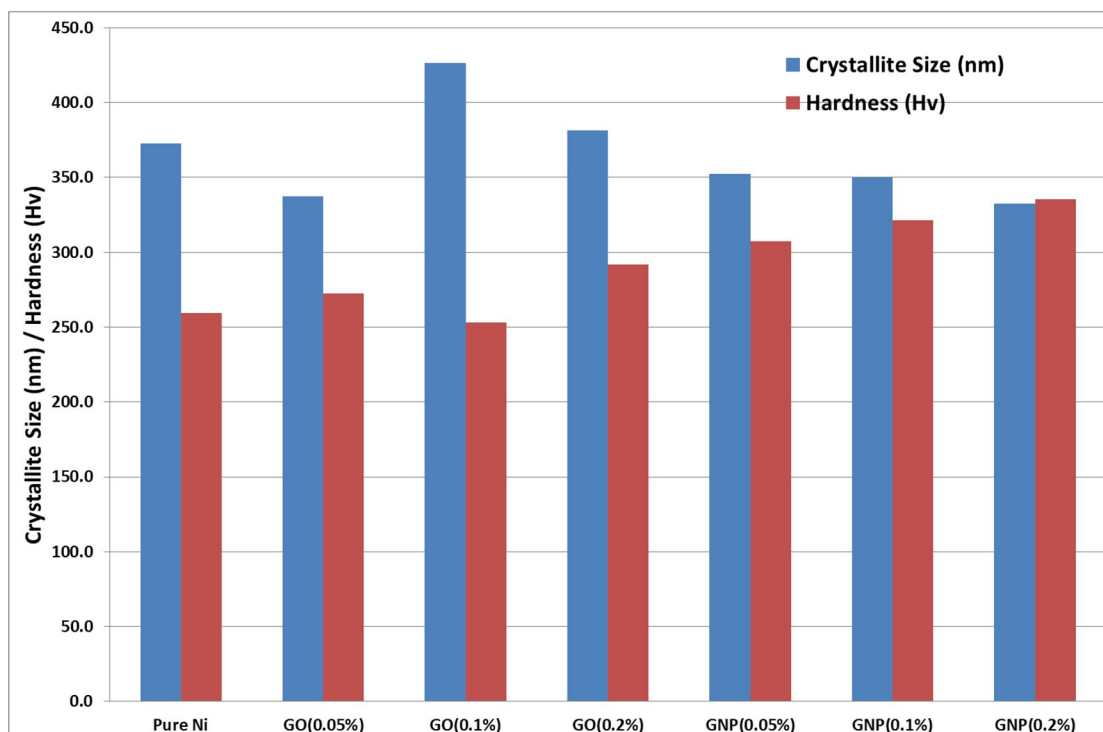


Figure 4.32: Hardness and crystallite size of the nano-composites

The deposition of pure nickel already gave a rather low grain size, with sub-micrometric dimension, around 370 nm. The incorporation of carbon nanomaterials in the coating does not change significantly the crystallite size that ranges always between 340 and 420 nm. A slight effect on the hardness is observed for GO, with hardness values rather close to those of the pure nickel, at least for 0.05% and 0.1% GO. For 0.2% GO the quantity of nanomaterials becomes more important and the hardness increases significantly over the value of the base alloy. With GNPs the hardness increase is higher even for very low GNP content (from 0.05%). In this case, probably the reduction of crystallite size is only one of the possible mechanisms for hardness increase that depends also on the increase of concentration of GNPs and, on the contrary, on the non-perfect dispersion of carbon nanomaterials. This latter effect can reduce the hardness due to the formation of large agglomerates of nanomaterials (as the one shown in Figure 4.30), as demonstrated by the hardness measurements, where the hardness increase is high from 0 to 0.05% GNP, while for 0.1% and 0.2% is less important.

4.2.4 Wear and friction behavior

The wear resistance and friction behavior of the produced nano-composite coatings were evaluated by using pin-on-disk testing setup.

Before proceeding to the wear testing, the roughness of the as deposited composites was measured by using the profilometer in order to verify that all the surfaces have the same surface finish during to the wear tests so that the results are comparable to each other.

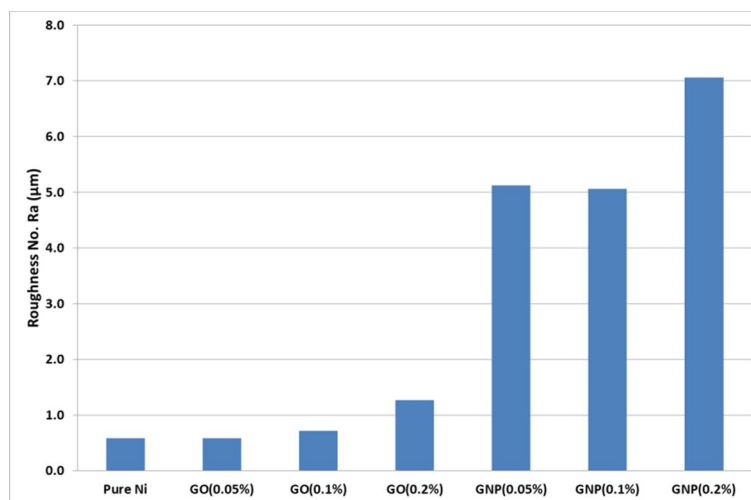


Figure 4.33: Roughness of the as deposited surfaces of the nano composites

Figure 4.33 shows that the surface roughness number (R_a) of pure nickel coatings is rather low, around $0.6 \mu\text{m}$. When GO or GNP are inserted in coating the roughness increases, however if low percentage of GO is used (0.05% or 0.1%) the roughness remains low, under $1 \mu\text{m}$. In case of high concentration GO the roughness begins to increase, up to $1.2 \mu\text{m}$, but it is with GNPs that the surface roughness becomes extremely high, with values from 5 to $7 \mu\text{m}$. For the standard wear tests, the roughness number should be less than $1 \mu\text{m}$ (ASTM 2014b). Therefore, all the composites were polished on 2000 grit paper to get the required roughness R_a .

Finally, wear tests were performed on the specimens using the parameters listed in Table 4.5. The specimens after the pin-on-disk tests are shown in Figure 4.34.

Table 4.5: Parameters of the pin on disk experiments

| Parameter | Details |
|----------------------|---------|
| Pin Type | WC/Co |
| Pin diameter (mm) | 3 |
| Track diameter (mm) | 20 |
| Load (N) | 10 |
| Sliding speed (rpm) | 180 |
| Sliding distance (m) | 226.2 |
| Sliding Time (min) | 20 |



Figure 4.34: The specimens after pin-on-disk tests showing wear tracks

The specimens were weighed before and after the test in order to evaluate the mass loss exhibited by the composites during the wear tests. The results of the percent mass loss are shown in the Figure 4.35.

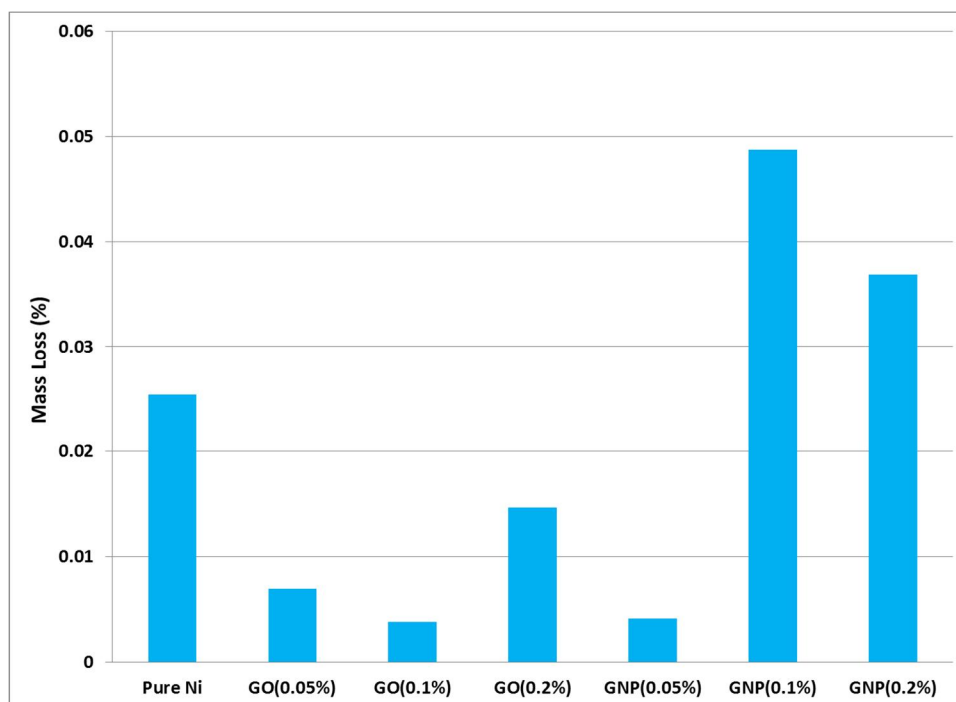


Figure 4.35: % mass loss of the nano composite coatings

Ni/GO composites with all concentrations of GO, show a decrease in the percent mass loss as compared to the pure nickel coatings suggesting that the addition of graphene oxide has a positive effect in reducing the wear of the composites. However, Ni/GNP composite coatings show a reduced percent mass loss only in case of low concentration of the nanomaterial. It can be due to the reason of non-uniform distribution and agglomeration of the GNPs in the composites. The poor wear results of 0.2% GNP coatings are also confirmed by the fact that they have more roughness in the as deposited state.

In order to compare the results of percent mass loss and to get relatively more accurate results about the wear behavior, volume loss was also measured by using the profilometer. In fact the profilometer gives the area of the worn track which can be

converted to the volume loss by considering the circumference of the wear track. The results are shown in Figure 4.36. So the results about the fact that 0.05% or 0.1% GO and 0.05% GNP reduce the wear seem confirmed also by the volume loss measurements, while a high increase is observed, with respect to the mass measurements, with 0.2% GO, similar to the 0.1% GNP case.

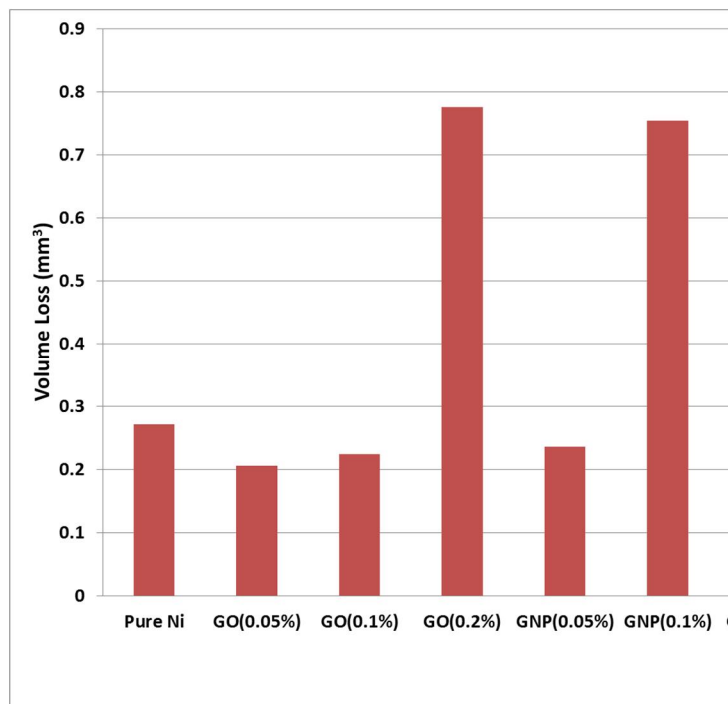


Figure 4.36: Volume loss of the nano composites after pin on disk experiments

The friction behavior of the carbon nanomaterials reinforced nickel matrix composites is shown in the Figure 4.37 for Ni/GO composites and in Figure 4.38 for Ni/GNP composites. As the tests involve the sliding conditions so here the friction coefficient is the kinetic coefficient of friction. The curves do not show a significant difference in friction behavior of the composites than the pure nickel. But the trajectories of the graphs presents that there is spontaneous jerking or the stick slip phenomenon involved during the sliding of the pin on the specimen disk. Due to this stick slip occurrence, the friction coefficient is too much variable to be reported numerically and in this case the friction behavior is reported as stick slip behavior (ASTM 2014a).

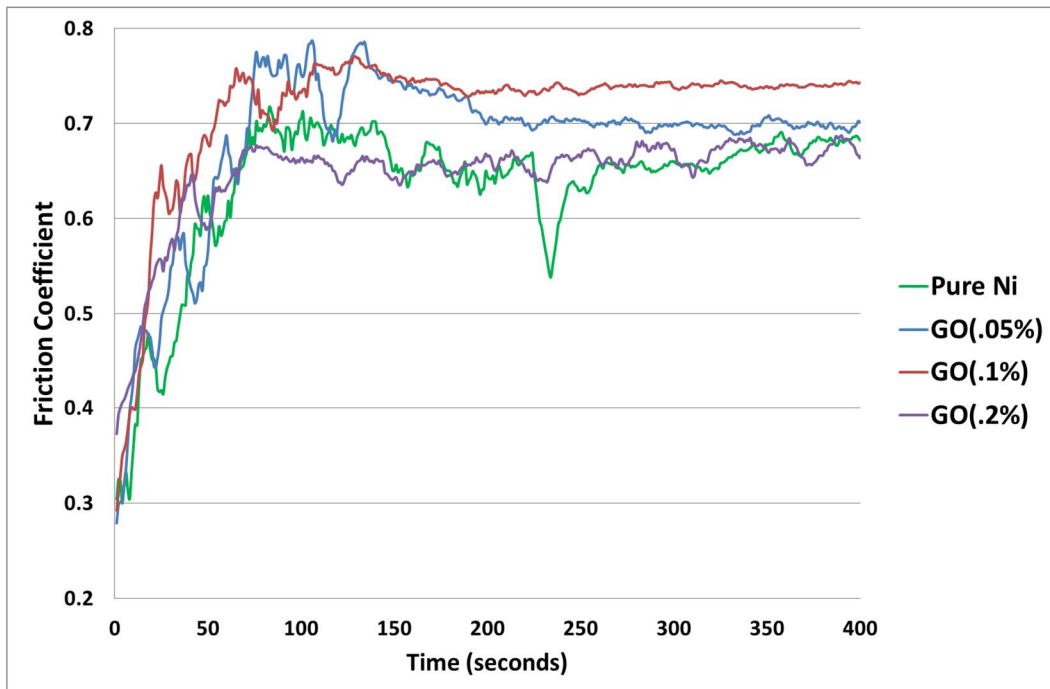


Figure 4.37: Friction behavior of Ni/GO composites as a function of time at 10 N load and 0.2 m/s sliding speed

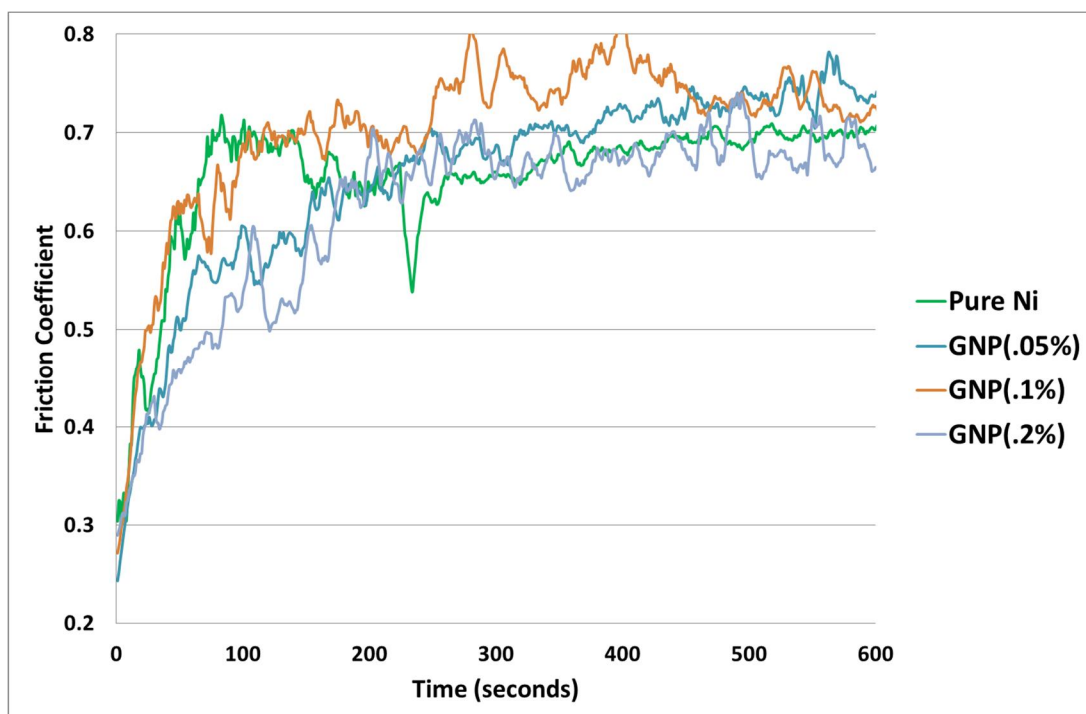


Figure 4.38: Friction behavior of Ni/GNP composites as a function of time at 10 N load and 0.2 m/s sliding speed

The SEM micrographs of the worn surfaces of the composites are shown in Figure 4.39 on next page. The evaluation of the surfaces suggests that the mechanism of wear exhibited by the composites is adhesive wear.

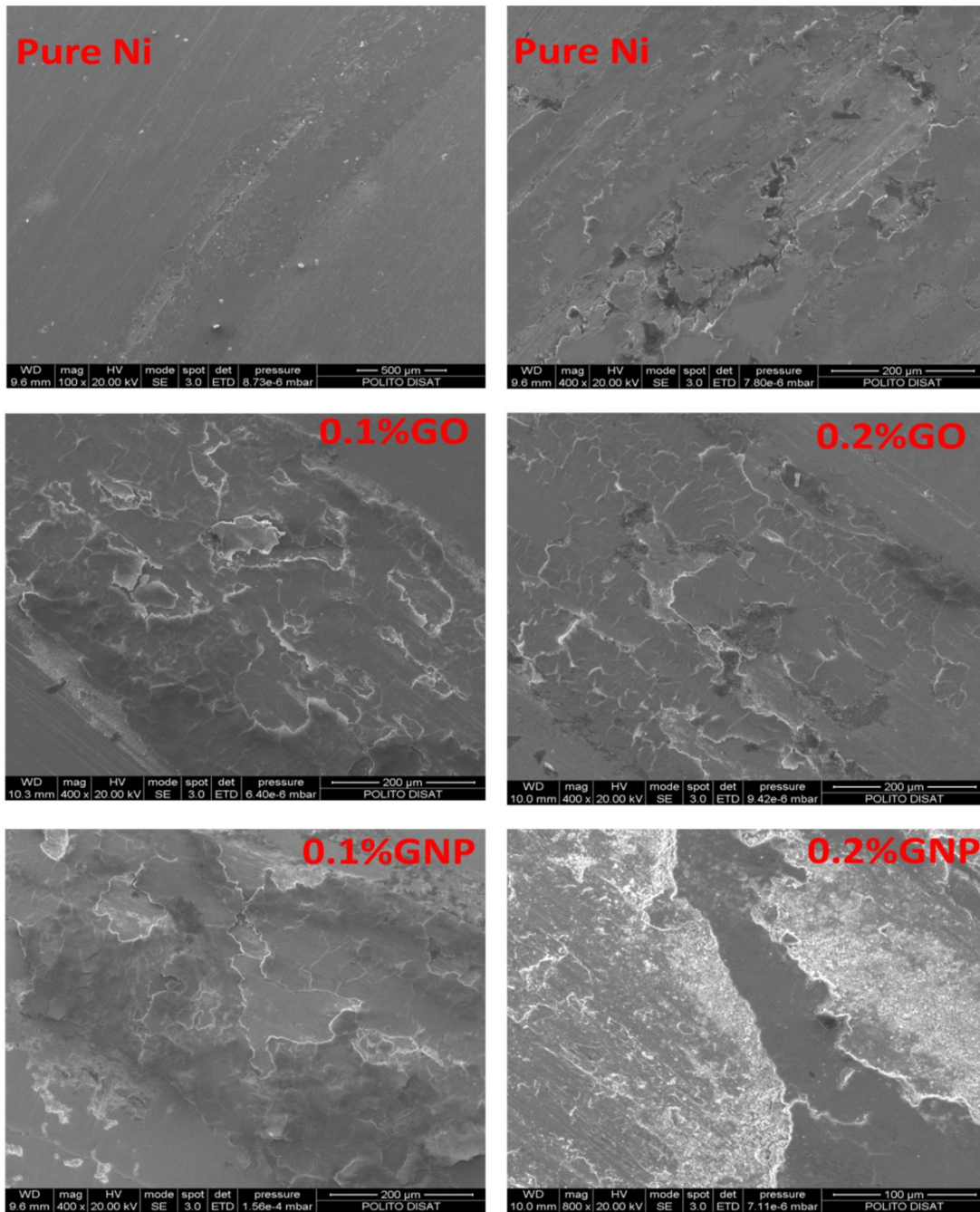


Figure 4.39: SEM images of the wear tracks after pin-on-disk experiment

Chapter 5 Conclusions

5.1 Fibers reinforced metal matrix composites

Electrodeposition of composites with nickel matrix and continuous silicon carbide fibers was successfully performed onto an Inconel 718 superalloy substrate. In order to have an insight on the possible high temperature interaction between superalloy and silicon carbide fibers, a chemical compatibility study was realized. This study made it possible to determine that the silicon carbide fibers must be coated by carbon, lest a reaction between superalloy and SiC takes place, and that the best choice for the matrix to be deposited is nickel. In fact, uncoated or TiB₂-coated silicon carbide fibers are prone to react with nickel that is the main component of Inconel 718, while carbon-coated ones do not. Both iron and chromium, that are also present in the superalloy composition, react with silicon carbide, while the reaction with carbon is evident only for chromium. This reaction however does not seem very strong, so that a nickel buffer layer could probably delay high temperature diffusion and consequently reaction. Thus the best choice for electrodepositing the composite on the superalloy seems to be nickel matrix and carbon-coated silicon carbide fibers.

Once the composition of the composite was determined, deposition was performed on the superalloy support, over which a parallel array of fibers was fixed by means of an epoxy resin. The deposition current density and deposition time were optimized. An intermediate Wood's bath deposition layer improved the adhesion between superalloy and nickel.

The stress-strain curves obtained from the mechanical tension tests demonstrated that at room temperature the superalloy reinforced with the Ni/SiC composite layer presents a higher yield strength than the pure superalloy. This is due to the high strength and stiffness of the silicon carbide fibers, and to the good interface that forms during the electrodeposition, that allows an effective stress transfer. However at higher temperature (already at 400 °C but the phenomenon is more evident at 600 °C) the interface yields, due to the thermal expansion coefficient of the nickel matrix, that is higher than the one of the silicon carbide fibers. This interface yielding reduces the

possibility of stress transfer to the silicon carbide fibers, so that the yield stress becomes similar or lower than the pure superalloy. To improve the yield strength at high temperatures, a hot pressing treatment of the specimen at 600 °C was designed. Hot pressing guarantees that the interface remains strong at 600 °C, while at room temperature no harmful effect can be observed (the only effect is the development of compressive residual stresses at the interface). Thus, it is possible to improve the interface quality and hence it is expected an improvement also of the hot strength. The study of the fractured surfaces of the specimens demonstrates that the fibers breaks at low strain values, and fibers fracture is followed by debonding and pull out, typical effects of the fracture in metal matrix composites. Moreover, the fracture in the superalloy undergoes the expected change from ductile to more ductile character, when increasing the test temperature from room temperature to 600 °C.

5.2 Carbon nanomaterials reinforced metal matrix composites

Graphene nanoplatelets and graphene oxide reinforced metal matrix composites were produced by electrochemical deposition on steel substrates. Good quality and well adherent thick composite coatings are achieved when the electrodeposition baths contain well and uniformly dispersed carbon nanomaterials and when the dispersions are stable for the sufficient period of time needed for the deposition. Since the deposition baths are generally acidic, it is important to use a suitable surfactant that works as a dispersant even at low pH. The result of a wide screening brought to the choice of poly sodium styrene sulphonate, that helps in attaining a stable suspension of the carbon nanomaterials in the nickel deposition bath during many hours, allowing to obtain good quality coatings. The suspension is obtained by mixing carbon nanomaterials inside the deposition baths and applying ultrasound energy by a probe sonicator. In this way the agglomerates of carbon nanomaterials are almost totally dispersed and single flakes of graphene nanoplatelets or graphene oxide are then encased in the nickel coating.

The produced nanocomposites were tested mainly for their wear properties. It was demonstrated that the co-deposition of carbon nanomaterials have no significant effect on the crystallite size of the nickel grains, while there is small increase observed in the hardness only in the case of Ni/GNP composites. The measurements of volume and mass loss demonstrated that wear resistance was improved only in the case of a low concentration of GO or GNP in the composites. Instead, samples obtained from high concentrated solutions exhibited more wear even than the pure nickel. This effect is probably due to the presence of big agglomerates of the graphene nano phases, that acts as defects in the coating. Indeed, the roughness of the coating increases substantially for high concentrations of GNP, where the chemical state of the surface makes more difficult the dispersion in the acidic water-based nickel deposition bath. Thus, the nanoparticles characteristics affects substantially the wear resistance, in particular their chemistry and structure. Their chemistry, since GO is better dispersed than GNP. Their structure, since in GNPs there is a relatively high number of layers, and thus it is further possible to exfoliate these graphene layers under stress, while in GO the layers are fewer.

Thus, even if the results in terms of friction coefficient or volume loss are not significantly improved with respect to the pure nickel layer, it is possible to draw some

conclusions about the possibility to produce nanocomposite coatings containing graphene-based phases by electrodeposition. The most important thing to keep into account is surely the dispersion of carbon nanomaterials inside the deposition bath. If the nanomaterials are well dispersed, they can exercise their function of improving the quality of the layer and its wear resistance. But if defects are present in the coating due to a scarce quality of the dispersion, than the positive effect of adding nanoparticles inside the nickel will be overcome by a bigger negative influence of defects and no improvement of properties will be observed.

Bibliography

- Allison, J.E. & Cole, G.S., 1993. Metal-matrix composites in the automotive industry: Opportunities and challenges. , 45(1), pp.19–24. Available at: <http://link.springer.com/10.1007/BF03223361>.
- Alwarappan, S. & Kumar, A., 2014. *Graphene-Based Materials: Science and Technology*, CRC Press, Taylor & Francis Group.
- An, B., Li, L. & Li, H., 2008. Electrodeposition in the Ni-plating bath containing multi-walled carbon nanotubes. *Materials Chemistry and Physics*, 110, pp.481–485.
- Arai, S., 2004. Ni-deposited multi-walled carbon nanotubes by electrodeposition. *Carbon*, 42, pp.641–644.
- Arai, S. & Endo, M., 2005. Various carbon nanofiber–copper composite films prepared by electrodeposition. *Electrochemistry Communications*, 7(1), pp.19–22. Available at: <http://linkinghub.elsevier.com/retrieve/pii/S1388248104002826>.
- Askeland, D.R., Fulay, P.P. & Wright, W.J., 2010. *The Science and Engineering of Materials* 6th ed., USA. Available at: <http://www.osti.gov/servlets/purl/15009526-vjFVRH/native/>.
- ASTM, I., 2014a. ASTM G115 Standard Guide for Measuring and Reporting Friction Coefficients. , 10(Reapproved 2013).
- ASTM, I., 2014b. ASTM G99, Standard Test Method for Wear Testing with a Pin-on-Disk Apparatus. , 05(Reapproved 2010), pp.1–5.
- Balandin, A.A. et al., 2008. Superior thermal conductivity of single-layer graphene. *Nano letters*, 8(3), pp.902–7. Available at: <http://dx.doi.org/10.1021/nl0731872>.
- Balandin, A.A., 2011. Thermal properties of graphene and nanostructured carbon materials. *Nature materials*, 10(8), pp.569–81. Available at: <http://dx.doi.org/10.1038/nmat3064>.
- Barin, I. & Platzki, G., 1995. *Thermochemical Data of Pure Substances* 3rd ed., Weinheim, New York: VCH Publishers Inc.
- Bayer, R.G., 2004. *Mechanical Wear Fundamentals and Testing* Second Edi., New York, NY: Marcel Dekker, Inc.
- Berns, H., 2003. Comparison of wear resistant MMC and white cast iron. *Wear*, 254(1-2), pp.47–54. Available at: <http://www.sciencedirect.com/science/article/pii/S0043164802003009>.
- Bethune, D.S., 1993. Cobalt-catalysed growth of carbon nanotubes with single-atomic-layer walls. *Nature*, 363.
- Blackwood, D.J. et al., 2000. Corrosion behaviour of porous titanium–graphite composites designed for surgical implants. *Corrosion Science*, 42(3), pp.481–503. Available at: <http://www.sciencedirect.com/science/article/pii/S0010938X99001031>.

- Bolotin, K.I. et al., 2008. Ultrahigh electron mobility in suspended graphene. *Solid State Communications*, 146(9-10), pp.351–355. Available at: <http://linkinghub.elsevier.com/retrieve/pii/S0038109808001178>.
- Breval, E., 1995. Synthesis routes to metal matrix composites with specific properties: A review. *Composites Engineering*, 5(9), pp.1127–1133. Available at: <http://www.sciencedirect.com/science/article/pii/096195269500048R>.
- Broomfield, R.W. et al., 1998. Development and Turbine Engine Performance of Three Advanced Rhenium Containing Superalloys for Single Crystal and Directionally Solidified Blades and Vanes. *Journal of Engineering for Gas Turbines and Power*, 120(3), p.595.
- Brown, M.E., 2001. *Introduction to Thermal Analysis: Techniques and Applications*, Dordrecht: Kluwer Academic Publishers.
- Budinski, K.G., 2009. *Guide to Friction, Wear, and Erosion Testing*, ASTM International.
- Bunsell, A.R. & Renard, J., 2005. *Fundamentals of Fibre Reinforced Composite Materials*, IOP Publishing. Available at: <http://linkinghub.elsevier.com/retrieve/pii/S1369702105710853>.
- Bürgel, R. et al., 2004. DEVELOPMENT OF A NEW ALLOY FOR DIRECTIONAL SOLIDIFICATION OF LARGE INDUSTRIAL GAS TURBINE BLADES. , pp.25–34.
- C. Zipperian, D., 2011. *Metallographic Handbook*, China: PACE Technologies.
- Callister, W.D. & Wiley, J., 2010. *Materials Science and Engineering: An Introduction 7th ed.*, USA: John Wiley & Sons, Inc.
- Carpenter, C.R., Shipway, P.H., Zhu, Y., et al., 2011. Effective dispersal of CNTs in the fabrication of electrodeposited nanocomposites. *Surface and Coatings Technology*, 205(20), pp.4832–4837. Available at: <http://linkinghub.elsevier.com/retrieve/pii/S0257897211004269>.
- Carpenter, C.R., Shipway, P.H. & Zhu, Y., 2011. Electrodeposition of nickel-carbon nanotube nanocomposite coatings for enhanced wear resistance. *Wear*, 271(9-10), pp.2100–2105. Available at: <http://linkinghub.elsevier.com/retrieve/pii/S0043164811002286>.
- Cassell, A.M., Kong, J. & Dai, H., 1999. Large Scale CVD Synthesis of Single-Walled Carbon Nanotubes. *J. Phys. Chem. B*.
- Castellino, M. et al., 2010. Thermal and Electronic Properties of Macroscopic Multi-Walled Carbon Nanotubes Blocks. *Journal of Nanoscience and Nanotechnology*, 10(6), pp.3828–3833. Available at: <http://www.ingentaconnect.com/content/asp/jnn/2010/00000010/00000006/art00013>.
- Ceschini, L. & Montanari, R., 2011. *Advances in Metal Matrix Composites*, Zurich: Trans Tech Pub. Ltd.
- Chamot, E.M. & Mason, C.W., 1958. *Handbook of Chemical Microscopy*, New York, NY: John Wiley & Sons, Inc.
- Chawla, N. & Chawla, K.K., 2013. *Metal Matrix Composites*, New York, NY: Springer New York. Available at: <http://link.springer.com/10.1007/978-1-4614-9548-2>.

- Chemists, R.S., 2014. Ultrasonication. Available at:
<http://www.rsc.org/publishing/journals/prospect/ontology.asp?id=CMO:0001708>.
- Chen, C. & Mansfeld, F., 1997. Corrosion protection of an Al 6092/SiCP metal matrix composite. *Corrosion Science*, 39(6), pp.1075–1082. Available at:
<http://www.sciencedirect.com/science/article/pii/S0010938X97000085>.
- Chipman, J., 1972. Thermodynamics and Phase Diagram of the Fe-C System. *Metallurgical Transactions*, 3(January).
- Choi, W. et al., 2010. Synthesis of Graphene and Its Applications: A Review. *Critical Reviews in Solid State and Materials Sciences*, 35(1), pp.52–71. Available at: <http://www.scopus.com/inward/record.url?eid=2-s2.0-77950941174&partnerID=tZOtx3y1>.
- Chou, S.-L. et al., 2010. Enhanced reversible lithium storage in a nanosize silicon/graphene composite. *Electrochemistry Communications*, 12(2), pp.303–306. Available at:
<http://www.sciencedirect.com/science/article/pii/S1388248109006225>.
- Chou, T.W., Kelly, A. & Okura, A., 1985. Fiber-reinforced metal-matrix composites. *Composites*, 16(3).
- Contributors, W., 2014. Archard_equation. Available at:
http://en.wikipedia.org/w/index.php?title=Archard_equation&oldid=603314120.
- Cullity, B.D., 1956. *Elements of X-Ray Diffraction*, USA: Addison-Wesley Publishing Company Inc.
- D. Gamburg, Y. & Zangari, G., 2011. *Theory and Practice of Metal Electrodeposition*, Springer New York.
- Davim, J.P. ed., 2012. *Machining of Metal Matrix Composites*, London: Springer London. Available at:
<http://link.springer.com/10.1007/978-0-85729-938-3>.
- Dini, J.W., 1993. *ELECTRODEPOSITION The Materials Science of Coatings and Substrates* Reprint Ed.,
- Divecha, A.P. & Church, F., 1970. Preparation of fiber-metal composites by electrodeposition.
- Djoki, S., 2014. *Electrodeposition and Surface Finishing* S. Djoki, ed., New York, NY: Springer.
- Ezugwu, E., Bonney, J. & Yamane, Y., 2003. An overview of the machinability of aeroengine alloys. *Journal of Materials Processing Technology*, 134(2), pp.233–253. Available at:
<http://linkinghub.elsevier.com/retrieve/pii/S0924013602010427>.
- Fan, Y. et al., 2010. Preparation and electrical properties of graphene nanosheet/Al₂O₃ composites. *Carbon*, 48(6), pp.1743–1749. Available at:
<http://www.sciencedirect.com/science/article/pii/S0008622310000400>.
- Fukuhara, M. & Sanpei, A., 1993. Elastic moduli and internal frictions of Inconel 718 and Ti-6Al-4V as a function of temperature. *Journal of Material Science Letters*, 12, pp.1122–1124.

- Fukui, H. et al., 2010. A Si-O-C composite anode: high capability and proposed mechanism of lithium storage associated with microstructural characteristics. *ACS applied materials & interfaces*, 2(4), pp.998–1008. Available at: <http://www.ncbi.nlm.nih.gov/pubmed/20423119>.
- Garcia, I. et al., 2003. Improved corrosion resistance through microstructural modifications induced by codepositing SiC-particles with electrolytic nickel. *Corrosion Science*, 45(6), pp.1173–1189. Available at: <http://linkinghub.elsevier.com/retrieve/pii/S0010938X02002202>.
- Geim, A.K. & Novoselov, K.S., 2007. The rise of graphene. *Nature materials*, 6(3), pp.183–91. Available at: <http://dx.doi.org/10.1038/nmat1849>.
- Ghosh, S., Sahoo, P. & Sutradhar, G., 2013. Friction Performance of Al-10%SiCp Reinforced Metal Matrix Composites Using Taguchi Method. *ISRN Tribology*, 2013, pp.1–9. Available at: <http://www.hindawi.com/journals/isrn.tribology/2013/386861/>.
- Gifkins, R.C., 1970. *Optical Microscopy of Metals*, New York, NY: American Elsevier Publishing Company.
- Gnecco, E., 2015. *Fundamentals of Friction and Wear on the Nanoscale* E. Gnecco & E. Meyer, eds., Cham: Springer International Publishing. Available at: <http://link.springer.com/10.1007/978-3-319-10560-4>.
- Gómez, E., Pollina, R. & Vallés, E., 1995. Nickel electrodeposition on different metallic substrates. *Journal of Electroanalytical Chemistry*, 386(1-2), pp.45–56. Available at: <http://www.sciencedirect.com/science/article/pii/002207289503817Z>.
- Graef, M. De & E. McHenry, M., 2007. *Structure of Materials: An Introduction to crystallography, Diffraction and Symmetry*, Cambridge, UK: Cambridge University Press.
- Guo, C. et al., 2008. The effects of electrodeposition current density on properties of Ni – CNTs composite coatings. *J surf. Coat. Technology*, 202, pp.3246 – 3250.
- Gupta, V.C. and A., 2011. *Carbon Nanotubes - Polymer Nanocomposites* S. Yellampalli, ed., InTech. Available at: <http://www.intechopen.com/books/carbon-nanotubes-polymer-nanocomposites/polymer-carbon-nanotube-nanocomposites>.
- Gyftou, P., Pavlatou, E. a. & Spyrellis, N., 2008. Effect of pulse electrodeposition parameters on the properties of Ni/nano-SiC composites. *Applied Surface Science*, 254(18), pp.5910–5916. Available at: <http://linkinghub.elsevier.com/retrieve/pii/S0169433208006557>.
- Haines, P.J., 2002. *Principles of Thermal Analysis and Calorimetry*, Royal Society of Chemistry.
- Hallstedt, B. et al., 2010. Thermodynamic properties of cementite (Fe₃C). *Calphad*, 34(1), pp.129–133. Available at: <http://linkinghub.elsevier.com/retrieve/pii/S0364591610000052>.
- Han, G.M. et al., 2011. Thermo-mechanical fatigue behavior of a single crystal nickel-based superalloy. *Materials Science and Engineering: A*, 528(19-20), pp.6217–6224. Available at: <http://linkinghub.elsevier.com/retrieve/pii/S0921509311005260>.
- Harrigan, W.C., 1998. Commercial processing of metal matrix composites. , 244, pp.75–79.

- He, T. et al., 2009. Preparation and Consolidation of Alumina/Graphene Composite Powders. *Materials Transactions*, 50(4), pp.749–751. Available at: <http://joi.jlc.jst.go.jp/JST.JSTAGE/matertrans/MRA2008458?from=CrossRef>.
- Herrmann, K., 2011. *Hardness Testing Principles and Applications*, ASM International.
- Hilder, M. et al., 2012. Graphene/zinc nano-composites by electrochemical co-deposition. *Physical chemistry chemical physics : PCCP*, 14(40), pp.14034–40. Available at: <http://www.ncbi.nlm.nih.gov/pubmed/22990074>.
- Hilding, J. et al., 2003. Dispersion of Carbon Nanotubes in Liquids. *Journal of Dispersion Science and Technology*, 24(1), pp.1–41. Available at: <http://dx.doi.org/10.1081/DIS-120017941>.
- Hovestad, A. & Janssen, L.J.J., 2005. Electroplating of Metal Matrix Composites by Codeposition of Suspended Particles. In *Modern Aspects of Electrochemistry No.38*. New York, NY: Kluwer Academic Publishers.
- Hu, Y. et al., 2010. Graphene–gold nanostructure composites fabricated by electrodeposition and their electrocatalytic activity toward the oxygen reduction and glucose oxidation. *Electrochimica Acta*, 56(1), pp.491–500. Available at: <http://www.sciencedirect.com/science/article/pii/S0013468610011813>.
- Iijima, S., 1991. Helical microtubules of graphitic carbon. *Nature*, 354, p.56.
- Iijima, S. & Ichihashi, T., 1993. Single-shell carbon nanotubes of 1-nm diameter. *Nature*, p.363.
- Ivanov, V. V. et al., 2009. Synergistic effect in nickel-Teflon composite electrolytic coatings. *Russian Journal of Applied Chemistry*, 81(12), pp.2169–2171. Available at: <http://link.springer.com/10.1134/S1070427208120252>.
- Jeon, Y.S., Byun, J.Y. & Oh, T.S., 2008. Electrodeposition and mechanical properties of Ni–carbon nanotube nanocomposite coatings. *Journal of Physics and Chemistry of Solids*, 69(5-6), pp.1391–1394. Available at: <http://linkinghub.elsevier.com/retrieve/pii/S0022369707006312>.
- Jung, a. et al., 2009. Nanocrystalline alumina dispersed in nanocrystalline nickel: enhanced mechanical properties. *Journal of Materials Science*, 44(11), pp.2725–2735. Available at: <http://link.springer.com/10.1007/s10853-009-3330-1>.
- Kainer, K.U., 2006. *Metal Matrix Composites Custom-made Materials for Automotive and Aerospace Engineering Edited by*, Weinheim: Wiley-VCH Verlag GmbH.
- Kandeil, A.Y. et al., 1984. The Fracture Behavior of Tungsten Wire Reinforced Superalloy Composites during Isothermal Forging. *Metallurgical Transactions A*, 15(March), pp.501–510.
- Kao, W.H. & Yang, J.-M., 1990. DEVELOPMENT OF ZrB₂ PARTICULATE-REINFORCED RENE 41 SUPER ALLOY COMPOSITE. *Materials and Manufacturing Processes*, 5(2).
- Khabazian, S. & Sanjabi, S., 2011. The effect of multi-walled carbon nanotube pretreatments on the electrodeposition of Ni–MWCNTs coatings. *Applied Surface Science*, 257(13), pp.5850–5856. Available at: <http://linkinghub.elsevier.com/retrieve/pii/S0169433211001541>.

- KORAB, J. et al., Thermal conductivity of unidirectional copper matrix carbon fibre composites. *Composites. Part A, Applied science and manufacturing*, 33(4), pp.577–581. Available at: <http://cat.inist.fr/?aModele=afficheN&cpsidt=13498768>.
- Koráb, J. et al., 2002. Thermal conductivity of unidirectional copper matrix carbon fibre composites. *Composites Part A: Applied Science and Manufacturing*, 33(4), pp.577–581. Available at: <http://www.sciencedirect.com/science/article/pii/S1359835X02000039>.
- Lee, C. et al., 2013. Current Density Effect on Nickel Electroplating Using Post Supercritical CO₂ Mixed Watts Electrolyte. , 7(7), pp.488–493.
- Lee, C. et al., 2008. Measurement of the elastic properties and intrinsic strength of monolayer graphene. *Science (New York, N.Y.)*, 321(5887), pp.385–8. Available at: <http://www.sciencemag.org/content/321/5887/385.abstract>.
- Li, Y., Tang, L. & Li, J., 2009. Preparation and electrochemical performance for methanol oxidation of pt/graphene nanocomposites. *Electrochemistry Communications*, 11(4), pp.846–849. Available at: <http://www.sciencedirect.com/science/article/pii/S1388248109000642>.
- Liao, Y.S. & Shiue, R.H., 1996. Carbide tool wear mechanism in turning of Inconel-718 superalloy. *Wear*, 193, pp.16–24.
- LLORCA, J., 2002. High temperature fatigue of discontinuously-reinforced metal?matrix composites. *International Journal of Fatigue*, 24(2-4), pp.233–240. Available at: <http://www.sciencedirect.com/science/article/pii/S0142112301000779>.
- Luo, X. et al., 2007. The fabrication and property of SiC fiber reinforced copper matrix composites. *Materials Science and Engineering: A*, 459(1-2), pp.244–250. Available at: <http://linkinghub.elsevier.com/retrieve/pii/S0921509307000445>.
- Luth, H., 1995. *Surfaces and Interfaces of Solid Materials* 3rd ed., New York, NY: Springer.
- Manfredi, D. et al., 2010. Microstructure and mechanical properties of co-continuous metal/ceramic composites obtained from Reactive Metal Penetration of commercial aluminium alloys into cordierite. *Composites Part A: Applied Science and Manufacturing*, 41(5), pp.639–645. Available at: <http://www.sciencedirect.com/science/article/pii/S1359835X10000266>.
- Manfredi, D. et al., 2009. Preparation and properties of NiAl(Si)/Al₂O₃ co-continuous composites obtained by reactive metal penetration. *Composites Science and Technology*, 69(11-12), pp.1777–1782. Available at: <http://www.sciencedirect.com/science/article/pii/S0266353808004156>.
- Mathers, G., 2014. Hardness Testing Part-I. Available at: <http://www.twi-global.com/technical-knowledge/job-knowledge/hardness-testing-part-1-074/>.
- Mathews, F.L. & Rawlings, R.D., 1999. *Composite Materials: Engineering and Science*.
- Mazor, a. et al., 1988. Columnar Growth in Thin Films. *Physical Review Letters*, 60(14), pp.1455–1455. Available at: <http://link.aps.org/doi/10.1103/PhysRevLett.60.1455.3>.

- McLaughlin, R.B., 1975. *Accessories for the Light Microscope*, London: Microscope Publications Ltd.
- McLaughlin, R.B., 1977. *Special Methods in Light Microscopy*, London: Microscope Publications Ltd.
- Meyyappan, M., 2004. *Carbon Nanotubes: Science and Applications*, CRC Press. Available at: <http://books.google.com/books?hl=en&lr=&id=MgEJgwgyFBkC&pgis=1>.
- MIRACLE, D., 2005. Metal matrix composites – From science to technological significance. *Composites Science and Technology*, 65(15-16), pp.2526–2540. Available at: <http://www.sciencedirect.com/science/article/pii/S0266353805002058>.
- Mittal, V. ed., 2012. *Polymer-Graphene Nanocomposites*, Cambridge: Royal Society of Chemistry. Available at: <http://ebook.rsc.org/?DOI=10.1039/9781849736794>.
- Mukhopadhyay, P. & Rakesh, K., 2013. *Graphite, Graphene and Their Polymer Nanocomposites*, CRC Press, Taylor & Francis Group.
- Muñoz, E. et al., 2000. Single-walled carbon nanotubes produced by cw CO₂-laser ablation: study of parameters important for their formation. *Applied Physics A: Materials Science & Processing*, 70(2), pp.145–151. Available at: <http://link.springer.com/10.1007/s003390050026>.
- Nishida, Y., 2013. *Introduction to Metal Matrix Composites: Fabrication and Recycling*, Tokyo: Springer Japan. Available at: <http://link.springer.com/10.1007/978-4-431-54237-7>.
- Novoselov, K.S. et al., 2004. Electric field effect in atomically thin carbon films. *Science (New York, N.Y.)*, 306(5696), pp.666–9. Available at: <http://www.sciencemag.org/content/306/5696/666.abstract>.
- Novoselov, K.S., Jiang, D., et al., 2005. Two-dimensional atomic crystals. *Proceedings of the National Academy of Sciences of the United States of America*, 102(30), pp.10451–3. Available at: <http://www.pnas.org/content/102/30/10451.full>.
- Novoselov, K.S., Geim, A.K., et al., 2005. Two-dimensional gas of massless Dirac fermions in graphene. *Nature*, 438(7065), pp.197–200. Available at: <http://dx.doi.org/10.1038/nature04233>.
- OLORUNTOBA, D., EGHWUBARE, O. & OLUWOLE, O., 2011. Effect of Some Process Variables on Nickel Electroplating of Low Carbon Steel. *Leonardo Electronic Journal of Practices and Technologies*. Available at: http://lejpt.academicdirect.org/A18/079_094.htm.
- Osterberg, H., 1950. Microscope Imagery and Interpretations. , 40(5), pp.295–303.
- PAUNOVIC, M. & MORDECHAY, S., 2006. *FUNDAMENTALS OF ELECTROCHEMICAL DEPOSITION*, NEW JERSEY, NJ.
- Pavese, M., Musso, S. & Pugno, N.M., 2010. Compression Behaviour of Thick Vertically Aligned Carbon Nanotube Blocks. *Journal of Nanoscience and Nanotechnology*, 10(7), pp.4240–4245. Available at: <http://www.ingentaconnect.com/content/asp/jnn/2010/00000010/00000007/art00017>.

- Philips, V., 1971. *Modern Metallographic Techniques and Their Applications*, New York, NY: John Wiley & Sons, Inc.
- Price, C.E. & Good, J.K., 1984. The Tensile Fracture Characteristics of Nickel, Monel, and Selected Superalloys Broken in Liquid Mercury. *Journal of Engineering Materials and Technology*, 106(2), p.184. Available at: <http://materialstechnology.asmedigitalcollection.asme.org/sci-hub.org/article.aspx?articleid=1423372>.
- Qian, Y., Lu, S. & Gao, F., 2011. Synthesis of manganese dioxide/reduced graphene oxide composites with excellent electrocatalytic activity toward reduction of oxygen. *Materials Letters*, 65(1), pp.56–58. Available at: <http://www.sciencedirect.com/science/article/pii/S0167577X10007950>.
- Rawal, S., 2001. Metal Matrix Composites for Space Applications. *The Journal of The Minerals, Metals & Materials Society*.
- Robin, A., de Santana, J.C.P. & Sartori, A.F., 2009. Characterization of copper–silicon nitride composite electrocoatings. *Journal of Applied Electrochemistry*, 40(3), pp.507–513. Available at: <http://link.springer.com/10.1007/s10800-009-0022-0>.
- Rochow, T.G. & Rochow, E.G., 1995. *An Introduction to Microscopy by Means of Light, Electrons, X-Rays, or Ultrasound*, Boston, MA: Springer US. Available at: <http://link.springer.com/10.1007/978-1-4684-2454-6>.
- Rosso, M. et al., 2008. Performance enhancements of die casting tools through PVD nanocoatings. *International Journal of Material Forming*, 1(S1), pp.1259–1262. Available at: <http://link.springer.com/10.1007/s12289-008-0131-z>.
- Sadiku-Agboola, O. et al., 2011. Influence of Operation Parameters on Metal Deposition in Bright Nickel-plating Process. *PORTUGALIAE ELECTROCHIMICA ACTA ISSN 1647-1571*. Available at: <http://www.scielo.oces.mctes.pt/pdf/pea/v29n2/v29n02a03.pdf>.
- Sajjadi, S.A. & Zebarjad, S.M., 2006. Study of fracture mechanisms of a Ni-Base superalloy at different temperatures. , 18(1), pp.227–230.
- SCHLESINGER, M. & PAUNOVIC, M., 2010. *Modern Electroplating* M. Schlesinger & M. Paunovic, eds., Hoboken, NJ, USA: John Wiley & Sons, Inc.
- Schlueter, E. & Gumpertz, W.E., 1976. The Stereomicroscope: Instrumentation and Techniques. *American Laboratory*, pp.61–71.
- Shelley, J.S., Leclaire, R. & Nichols, J., 2001. Metal-Matrix Composites for Liquid Rocket Engines. *JOM*, (April), pp.1–4.
- Sheshadri, B.S., 1975. Effect of thioglycolic acid and benzotriazole on the cathodic polarization potential during electrocrystallization of copper on copper single crystal planes. *Journal of Electroanalytical Chemistry and Interfacial Electrochemistry*, 61(3), pp.353–360. Available at: <http://www.sciencedirect.com/science/article/pii/S0022072875802361>.
- Shima, H., 2011. Buckling of Carbon Nanotubes: A State of the Art Review. *Materials*, 5(12), pp.47–84. Available at: <http://www.mdpi.com/1996-1944/5/1/47>.

- Shimizu, Y., Nishimura, T. & Matsushima, I., 1995. Corrosion resistance of Al-based metal matrix composites. *Materials Science and Engineering: A*, 198(1-2), pp.113–118. Available at: <http://www.sciencedirect.com/science/article/pii/0921509395800653>.
- Shokrieh, M.M. & Rafiee, R., 2010. A review of the mechanical properties of isolated carbon nanotubes and carbon nanotube composites. *Mechanics of Composite Materials*, 46(2), pp.155–172. Available at: <http://link.springer.com/10.1007/s11029-010-9135-0>.
- Shrestha, N.K., Masuko, M. & Saji, T., 2003. Composite plating of Ni / SiC using azo-cationic surfactants and wear resistance of coatings. *Science*, 254, pp.555–564.
- Si, Y. & Samulski, E.T., 2008. Exfoliated Graphene Separated by Platinum Nanoparticles. *Chemistry of Materials*, 20(21), pp.6792–6797. Available at: <http://dx.doi.org/10.1021/cm801356a>.
- Sieborger, D., Knake, H. & Glatzel, U., 2001. Temperature dependence of the elastic moduli of the nickel-base superalloy CMSX-4 and its isolated phases. *Materials Science and Engineering: A*, 298, pp.26–33.
- Sinha, A.K., 2003. *PHYSICAL METALLURGY HANDBOOK*, New York, NY: McGRAW-HILL.
- Skákalová, V. & Kaiser, A.B., 2014. *Graphene: Properties, preparation, characterisation and devices*, Woodhead Publishing Ltd.
- Song, B. et al., 2010. Graphene-on-Au(111): a Highly Conductive Material with Excellent Adsorption Properties for High-Resolution Bio-/Nano- detection and Identification. *Chem. Phys. Chem*, (11), pp.585–589.
- Srivastava, M., Grips, V.K.W. & Rajam, K.S., 2007. Electrochemical deposition and tribological behaviour of Ni and Ni – Co metal matrix composites with SiC nano-particles. *Applied Surface Science*, 253, pp.3814–3824.
- Stankovich, S. et al., 2006. Graphene-based composite materials. *Nature*, 442(7100), pp.282–6. Available at: <http://dx.doi.org/10.1038/nature04969>.
- Stoller, M.D. et al., 2008. Graphene-based ultracapacitors. *Nano letters*, 8(10), pp.3498–502. Available at: <http://dx.doi.org/10.1021/nl802558y>.
- Suchentrunk, R., 2004. Chapter 24 METAL MATRIX COMPOSITES PRODUCED BY ELECTROPLATING . A REVIEW ON TECHNOLOGY AND APPLICATIONS. *Thin Films*, pp.241–250.
- Sun, X.J. & Li, J.G., 2007. Friction and Wear Properties of Electrodeposited Nickel–Titania Nanocomposite Coatings. *Tribology Letters*, 28(3), pp.223–228. Available at: <http://link.springer.com/10.1007/s11249-007-9254-5>.
- Tanaka, K., 2014. *Carbon Nanotubes and Graphene*, Elsevier.
- Tang, Y.-B. et al., 2010. Incorporation of graphenes in nanostructured TiO₂ films via molecular grafting for dye-sensitized solar cell application. *ACS nano*, 4(6), pp.3482–8. Available at: <http://www.ncbi.nlm.nih.gov/pubmed/20455548>.

- Tecchio, P., 1997. Fabrication and properties of carbon fibre- reinforced copper composite by controlled three-step electrodeposition. , 2.
- TETERINA, N. & KHALDEEV, G., 1998. Electrodeposition of composite nickel -teflon coatings from acetate baths. *Protection of metals*, 34, pp.276–279.
- Thess, A. et al., 1996. Crystalline ropes of metallic carbon nanotubes. *Science*, 273, pp.483–487.
- Tjong, S.C. & Ma, Z.Y., 1997. The high-temperature creep behaviour of aluminium-matrix composites reinforced with SiC, Al₂O₃ and TiB₂ particles. *Composites Science and Technology*, 57(6), pp.697–702. Available at: <http://www.sciencedirect.com/science/article/pii/S0266353897000298>.
- Torres, L.E.F.F., Roche, S. & Charlier, J., 2014. *Introduction to Graphene-Based Nanomaterials*, Cambridge University Press.
- Ultrasonics, H., 2014. Ultrasonic Devices to Disperse Nanomaterials. Available at: http://www.hielscher.com/nano_01.htm#ultrasonic_articles.
- Voort, G.F. Vander, 1999. *Metallography: Principles and Practice*, USA: ASM International.
- Wan, Y.Z. et al., 2000. Effects of fiber volume fraction , hot pressing parameters and alloying elements on tensile strength of carbon fiber reinforced copper matrix composite prepared by continuous three-step electrodeposition. *Materials Science*, 288, pp.26 – 33.
- Wang, F., Arai, S. & Endo, M., 2005. Preparation of nickel – carbon nanofiber composites by a pulse-reverse electrodeposition process. *Electrochemistry Communications*, 7, pp.674–678.
- Wang, K. et al., 2011. Preparation of graphene nanosheet/alumina composites by spark plasma sintering. *Materials Research Bulletin*, 46(2), pp.315–318. Available at: <http://www.sciencedirect.com/science/article/pii/S0025540810004320>.
- Wang, X. et al., 2011. A SnO₂/graphene composite as a high stability electrode for lithium ion batteries. *Carbon*, 49(1), pp.133–139. Available at: <http://www.sciencedirect.com/science/article/pii/S0008622310006287>.
- Wang, Z. et al., 2010. Laterally confined graphene nanosheets and graphene/SnO₂ composites as high-rate anode materials for lithium-ion batteries. *Nano Research*, 3(10), pp.748–756. Available at: <http://link.springer.com/10.1007/s12274-010-0041-5>.
- Ward, P.J. et al., 1996. Semi-solid processing of novel MMCs based on hypereutectic aluminium-silicon alloys. *Acta Materialia*, 44(5), pp.1717–1727. Available at: <http://www.sciencedirect.com/science/article/pii/S096645495003568>.
- Ward-Close, C.M. & Robertson, J.G., 1996. Advances in the fabrication of titanium based composites. *Advanced Performance Materials*, 3(3-4), pp.251–262. Available at: <http://link.springer.com/10.1007/BF00136790>.
- Waseda, Y., Matsubara, E. & Shinoda, K., 2011. *X-Ray Diffraction Crystallography*, New York, NY: Springer New York Dordrecht Heidelberg London.

- Watcharotone, S. et al., 2007. Graphene-silica composite thin films as transparent conductors. *Nano letters*, 7(7), pp.1888–92. Available at: <http://pubs.acs.org/doi/abs/10.1021/nl070477%2B>.
- Weber, L., Dorn, J. & Mortensen, A., 2003. On the electrical conductivity of metal matrix composites containing high volume fractions of non-conducting inclusions. *Acta Materialia*, 51(11), pp.3199–3211. Available at: <http://www.sciencedirect.com/science/article/pii/S1359645403001411>.
- Williams, G., Seger, B. & Kamat, P. V, 2008. TiO₂-Graphene Nanocomposites. UV-Assisted Photocatalytic Reduction of Graphene Oxide. , 2(7), pp.1487–1491.
- Wu, Y., Shen, Z. & Yu, T., 2014. *Two-Dimensional Carbon: Fundamental Properties, Synthesis, Characterization, and Applications*, Taylor & Francis. Available at: <http://scholar.google.com/scholar?hl=en&btnG=Search&q=intitle:No+Title#0>.
- Xiao, C. et al., 2001. Tensile behavior and fracture in nickel and carbon doped nanocrystalline nickel. *Materials Science and Engineering: A*, 301(1), pp.35–43. Available at: <http://www.sciencedirect.com/science/article/pii/S0921509300013927>.
- Xu, C., Wang, X. & Zhu, J., 2008. Graphene–Metal Particle Nanocomposites. *The Journal of Physical Chemistry C*, 112(50), pp.19841–19845. Available at: <http://dx.doi.org/10.1021/jp807989b>.
- Yan, J. et al., 2010. Fast and reversible surface redox reaction of graphene–MnO₂ composites as supercapacitor electrodes. *Carbon*, 48(13), pp.3825–3833. Available at: <http://www.sciencedirect.com/science/article/pii/S0008622310004537>.
- Yang, F., Deng, Z.-S. & Fan, Q.-H., 2013. A method for fast automated microscope image stitching. *Micron (Oxford, England : 1993)*, 48, pp.17–25. Available at: <http://www.sciencedirect.com/science/article/pii/S0968432813000231>.
- Yang, S. et al., 2010. Fabrication of cobalt and cobalt oxide/graphene composites: towards high-performance anode materials for lithium ion batteries. *ChemSusChem*, 3(2), pp.236–9. Available at: <http://www.ncbi.nlm.nih.gov/pubmed/19816895>.
- Young, R.J. et al., 2012. The mechanics of graphene nanocomposites: A review. *Composites Science and Technology*, 72(12), pp.1459–1476. Available at: <http://www.sciencedirect.com/science/article/pii/S0266353812001789>.
- Zhang, L.-S. et al., 2010. Mono dispersed SnO₂ nanoparticles on both sides of single layer graphene sheets as anode materials in Li-ion batteries. *Journal of Materials Chemistry*.
- Zhang, Y. et al., 2005. Experimental observation of the quantum Hall effect and Berry's phase in graphene. *Nature*, 438(7065), pp.201–4. Available at: <http://dx.doi.org/10.1038/nature04235>.
- Zheng, W.T. et al., 2009. Field Emission from a Composite of Graphene Sheets and ZnO Nanowires. *The Journal of Physical Chemistry C*, 113(21), pp.9164–9168. Available at: <http://dx.doi.org/10.1021/jp900881q>.

- Zhou, K. et al., 2010. A novel hydrogen peroxide biosensor based on Au–graphene–HRP–chitosan biocomposites. *Electrochimica Acta*, 55(9), pp.3055–3060. Available at: <http://www.sciencedirect.com/science/article/pii/S0013468610000964>.
- Zhu, S., Fahrenholtz, W.G. & Hilmas, G.E., 2007. Influence of silicon carbide particle size on the microstructure and mechanical properties of zirconium diboride–silicon carbide ceramics. *Journal of the European Ceramic Society*, 27(4), pp.2077–2083. Available at: <http://linkinghub.elsevier.com/retrieve/pii/S0955221906004808>.
- ZHU, Z. et al., 1997. Fabrication and properties of carbon fibre-reinforced copper composite by controlled three-step electrodeposition. *Journal of Materials Science*, 32(4), pp.1061–1067. Available at: <http://link.springer.com/article/10.1023/A%3A1018542809294>.
- Zieler, H.W., 1972. *The Optical Performance of the Light Microscope*, London: Microscope Publications Ltd.